AD_____

Award Number: W81XWH-11-1-0106

TITLE: Molecular Mechanisms Underlying Genomic Instability in Brca-Deficient Cells

PRINCIPAL INVESTIGATOR: Dr. Andre Nussenzweig

CONTRACTING ORGANIZATION: The Geneva Foundation
Lakewood, WA 98499

REPORT DATE: March 2013

TYPE OF REPORT: Annual

PREPARED FOR: U.S. Army Medical Research and Materiel Command
Fort Detrick, Maryland 21702-5012

DISTRIBUTION STATEMENT: Approved for public release; distribution unlimited

REPORT DOCUMENTATION PAGE

Form Approved
OMB No. 0704-0188

1. REPORT DATE *(DD-MM-YYYY)*	2. REPORT TYPE	3. DATES COVERED *(From - To)*
March 2013	Annual	1 March 2012 - 28 February 2013

4. TITLE AND SUBTITLE
Molecular Mechanisms Underlying Genomic Instability in Brca-Deficient Cells

5a. CONTRACT NUMBER

5b. GRANT NUMBER
W81XWH-11-1-0106

5c. PROGRAM ELEMENT NUMBER

6. AUTHOR(S)
Dr. Andre Nussenzweig

E-Mail: lwagner@genevausa.org

5d. PROJECT NUMBER

5e. TASK NUMBER

5f. WORK UNIT NUMBER

7. PERFORMING ORGANIZATION NAME(S) AND ADDRESS(ES)
The Geneva Foundation
Lakewood, WA 98499

8. PERFORMING ORGANIZATION REPORT NUMBER

9. SPONSORING / MONITORING AGENCY NAME(S) AND ADDRESS(ES)
U.S. Army Medical Research and Materiel Command
Fort Detrick, Maryland 21702-5012

10. SPONSOR/MONITOR'S ACRONYM(S)

11. SPONSOR/MONITOR'S REPORT NUMBER(S)

12. DISTRIBUTION / AVAILABILITY STATEMENT
Approved for Public Release; Distribution Unlimited

13. SUPPLEMENTARY NOTES

14. ABSTRACT

Our proposal is to explore the novel notion that it may be possible to restore near normal HR activity in Brca1 cells and tissues. We believe that this phenomenon will lead to targeted therapies to reduce lifetime risk of tumor formation in BRCA1 and potentially BRCA2 carriers.

15. SUBJECT TERMS
BRCA1, 53BP1, cancer biology, DNA repair, tumorigenesis

16. SECURITY CLASSIFICATION OF:			17. LIMITATION OF ABSTRACT	18. NUMBER OF PAGES	19a. NAME OF RESPONSIBLE PERSON
a. REPORT	b. ABSTRACT	c. THIS PAGE			USAMRMC
U	U	U	UU	56	19b. TELEPHONE NUMBER *(include area code)*

Page

Introduction

Genomic instability is a hallmark of cancer. Central to a cells ability to maintain genomic stability are systems that monitor and repair DNA double strand breaks (DSBs). The objective of this study is to understand how the choice of pathways used to repair DNA damage determines whether the repair is error free or causes genomic instability. In mammalian cells, homologous recombination (HR) and nonhomologous end joining (NHEJ) are the two major pathways involved in the repair of DNA DSBs. The Brca1 gene is required for DNA repair by homologous recombination and normal embryonic development. Additionally, protein 53BP1 promotes ligation and facilitates end joining. In previous studies, we have demonstrated that Brca1 and 53BP1 can compete for the processing of DSBs and that 53BP1 can promote genomic instability in the absence of Brca1. Thus, the tumor suppressive function of Brca1 does not appear to be absolute and can be modulated by altering the ability of cells to carryout NHEJ. Our study focuses on shifting the balance between these two repair pathways (HR and NHEJ) to restore error free repair and genomic stability. We believe that a better understanding of mechanisms of DSB repair pathway choice may have important therapeutic implications for prevention or treatment of Brca1/2 germline mutation-associated cancers.

Body

Aim 1: Determine the capacity of NHEJ deficiency to rescue defects in homologous recombination (HR). Using various established mouse models where there is a clearly described defect in HR, we will test the role of the NHEJ proteins 53BP1 and Ku in subverting HR.

We have discovered a new NHEJ factor called RIF1 that acts downstream of 53BP1 in blocking resection. This work was recently published (M. Di Virgilio et al. Science 2013). The relevant data is shown in Figure 4 of this publication as follows, which demonstrates increase RPA association at the IgH locus:

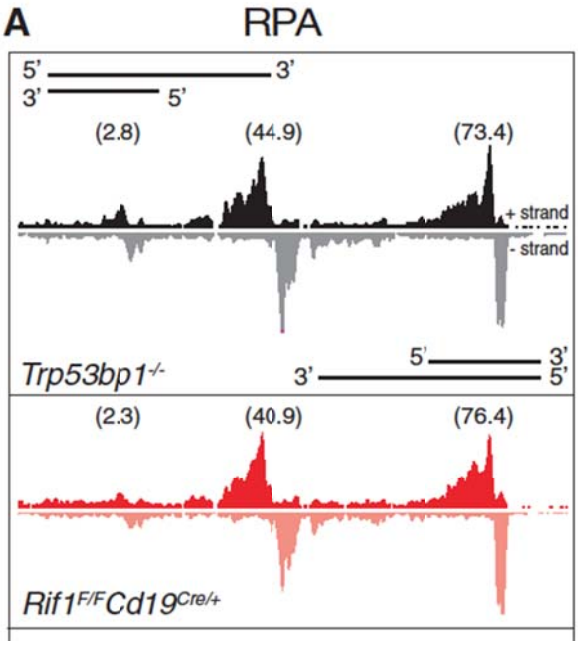

We are currently crossing mice containing floxed alleles of Brca1 with RIF1$^{-/-}$ mice to generate Brca1$^{f/f}$RIF1$^{+/+}$ and Brca1$^{f/f}$RIF1$^{-/-}$ mice. We propose to test these cells for HR reconstitution by assaying for the formation of chromosomal breaks and radial structures, Rad51 foci formation, RPA phosphorylation and PARPi sensitivity.

The proposed PALB2fl/fl x 53BP1 crosses have also been generated and characterized. This work was recently accepted for publication (C. Bowman-Colin et al. PNAS 2013). The relevant data is shown in Figure 4 of this publication as follows:

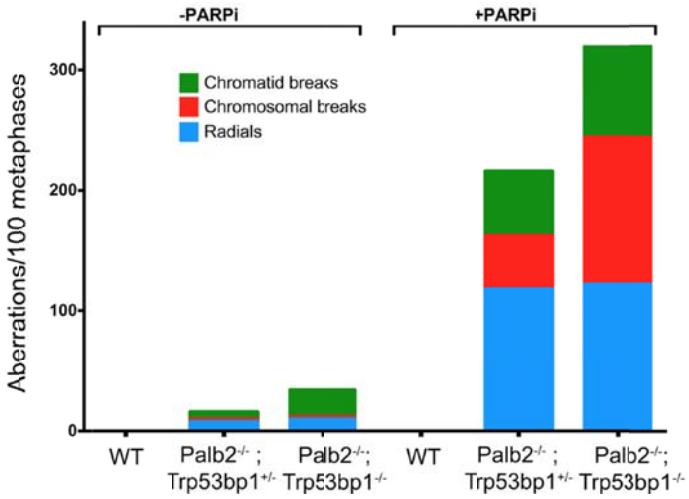

This demonstrates that unlike BRCA1, loss of 53BP1 (Trp53BP1) does not rescue the genome instability associated with deletion of PALB2.

Aim 2: Determine the domain of 53BP1 that inhibits HR in Brca1-deficient mice. We will use a combined in vitro and in vivo reconstitution approach to define the functional domains of 53BP1 that regulate the observed HR defects seen in Brca1-deficient cells.

We are using retroviral gene transfer to reconstitute 53BP1 mutants into Brca1$^{\Delta 11/\Delta 11}$53BP1$^{-/-}$ B cells. Given that Brca1$^{\Delta 11/\Delta 11}$53BP1$^{-/-}$ B cells are resistant to PARP inhibitors, we are using restoration of PARP sensitivity as an initial screen to determine the relevant domain of 53BP1 required for inhibiting HR activity. Simultaneously we are examining the domains required for class switching. Retroviral constructs include full-length 53BP1, 53BP1^{EV} (empty vector), 53BP1^{DB} and 53BP1^{8A}. We show that a 53BP1 phospho-mutant 53BP1^{8A}, comprising alanine substitutions of the 8 most N-terminal S/TQ phosphorylation sites, mimics 53BP1 deficiency by restoring genome stability in BRCA1 deficient cells yet behaves like wild-type 53BP1 with respect to immunoglobulin class switch recombination (CSR): The relevant data is shown below, and we have recently submitted a paper based on these findings:

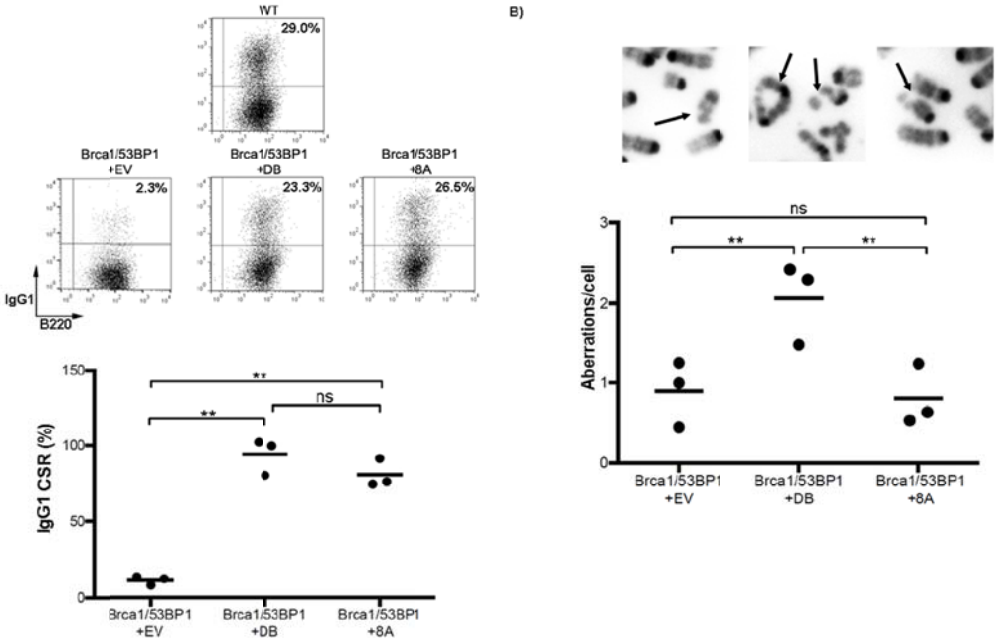

These results indicate 53BP1^{8A} behaves like a 53BP1 null with respect to rescuing BRCA1 deficiency, but is WT for class switching.

In the context of this proposal, we have been interested to know whether there are preferred "genomic sites" for genome instability during DNA replication. Recently we discovered a novel type of "fragile" site that contributes to genome instability. These sites (coined "ERFS" are broken spontaneously during replication, and their fragility is increased by hydroxyurea, ATR inhibition, deregulated c-Myc expression and by PARPi treatment of BRCA1 deficient cells. This work was recently published (J. Barlow et al. Cell; 152:620-632, 2013). The relevant data is shown in figure 3 of this manuscript, which shows examples and quantitation of ERFS breakage in response to HU:

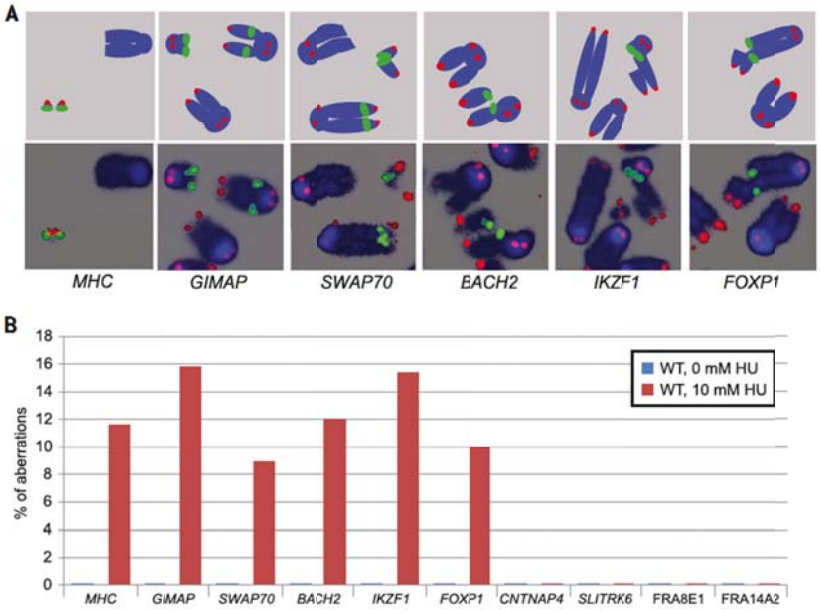

Aim 3: Develop small molecule inhibitors of 53BP1 as possible lead compounds to inhibit Brca-mediated tumor formation. This highly ambitious project is ongoing.

Task 1: Construct a GFP-53BP1 expression vector containing the minimal foci forming domain of 53BP1 and create stable cell line that has robust inducible foci formation following DNA damage (adriamycin treatment).

We have determined conditions for measuring 53BP1 foci using an alternative immunofluorescence approach that gives robust foci following treatment with the radiomimetic drug, neocarzinostatin (NCS). In collaboration with Dr. Ty Voss of the High-Throughput Microscopy Core at NIH, we have been able to visualize the foci using the automated Perkin-Elmer Opera platform that will enable screening of the NCI Diversity Set by measuring the suppression of the appearance of 53BP1 foci by any potential lead compound. Currently we are optimizing this system with appropriate positive and negative controls. This work will enable us to conduct a screen of the NIH Diversity Set of small molecules, thereby enabling us to carry out the more detailed screening approaches entailed in Specific Aim 3.

Key Research Accomplishments

- Deletion of the DNA damage response gene, RIF1, mimics 53BP1 deficiency with respect to increased resection and defective class switching.
- Genomic instability and hypersensitivity of BRCA1-deficient cells to inhibitors of polyADP-ribose polymerase (PARP inhibitors, PARPi) is not suppressed by deletion of PALB2.
- Phosphorylation of the N-terminus of 53BP1 is essential for the role of 53BP1 in promoting genomic instability in BRCA1-deficient cells but is dispensable for class switching.

- PARPi treatment leads to genome instability at preferred genomic sites.

Reportable Outcomes

1. Three high-impact papers have been published or are in press based on this work with the awardee, Dr. Andre Nussenzweig (M. Di Virgilio et al. Science 2013. C. Bowman-Colin et al. PNAS 2013, J. Barlow et al. Cell; 152:620-632, 2013). One additional paper has been submitted for publication.

Conclusion

This work has revealed for the first time that deletion of 53BP1 prevents genomic instability in cells lacking the tumor suppressor, BRCA1. 53BP1 therefore plays a key role in cellular changes leading to cancer in individuals with BRCA1 mutations. This validates the targeting of 53BP1 as a chemopreventive measure to avert the appearance of cancer in women with mutations in BRCA1, which accounts for ~5% of all annual cases of breast cancer and a higher proportion of ovarian cancers. This work further suggests that 53BP1 inactivation or deregulation of downstream pathways (eg. RIF1) is a potential mechanism leading to resistance of BRCA1-deficient tumors to chemotherapeutic regimens involving PARP inhibitors.

References

Di Virginio M, Callen E, Yamane A, Jankovic M, Gitlin AD, Feldhahn N, Resch W, Chait BT, Nussenzweig A, Casellas R, Robbiani DF, Nussenweig MC. **Rif1 prevents resection of DNA breaks and promotes immunoglobulin class switching,** Science, 339(6120): 711-5, 2013 Feb 8.

Bowman-Colin C, Xia B, Bunting SF, Klijn C, Drost R, Bouwman P, Fineman L, Chen X, Culhane AC, Bronson RT, Jonkers J, Nussenzweig A, Kanellopoulou C, Livingston, DM. **Palb2 synergizes with Trp53 to suppress mammary tumor formation in a model of inherited breast cancer,** PNAS in press 2013.

Barlow J, Faryabi RB, Callen E, Wong N, Malhowski A, Chen HT, Gutierez-Cruz G, Sun HW, McKinnon P, Wright G, Casellas R, Robbiani DF, Staudt L, Fernandez-Capetillo O, Nussenzweig A. **Identification of early replicating fragile sites that contribute to genome instability.** Cell, 152(3):620-32, 2013 Jan 31

Appendices

1. Di Virginio M, Callen E, Yamane A, Jankovic M, Gitlin AD, Feldhahn N, Resch W, Chait BT, Nussenzweig A, Casellas R, Robbiani DF, Nussenweig MC. **Rif1 prevents resection of DNA breaks and promotes immunoglobulin class switching,** Science, 339(6120): 711-5, 2013 Feb 8.

2. Barlow J, Faryabi RB, Callen E, Wong N, Malhowski A, Chen HT, Gutierez-Cruz G, Sun HW, McKinnon P, Wright G, Casellas R, Robbiani DF, Staudt L, Fernandez-Capetillo O, Nussenzweig A. **Identification of early replicating fragile sites that contribute to genome instability.** Cell, 152(3):620-32, 2013 Jan 31
3. Bowman-Colin C, Xia B, Bunting SF, Klijn C, Drost R, Bouwman P, Fineman L, Chen X, Culhane AC, Bronson RT, Jonkers J, Nussenzweig A, Kanellopoulou C, Livingston, DM. **Palb2 synergizes with Trp53 to suppress mammary tumor formation in a model of inherited breast cancer,** PNAS in press 2013.

Rif1 Prevents Resection of DNA Breaks and Promotes Immunoglobulin Class Switching

Michela Di Virgilio *et al.*

Science **339**, 711 (2013);
DOI: 10.1126/science.1230624

Science (print ISSN 0036-8075; online ISSN 1095-9203) is published weekly, except the last week in December, by the American Association for the Advancement of Science, 1200 New York Avenue NW, Washington, DC 20005.

higher numbers from colon contents than was the nitrate respiration–deficient mutant (Fig. 3H and fig. S8B). Collectively, these data suggested that nitrate respiration conferred a marked growth advantage on commensal *E. coli* in the lumen of the inflamed gut.

The picture emerging from this study is that nitrate generated as a by-product of the host inflammatory response can be used by *E. coli*, and likely by other commensal Enterobacteriaceae, to edge out competing microbes that rely on fermentation to generate energy for growth. Obligate anaerobic microbes in the intestine compete for nutrients that are available for fermentation but cannot use nonfermentable nutrients (such as fermentation end products). The ability to degrade nonfermentable substrates probably enables *E. coli* to sidestep this competition, which explains the fitness advantage conferred by nitrate respiration in the inflamed gut. Through this mechanism, inflammation contributes to a bloom of nitrate-respiration–proficient Enterobacteriaceae, providing a plausible explanation for the dysbiosis associated with intestinal inflammation (*3*–*12*). This general principle might also influence the dynamics of host-associated bacterial communities outside the large bowel, as nitrate respiration confers a fitness advantage in the oxygen-poor and nitrate-rich environment of the cystic fibrosis airway (*21*).

References and Notes

1. P. B. Eckburg *et al.*, *Science* **308**, 1635 (2005).
2. R. E. Ley *et al.*, *Proc. Natl. Acad. Sci. U.S.A.* **102**, 11070 (2005).
3. A. Krook, B. Lindström, J. Kjellander, G. Järnerot, L. Bodin, *J. Clin. Pathol.* **34**, 645 (1981).
4. M. H. Giaffer, C. D. Holdsworth, B. I. Duerden, *J. Med. Microbiol.* **35**, 238 (1991).
5. P. Seksik *et al.*, *Gut* **52**, 237 (2003).
6. U. Gophna, K. Sommerfeld, S. Gophna, W. F. Doolittle, S. J. Veldhuyzen van Zanten, *J. Clin. Microbiol.* **44**, 4136 (2006).
7. D. N. Frank *et al.*, *Proc. Natl. Acad. Sci. U.S.A.* **104**, 13780 (2007).
8. M. M. Heimesaat *et al.*, *PLoS ONE* **2**, e662 (2007).
9. C. Lupp *et al.*, *Cell Host Microbe* **2**, 119 (2007).
10. B. Stecher *et al.*, *PLoS Biol.* **5**, e244 (2007).
11. M. Barman *et al.*, *Infect. Immun.* **76**, 907 (2008).
12. W. S. Garrett *et al.*, *Cell Host Microbe* **8**, 292 (2010).
13. J. O. N. Lundberg, J. M. Lundberg, K. Alving, P. M. Hellström, *Lancet* **344**, 1673 (1994).
14. I. I. Singer *et al.*, *Gastroenterology* **111**, 871 (1996).
15. A. Enocksson, J. Lundberg, E. Weitzberg, A. Norrby-Teglund, B. Svenungsson, *Clin. Diagn. Lab. Immunol.* **11**, 250 (2004).
16. C. Szabó, H. Ischiropoulos, R. Radi, *Nat. Rev. Drug Discov.* **6**, 662 (2007).
17. C. Schöneich, *Biochim. Biophys. Acta* **1703**, 111 (2005).
18. B. Balagam, D. E. Richardson, *Inorg. Chem.* **47**, 1173 (2008).
19. R. B. Gennis, V. Stewart, in Escherichia coli *and* Salmonella. *Cellular and Molecular Biology*, F. C. Neidhardt *et al.*, Eds. (ASM Press, Washington, DC, 1996), vol. 1, pp. 217–261.
20. M. C. Pils *et al.*, *Inflamm. Bowel Dis.* **17**, 2038 (2011).
21. L. R. Hoffman *et al.*, *PLoS Pathog.* **6**, e1000712 (2010).

Acknowledgments: We thank W. Müller for providing *Il10*$^{flox/flox}$ *Cd4-cre* mice and E. Romao for technical assistance. The data reported in the manuscript are tabulated in the main paper and in the supplementary materials. This work was supported by the California Agricultural Experiment Station (I.E.P. and S.J.P.) and Public Health Service grants AI090387 (R.M.T), AI076246 (L.G.A and A.J.B.), and AI088122 (A.J.B.). P.T. was supported by a scholarship from the Faculty of Medicine, Chiang Mai University, Thailand.

Supplementary Materials

www.sciencemag.org/cgi/content/full/339/6120/708/DC1
Materials and Methods
Figs. S1 to S11
Tables S1 and S2
References (*22*–*39*)

7 November 2012; accepted 5 December 2012
10.1126/science.1232467

Rif1 Prevents Resection of DNA Breaks and Promotes Immunoglobulin Class Switching

Michela Di Virgilio,[1] Elsa Callen,[3]* Arito Yamane,[4]* Wenzhu Zhang,[5]* Mila Jankovic,[1] Alexander D. Gitlin,[1] Niklas Feldhahn,[1] Wolfgang Resch,[4] Thiago Y. Oliveira,[1,6,7] Brian T. Chait,[5] André Nussenzweig,[3] Rafael Casellas,[4] Davide F. Robbiani,[1] Michel C. Nussenzweig[1,2]†

DNA double-strand breaks (DSBs) represent a threat to the genome because they can lead to the loss of genetic information and chromosome rearrangements. The DNA repair protein p53 binding protein 1 (53BP1) protects the genome by limiting nucleolytic processing of DSBs by a mechanism that requires its phosphorylation, but whether 53BP1 does so directly is not known. Here, we identify Rap1-interacting factor 1 (Rif1) as an ATM (ataxia-telangiectasia mutated) phosphorylation-dependent interactor of 53BP1 and show that absence of Rif1 results in 5′-3′ DNA-end resection in mice. Consistent with enhanced DNA resection, Rif1 deficiency impairs DNA repair in the G_1 and S phases of the cell cycle, interferes with class switch recombination in B lymphocytes, and leads to accumulation of chromosome DSBs.

The DNA damage response factor p53 binding protein 1 (53BP1) is a multidomain protein containing a chromatin-binding tudor domain, an oligomerization domain, tandem breast cancer 1 (BRCA1) C-terminal (BRCT) domains, and an N-terminal domain with 28 SQ/TQ potential phosphorylation sites for phosphatidylinositol 3-kinase–related kinases [PIKKs, ataxia-telangiectasia mutated (ATM)/ATM and Rad3-related/DNA-dependent protein kinase catalytic subunit (DNA-PKcs)] (*1*–*3*). 53BP1 contributes to DNA repair in several ways: This protein facilitates joining between intrachromosomal double-strand breaks (DSBs) at a distance (synapsis) (*4*–*7*), it enables heterochromatic DNA repair through relaxation of nucleosome compaction (*2*, *3*), and it protects DNA ends from resection and thereby favors repair of DSBs that occur in G_1 phase by nonhomologous end joining (NHEJ) (*4*, *5*, *8*). Consistent with its role in DNA-end protection, 53BP1 is essential for class switch recombination (CSR) in B lymphocytes (*9*, *10*).

Structure-function studies indicate that, besides the recruitment of 53BP1 to DNA ends, protection requires 53BP1 phosphorylation (*4*), but how this protective effect is mediated is unknown. To identify phosphorylation-dependent interactors of 53BP1, we applied stable isotope labeling by amino acids in cell culture (SILAC). *Trp53bp1*$^{-/-}$ (*Trp53bp1* encodes 53BP1) B cells were infected with retroviruses encoding a C-terminal deleted version of 53BP1 (53BP1^{DB}) or a phosphomutant in which all 28 N-terminal potential PIKK phosphorylation sites were mutated to alanine (53BP1^{DB28A}) (*4*), in media containing isotopically heavy (53BP1^{DB}) or light (53BP1^{DB28A}) lysine and arginine (fig. S1, A to C) (*11*).

Most proteins coprecipitating with 53BP1^{DB} and 53BP1^{DB28A} displayed a $H/(H+L)$ ratio of ~0.5 (H, heavy; L, light), which is characteristic of phospho-independent association (average of 0.57 ± 0.09, peptide count: at least four) (Fig. 1 and table S1). Many of these proteins are nonspecific contaminants, but others such as KRAB-associated protein 1 (KAP-1), dynein light chain LC8-type 1 (Dynll1), Nijmegen breakage syndrome 1 (Nbs1), and H2AX represent authentic phospho-independent 53BP1-interacting proteins (fig. S1D). Three proteins displayed an abundance ratio that was more than four standard deviations (SDs) above the mean, indicating that these proteins interact specifically

[1]Laboratory of Molecular Immunology, The Rockefeller University, New York, NY 10065, USA. [2]Howard Hughes Medical Institute (HHMI), The Rockefeller University, New York, NY 10065, USA. [3]Laboratory of Genome Integrity and Center for Cancer Research, National Cancer Institute (NCI), National Institutes of Health (NIH), Bethesda, MD 20892, USA. [4]Genomics and Immunity and National Institute of Arthritis and Musculoskeletal and Skin Diseases (NIAMS), NCI, NIH, Bethesda, MD 20892, USA. [5]Laboratory of Mass Spectrometry and Gaseous Ion Chemistry, The Rockefeller University, New York, NY 10065, USA. [6]Department of Genetics, Faculty of Medicine, University of São Paulo, Ribeirão Preto, Brazil. [7]National Institute of Science and Technology for Stem Cells and Cell Therapy, Ribeirão Preto, Brazil.

*These authors contributed equally to this work.
†To whom correspondence should be addressed. E-mail: nussen@rockefeller.edu

with phosphorylated 53BP1: Pax interaction with transcription-activation domain protein-1 (Paxip1, or PTIP; 0.95), PTIP-associated protein 1 (Pa1; 0.97), and Rap1-interacting factor 1 (Rif1) (0.96) (Fig. 1 and figs. S1D and S2). PTIP was known to interact with 53BP1 in a phospho-dependent manner (*12*), whereas Pa1 and Rif1 were not.

Rif1 was originally identified in budding yeast as a protein with a key role in telomere length maintenance (*13*). However, in mammalian cells, Rif1 is not essential for telomere homeostasis, but has been assigned a number of different roles in maintaining genome stability, including participation in the DNA damage response (*14*–*16*), repair of S-phase DNA damage (*17*, *18*), and regulation of origin firing during DNA replication (*19*, *20*). However, the mechanism by which Rif1 might contribute to DNA repair and maintenance of genome stability is not known.

To confirm that Rif1 interaction with 53BP1 is dependent on phosphorylation, we performed Western blot analysis of Flag immunoprecipitates from lysates of irradiated *Trp53bp1*$^{-/-}$ B cells infected with retroviruses encoding 53BP1^{DB} or 53BP1^{DB28A}. Whereas Dynll1, a phospho-independent 53BP1 interactor (SILAC ratio: 0.55) (fig. S1D), coimmunoprecipitated with 53BP1^{DB} and 53BP1^{DB28A} to a similar extent (Fig. 2A), only 53BP1^{DB} coimmunoprecipitated with Rif1. We conclude that the interaction between 53BP1 and Rif1 is dependent on phosphorylation of 53BP1.

Ataxia-telangiectasia mutated phosphorylates 53BP1 in response to DSBs (*1*, *3*). To determine whether ATM induces DNA damage–dependent association between Rif1 and 53BP1, we compared irradiated and nonirradiated B cells in coimmunoprecipitation experiments. Although we detected small amounts of Rif1 in 53BP1^{DB} immunoprecipitates from unirradiated cells, this was increased by a factor of >3 after irradiation, and the increase was abrogated by treatment with the ATM inhibitor KU55933 (Fig. 2B). We conclude that Rif1 preferentially interacts with phosphorylated 53BP1 in a DNA damage- and ATM-dependent manner.

Rif1 is recruited to DNA damage foci by 53BP1 (*15*). To determine whether 53BP1 phosphorylation is required for Rif1 focus formation, we tested Rif1 foci in irradiated *Trp53bp1*$^{-/-}$ immortalized mouse embryonic fibroblasts (iMEFs), which were stably transduced with either 53BP1^{DB} or 53BP1^{DB28A}. Rif1 foci were readily detected and colocalized with 53BP1^{DB} (Fig. 2C). In contrast, although 53BP1^{DB28A} formed normal-appearing foci, Rif1 foci were rare and did not colocalize with 53BP1 (Fig. 2C). Furthermore, Rif1 recruitment to ionizing radiation–induced foci (IRIF) and colocalization with 53BP1 were abrogated in ATM-deficient but not DNA-PKcs–deficient iMEFs (fig. S3) (*15*). We conclude that Rif1 recruitment to DNA damage response foci is dependent on ATM-mediated 53BP1 phosphorylation.

The phosphorylation of 53BP1 is essential for CSR (*4*). To examine the role of Rif1 in joining DSBs during CSR, we conditionally ablated Rif1 in B cells using CD19^{Cre}, which is expressed specifically in B cells (*Rif1*$^{F/F}$*Cd19*$^{Cre/+}$ mice) (fig. S4, A to C). To induce CSR, B cells were activated with lipopolysaccharide (LPS) and interleukin-4 (IL-4) in vitro, and switching to immunoglobulin G1 (IgG1) or IgG3 was measured by flow cytometry. CSR to IgG1 and IgG3 was markedly reduced in *Rif1*$^{F/F}$*Cd19*$^{Cre/+}$ B cells, but less so than in *Trp53bp1*$^{-/-}$ controls (Fig. 3, A and B, and fig. S5). Switch junctions from *Rif1*$^{F/F}$*Cd19*$^{Cre/+}$ B cells were comparable to those from *Trp53bp1*$^{-/-}$ and wild-type controls (fig. S6) (*7*), which indicates that, similar to 53BP1 deficiency, absence of Rif1 does not alter the nature of productive CSR joining events.

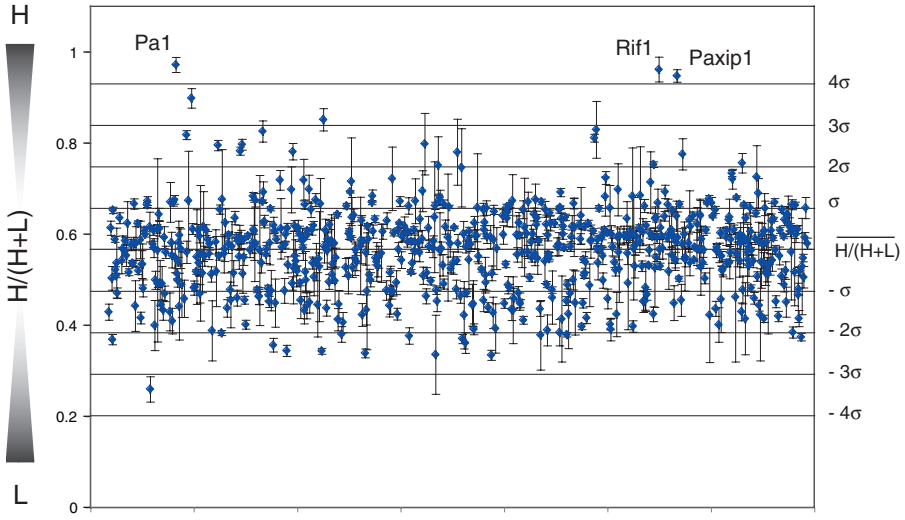

Fig. 1. Identification of phospho-dependent 53BP1 interactors. The graph shows the $H/(H + L)$ ratio distribution of proteins identified by SILAC. Error bars represent the SD of the $H/(H + L)$ mean value for all of the peptides identified for each individual protein (only proteins with at least four peptides were included). $\overline{H/(H + L)}$ and σ are the mean (0.57) and SD (0.09) of the distribution, respectively.

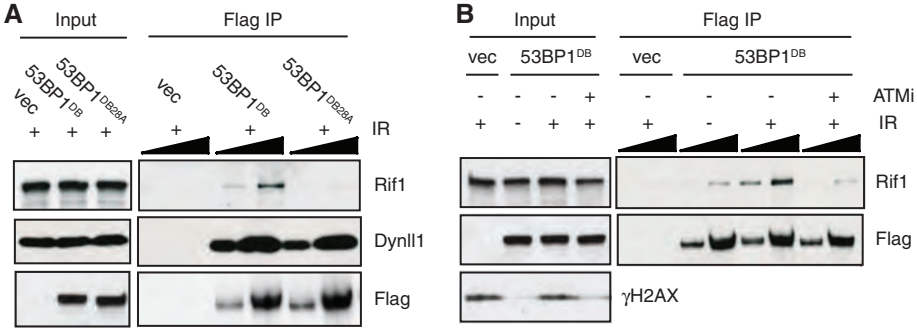

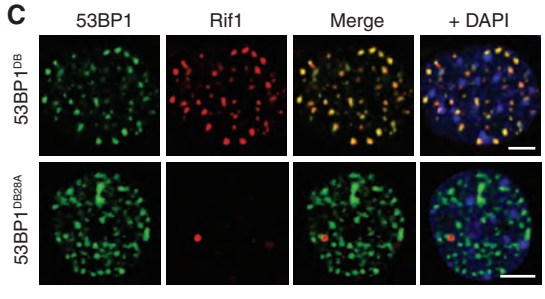

Fig. 2. Rif1 interaction with 53BP1 is dependent on phosphorylation, DNA damage, and ATM. (**A**) Western blot analysis of anti-Flag immunoprecipitates (IP) from irradiated (IR) *Trp53bp1*$^{-/-}$ B lymphocytes infected with empty vector (vec), 53BP1^{DB}, or 53BP1^{DB28A} virus. Triangles indicate threefold dilution. Data are representative of two independent experiments. (**B**) Western blot analysis of anti-Flag immunoprecipitates from *Trp53bp1*$^{-/-}$ B cells infected with empty vector or 53BP1^{DB}. Cells were either left untreated or irradiated [50 gray (Gy), 45-min recovery] in the presence or absence of the ATM kinase inhibitor KU55933 (ATMi). Triangles indicate threefold dilution. Data are representative of two independent experiments. (**C**) Immunofluorescent staining for 53BP1 (Flag) and Rif1 in irradiated *Trp53bp1*$^{-/-}$ iMEFs reconstituted with 53BP1^{DB} or 53BP1^{DB28A} retroviruses (*4*). Magnification, 100×; scale bars, 5 μm. Data are representative of two independent experiments. DAPI, 4′,6-diamidino-2-phenylindole.

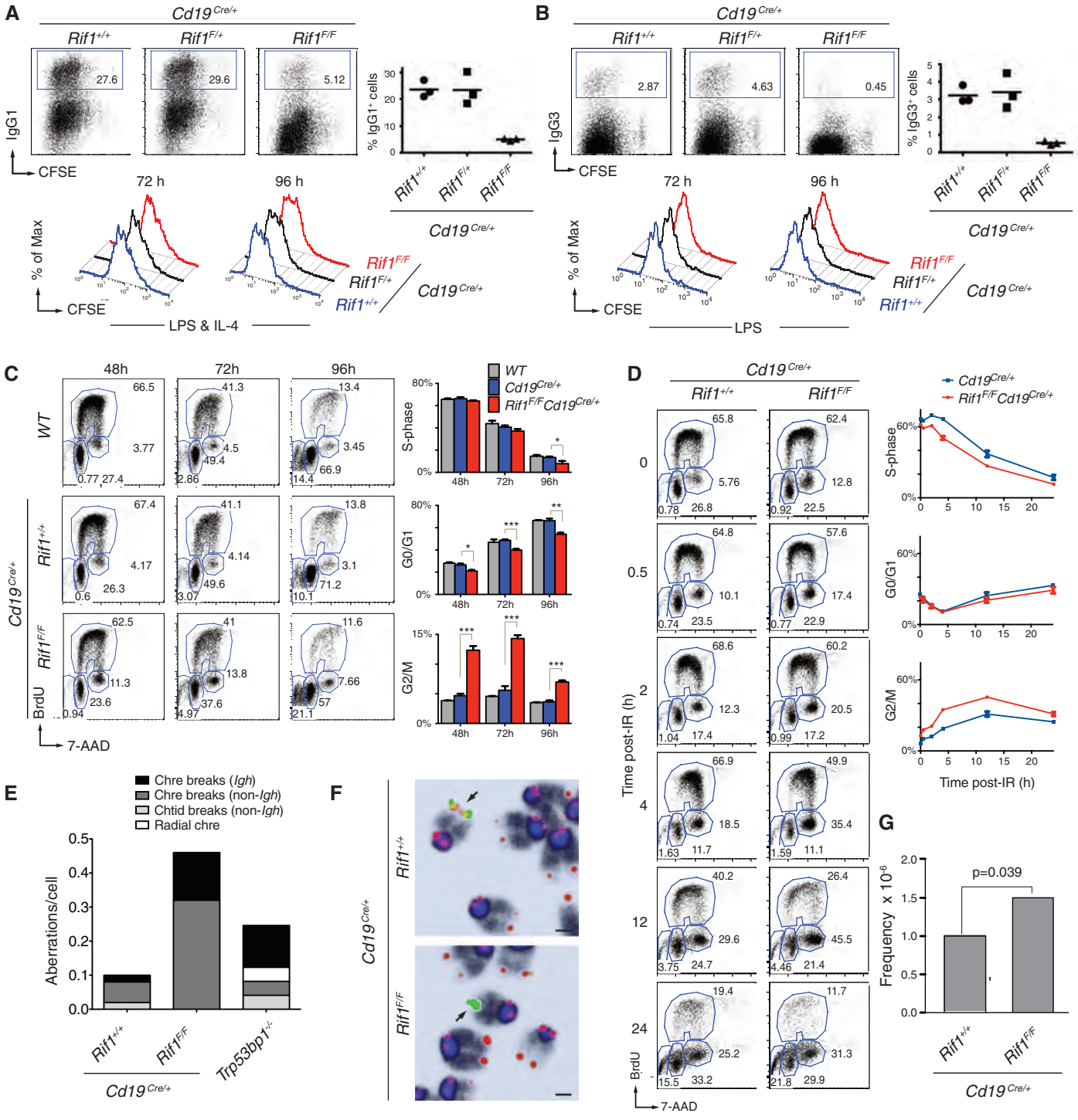

Fig. 3. Rif1 deficiency impairs CSR and causes *Igh* and genome instability in primary B cells. (**A**) (Left) CSR to IgG1 96 hours after stimulation of B lymphocytes with LPS and IL-4. (Right) Summary dot plot for three independent experiments (n = three mice per genotype). Mean values are: 23.6% for $Cd19^{Cre/+}$, 23.4% for $Rif1^{F/+}Cd19^{Cre/+}$, and 5.0% for $Rif1^{F/F}Cd19^{Cre/+}$ ($P < 0.008$ with the paired Student's t test). (Bottom) B cell proliferation by carboxyfluorescein succinimidyl ester (CFSE) dilution. Data are representative of three independent experiments. (**B**) Same as in (A) but for CSR to IgG3 after stimulation with LPS alone. Mean values are: 3.2% for $Cd19^{Cre/+}$, 3.4% for $Rif1^{F/+}Cd19^{Cre/+}$, and 0.5% for $Rif1^{F/F}Cd19^{Cre/+}$ ($P < 0.008$). (**C**) (Left) Cell cycle analysis of primary B cells after stimulation with LPS and IL-4. BrdU, 5-bromo-2′-deoxyuridine; 7-AAD, 7-amino-actinomycin D. (Right) Summary histograms for S, G_0/G_1, and G_2/M phase cells from two independent experiments (n = four mice per genotype). Error bars indicate SEM. * $0.01 < P < 0.05$, ** $0.001 < P < 0.01$, *** $P < 0.001$. WT, wild type. (**D**) (Left) Cell cycle analysis of LPS- and IL-4–stimulated splenocytes at the indicated times after irradiation (6 Gy). (Right) Summary graphs for S, G_0/G_1, and G_2/M phase cells from two independent experiments (n = three mice per genotype). Error bars indicate SD. (**E**) Analysis of genomic instability in metaphases from B cell cultures. Chtid, chromatid; Chre, chromosome. Data are representative of two independent experiments (n = 50 metaphases analyzed per genotype per experiment). (**F**) Examples of *Igh*-associated aberrations in $Rif1^{F/F}Cd19^{Cre/+}$ B cells. Chromosomes were hybridized with an *Igh* Cα probe (green; centromeric of Cγ1) and a telomere sequence-specific probe (red) and were counterstained with DAPI (dark blue/black). Arrows indicate *Igh* Cα/telomeric signal on chromosome 12. Magnification, 63×; scale bars, 1 μm. (**G**) Frequency of *c-myc/Igh* translocations in activated B cells. The graph shows combined results from three mice per genotype.

A similar CSR defect was also obtained by conditionally deleting Rif1 with 4-hydroxytamoxifen (4HT) in *Rif1*$^{F/F}$*ROSA26*$^{Cre\text{-}ERT2/+}$ B cells (fig. S7). Finally, short hairpin RNA–mediated partial down-regulation of CtBP-interacting protein (CtIP), which interacts with Rif1 (fig. S8C) and has been implicated in processing of DNA ends (*21*, *22*), resulted in a very small but reproducible increase in CSR (fig. S8, A and B). Thus, Rif1 is essential for normal CSR, and CtIP may not be the only factor that contributes to end processing in Rif1-deficient B cells.

Class switch recombination requires cell division, activation-induced cytidine deaminase (AID) expression, and *Igh* germline transcription (*23*). There are conflicting reports that Rif1 is required for proliferation in MEFs, but not in DT40 B cells (*17*, *18*). We found that cell division profiles of *Rif1*$^{F/F}$*Cd19*$^{Cre/+}$ and 4HT-treated *Rif1*$^{F/F}$*ROSA26*$^{Cre\text{-}ERT2/+}$ B cells were indistinguishable from controls (Fig. 3, A and B; and fig. S7, A, C, E, and G), indicating that Rif1 is dispensable for B cell proliferation in vitro. Finally, AID mRNA and protein expression and *Igh* germline transcription were not affected by Rif1 deletion (fig. S4, B and D).

We next examined the role of Rif1 in cell cycle progression in primary B cells. We found no major differences in the percentage of cells in G_0/G_1 and S phases (Fig. 3C). However, the number of cells in G_2/M phase was increased approximately twofold in the absence of Rif1 (2.64-, 2.56-, and 1.91-fold at 48, 72, and 96 hours, respectively) (Fig. 3C). We obtained similar results with the use of *Rif1*$^{F/F}$*ROSA26*$^{Cre\text{-}ERT2/+}$ B cells treated with 4HT (fig. S7, H and I).

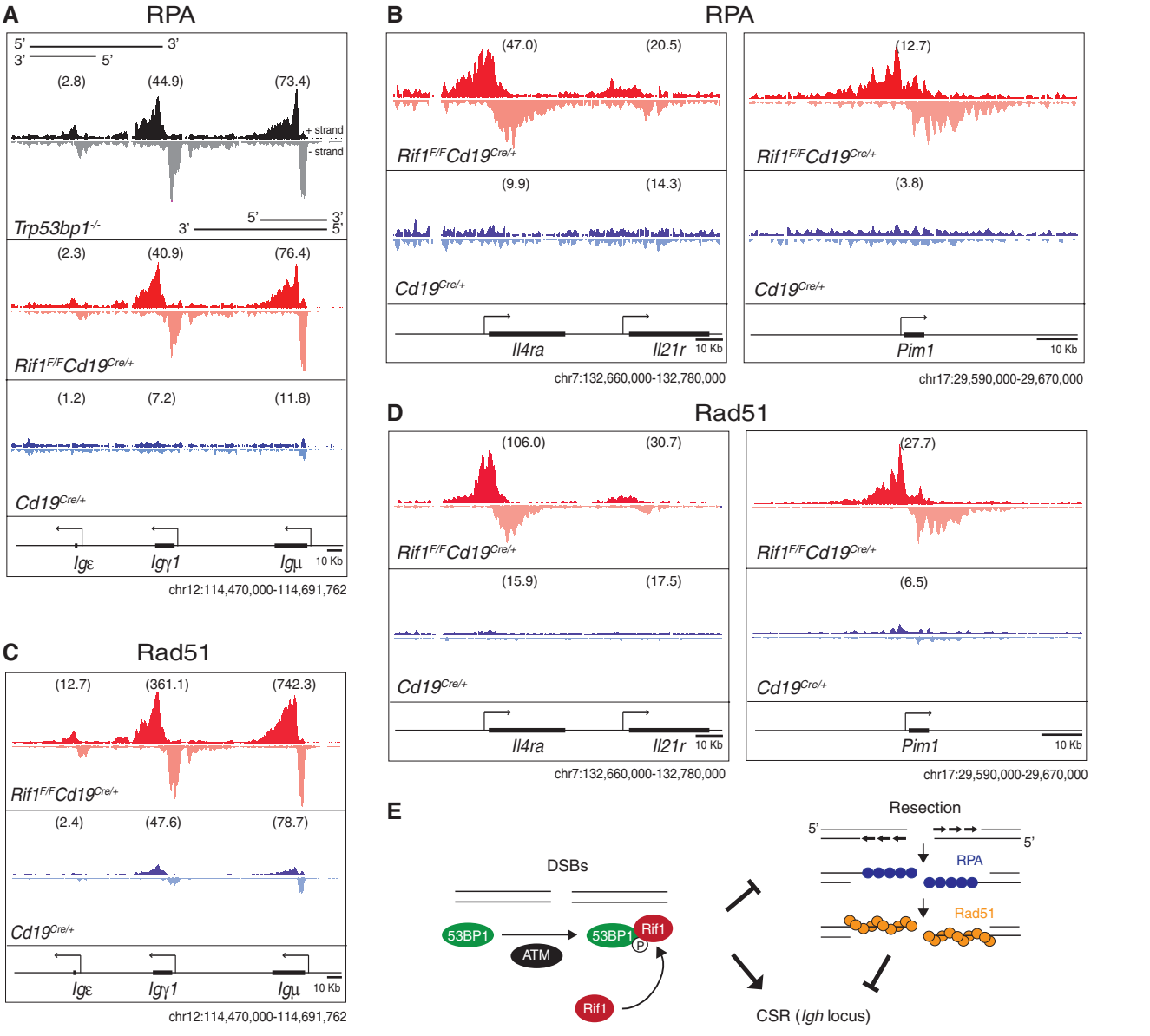

Fig. 4. Rif1 prevents resection of DNA ends at sites of AID-induced DNA damage. (**A** to **D**) RPA and Rad51 occupancy at the *Igh* locus (A and C) and at non-*Igh* AID targets genes (B and D) in B cells activated to undergo class switching. ChIP-seq libraries were resolved into upper (+) and lower (-) DNA strands to show RPA and Rad51 association with sense and antisense strands. Within a specified genomic window, graphs have the same scale and show tag density. Deep-sequencing samples were normalized per library size, and tags per million values were calculated for each genic region, as indicated in the supplementary materials and methods and shown in parenthesis. Data are representative of two independent experiments for RPA ChIP-seq and one for Rad51. (**E**) Model of Rif1 recruitment and DNA-end protection at DSBs. DNA damage activates ATM, which phosphorylates many targets, including 53BP1. This event recruits Rif1 to 53BP1 at the DSB, where it inhibits DNA resection. The extensive resection in the absence of Rif1 impairs CSR at the *Igh* locus. P, phosphate.

Furthermore, irradiation increases the accumulation of $Rif1^{F/F}Cd19^{Cre/+}$ B cells in G2/M phase (Fig. 3D). In addition, $Trp53bp1^{-/-}$ iMEFs expressing $53BP1^{DB28A}$, which did not recruit Rif1 to IRIF (Fig. 2C), exhibited delayed progression through S phase following DNA damage with accumulation of cells in G_2 phase after irradiation (fig. S9).

Accumulation of cells in G_2/M phase may reflect the persistence of unrepaired DNA damage in a fraction of Rif1-deficient cells. To investigate this possibility, we analyzed metaphase spreads from B cells dividing in response to LPS and IL-4 in vitro. These cells express AID, which produces DSBs in *Igh* and, less frequently at off-target sites throughout the genome, in the G_1 phase of the cell cycle (*24*–*26*). Chromosomal aberrations were increased in $Rif1^{F/F}Cd19^{Cre/+}$ B cells compared to controls (Fig. 3E), with many localized to the *Igh* locus (Fig. 3E). Consistent with the observation that *Igh* is targeted by AID in the G_1 phase of the cell cycle, all of the *Igh* breaks were chromosome breaks (Fig. 3, E and F). Interestingly, the frequency of *c-myc/Igh* translocations is moderately increased in $Rif1^{F/F}Cd19^{Cre/+}$ B cells; however, the breakpoint distribution was similar to the $Cd19^{Cre/+}$ control (1.5×10^{-6} versus 1.0×10^{-6} in the control; $P = 0.039$) (Fig. 3G and fig. S10). We conclude that in the absence of Rif1, DSBs fail to be resolved efficiently in the G_1, S, or G_2 phases, which leads to increased levels of genomic instability, including chromosome breaks at *Igh* and translocations in dividing B cells.

In the absence of 53BP1, DSBs produced by AID at the *Igh* locus accumulate the single-stranded DNA-binding replication protein A complex (RPA) as a result of increased DNA-end resection (*24*). To determine if Rif1 is required for DNA-end protection by 53BP1, we performed RPA–chromatin immunoprecipitation followed by massive parallel sequencing (ChIP-seq) experiments on $Rif1^{F/F}Cd19^{Cre/+}$ and control B cells. Ablation of Rif1 was indistinguishable from the loss of 53BP1 in that in its absence, RPA decorates the *Igh* locus asymmetrically, in a manner consistent with 5′-3′ resection (Fig. 4A) (*27*). In addition, absence of Rif1 also results in RPA accumulation at non-*Igh* genes, such as *Il4ra* and *Pim1*, that are damaged by AID in G_1 phase (Fig. 4B) (*24*, *25*). Rad51 is the recombinase that mediates repair of DSBs by homologous recombination in S/G_2/M phase (*22*). To confirm that Rif1 prevents resection that takes place in S phase, we monitored Rad51 accumulation in activated B cells by ChIP-seq. Loss of Rif1 was indistinguishable from the loss of 53BP1 (*27*), in that it led to asymmetric Rad51 accumulation at sites of AID-inflicted DNA damage (Fig. 4, C and D). We conclude that in the absence of Rif1, AID-induced DSBs incurred in G_1 phase persist and undergo extensive 5′-3′ DNA-end resection in S/G_2/M phase, as measured by RPA and Rad51 accumulation.

A role for Rif1 in maintenance of genome stability and protection of DNA ends against resection is consistent with its phosphorylation-dependent recruitment to the N-terminal domain of 53BP1 (*4*). 53BP1 facilitates DNA repair and prevents DNA-end resection during CSR. In the absence of 53BP1, AID-induced DSBs are resolved inefficiently in G_1 phase, leading to chromosome breaks, *Igh* instability, and resolution by alternative NHEJ or homologous recombination instead of classical NHEJ (*4*, *8*, *27*). Our experiments show that in the absence of Rif1, 53BP1 is insufficient to promote genomic stability or mediate efficient *Igh* repair, DNA-end protection, or CSR. Thus, these 53BP1 activities require Rif1 recruitment to the phosphorylated N terminus of 53BP1. Rif1 is likely to have additional functions beyond 53BP1, CSR, and DNA-end protection because although $Trp53bp1^{-/-}$ mice are viable, Rif1 deletion is lethal (*17*). Indeed, Rif1 is believed to play a role in the repair of S-phase DNA damage (*17*, *18*), as well as in the regulation of replication timing (*19*, *20*, *28*). Analogously, additional CSR factor(s) may exist downstream of 53BP1, as class switching in Rif1-deficienct B cells is significantly higher than in $Trp53bp1^{-/-}$.

In summary, our data are consistent with a model in which ATM-mediated phosphorylation of 53BP1 recruits Rif1 to sites of DNA damage, where it facilitates DNA repair in part by protecting DNA ends from resection (Fig. 4E). In the absence of Rif1, DNA breaks incurred in G_1 phase fail to be repaired by NHEJ and undergo extensive 5′-3′ end resection, resulting in the accumulation of chromosome breaks and genome instability.

References and Notes

1. M. M. Adams, P. B. Carpenter, *Cell Div.* **1**, 19 (2006).
2. J. Lukas, C. Lukas, J. Bartek, *Nat. Cell Biol.* **13**, 1161 (2011).
3. A. T. Noon, A. A. Goodarzi, *DNA Repair* **10**, 1071 (2011).
4. A. Bothmer *et al.*, *Mol. Cell* **42**, 319 (2011).
5. S. Difilippantonio *et al.*, *Nature* **456**, 529 (2008).
6. N. Dimitrova, Y. C. Chen, D. L. Spector, T. de Lange, *Nature* **456**, 524 (2008).
7. B. Reina-San-Martin, J. Chen, A. Nussenzweig, M. C. Nussenzweig, *Eur. J. Immunol.* **37**, 235 (2007).
8. A. Bothmer *et al.*, *J. Exp. Med.* **207**, 855 (2010).
9. J. P. Manis *et al.*, *Nat. Immunol.* **5**, 481 (2004).
10. I. M. Ward *et al.*, *J. Cell Biol.* **165**, 459 (2004).
11. Materials and methods are available as supplementary materials on *Science* Online.
12. I. A. Manke, D. M. Lowery, A. Nguyen, M. B. Yaffe, *Science* **302**, 636 (2003).
13. C. F. Hardy, L. Sussel, D. Shore, *Genes Dev.* **6**, 801 (1992).
14. S. Kumar *et al.*, *Cell Cycle* **11**, 1183 (2012).
15. J. Silverman, H. Takai, S. B. Buonomo, F. Eisenhaber, T. de Lange, *Genes Dev.* **18**, 2108 (2004).
16. L. Xu, E. H. Blackburn, *J. Cell Biol.* **167**, 819 (2004).
17. S. B. Buonomo, Y. Wu, D. Ferguson, T. de Lange, *J. Cell Biol.* **187**, 385 (2009).
18. D. Xu *et al.*, *EMBO J.* **29**, 3140 (2010).
19. D. Cornacchia *et al.*, *EMBO J.* **31**, 3678 (2012).
20. S. Yamazaki *et al.*, *EMBO J.* **31**, 3667 (2012).
21. A. A. Sartori *et al.*, *Nature* **450**, 509 (2007).
22. L. S. Symington, J. Gautier, *Annu. Rev. Genet.* **45**, 247 (2011).
23. R. Pavri, M. C. Nussenzweig, *Adv. Immunol.* **110**, 1 (2011).
24. O. Hakim *et al.*, *Nature* **484**, 69 (2012).
25. S. Petersen *et al.*, *Nature* **414**, 660 (2001).
26. A. Yamane *et al.*, *Nat. Immunol.* **12**, 62 (2011).
27. A. Yamane *et al.*, *Cell Rep.* 10.1016/j.celrep.2012.12.006 (2013).
28. M. Hayano *et al.*, *Genes Dev.* **26**, 137 (2012).

Acknowledgments: We thank all members of the Nussenzweig laboratory for discussion, D. Bosque and T. Eisenreich for help in managing mouse colonies, A. Gazumyan for assistance with *Igh* germline and AID transcript levels analysis, and K. Yao for help with genotyping. We thank T. de Lange (The Rockefeller University, New York) for $Rif1^{F/F}$ mice; S. Buonomo (European Molecular Biology Laboratory Mouse Biology Unit, Monterotondo, Italy) for the anti-mouse Rif1 serum #1240; G. Gutierrez (NIAMS, NIH, Bethesda, MD) for Illumina sequencing; N. Zampieri (Columbia University, New York) for assistance with immunofluorescence image processing, and M. P. Rout, J. LaCava, S. Obado, and L. Hough (The Rockefeller University) for invaluable help, discussions, and protocols for cryolysis and magnetic bead-mediated immunoisolation. The data presented in the manuscript are tabulated in the main text and in the supplementary materials. Sequence data shown in Fig. 4 have been deposited in the Gene Expression Omnibus database (accession number GSE42298) at www.ncbi.nlm.nih.gov/geo/. M.D.V. was a Fellow of the American Italian Cancer Foundation, and A.D.G. was supported by NIH Medical Scientist Training Program grant GM007739. This work was supported in part by NIH grants AI037526 (M.C.N.), RR022220 (B.T.C.), RR00862 (B.T.C.), and GM103314 (B.T.C.); and by the intramural program of NIAMS at the NIH (R.C.); and the intramural research program of NCI at the NIH and Center for Cancer Research (A.N. and E.C.). M.C.N. is an HHMI Investigator.

Supplementary Materials

www.sciencemag.org/cgi/content/full/science.1230624/DC1
Materials and Methods
Figs. S1 to S10
Table S1
References (*29*–*49*)

24 September 2012; accepted 16 November 2012
Published online 10 January 2013;
10.1126/science.1230624

Cell

Identification of Early Replicating Fragile Sites that Contribute to Genome Instability

Jacqueline H. Barlow,[1,9] Robert B. Faryabi,[1,9] Elsa Callén,[1] Nancy Wong,[1] Amy Malhowski,[1] Hua Tang Chen,[1] Gustavo Gutierrez-Cruz,[3] Hong-Wei Sun,[4] Peter McKinnon,[6] George Wright,[2] Rafael Casellas,[5] Davide F. Robbiani,[7] Louis Staudt,[2] Oscar Fernandez-Capetillo,[8] and André Nussenzweig[1,*]

[1]Laboratory of Genome Integrity
[2]Metabolism Branch Center for Cancer Research
National Cancer Institute, NIH, Bethesda, Maryland 20892, USA
[3]Laboratory of Muscle Stem Cells and Gene Regulation
[4]Biodata Mining and Discovery Section, Office of Science and Technology
[5]Laboratory of Immunogenetics
National Institute of Arthritis and Musculoskeletal and Skin Diseases, NIH, Bethesda, MD 20892, USA
[6]Department of Genetics, St. Jude Children's Research Hospital, Memphis, TN 38105, USA
[7]Laboratory of Molecular Immunology, The Rockefeller University, New York, NY 10065, USA
[8]Genomic Instability Group, Spanish National Cancer Research Centre (CNIO), E-28029 Madrid, Spain
[9]These authors contributed equally to this work
*Correspondence: andre_nussenzweig@nih.gov
http://dx.doi.org/10.1016/j.cell.2013.01.006

SUMMARY

DNA double-strand breaks (DSBs) in B lymphocytes arise stochastically during replication or as a result of targeted DNA damage by activation-induced cytidine deaminase (AID). Here we identify recurrent, early replicating, and AID-independent DNA lesions, termed early replication fragile sites (ERFSs), by genome-wide localization of DNA repair proteins in B cells subjected to replication stress. ERFSs colocalize with highly expressed gene clusters and are enriched for repetitive elements and CpG dinucleotides. Although distinct from late-replicating common fragile sites (CFS), the stability of ERFSs and CFSs is similarly dependent on the replication-stress response kinase ATR. ERFSs break spontaneously during replication, but their fragility is increased by hydroxyurea, ATR inhibition, or deregulated c-Myc expression. Moreover, greater than 50% of recurrent amplifications/deletions in human diffuse large B cell lymphoma map to ERFSs. In summary, we have identified a source of spontaneous DNA lesions that drives instability at preferred genomic sites.

INTRODUCTION

Double-strand breaks (DSBs) arise spontaneously during DNA replication, as a result of oncogenic stress, and as a part of the gene diversification programs in lymphocytes (Bartek et al., 2007; Callén et al., 2007; Gostissa et al., 2011; Halazonetis et al., 2008). When B lymphocytes are activated, they undergo rapid proliferation and simultaneously initiate two-genome remodeling reactions, termed somatic hypermutation (SHM) and class switch recombination (CSR). The coupling of rapid cycling and programmed DNA damage poses the B cell genome at high risk for destabilization.

SHM introduces point mutations in the variable region of immunoglobulin (Ig) genes, which can increase antibody affinity, whereas CSR is a DNA deletion event that replaces one Ig constant region gene for another. Both of these reactions are initiated by the enzyme activation-induced cytidine deaminase (AID), which deaminates cytosine residues in single-stranded DNA exposed during Ig gene transcription (Chaudhuri and Alt, 2004). In addition to Ig genes, AID causes a considerable amount of collateral genomic damage (Chiarle et al., 2011; Kato et al., 2012; Klein et al., 2011; Liu et al., 2008), including oncogenic targets such as c-Myc (Robbiani et al., 2008). Nevertheless, many recurrent mutations in B cell lymphoma are not associated with AID activity, and the mechanisms of rearrangements at these sites remain unclear.

The DNA damage response (DDR) is activated during programmed rearrangements in lymphocytes to ensure faithful DNA repair and prevent chromosomal translocation (Chen et al., 2000; Petersen et al., 2001). The DDR is also triggered by aberrant oncogene expression that induces precocious entry into S phase and perturbs replication fork progression (Bartek et al., 2007; Bester et al., 2011; Halazonetis et al., 2008). Replication fork instability can also be triggered by exogenous agents such as hydroxyurea (HU), which depletes deoxynucleotide pools, or by deficiencies in homologous recombination pathways that are needed to complete DNA replication after fork stalling or collapse (Schlacher et al., 2012).

Oncogenic stress has been shown to preferentially target genomic regions called common fragile sites (CFSs) (Bartek et al., 2007; Halazonetis et al., 2008). Historically, CFSs have been mapped in lymphocytes but are induced in all cell types under conditions that obstruct replication, such as treatment with low doses of the DNA polymerase inhibitor aphidicolin. DNA breakage within CFSs spans megabase regions. Nevertheless, CFSs share characteristic features including association with very large genes, enrichment of long stretches of AT dinucleotide-rich repeats, and incomplete DNA replication (Durkin and Glover, 2007).

Replication-stress-induced DNA damage is also observed in yeast. Similar to CFSs, sites located in "replication slow zones" (RSZs) are late replicating and breakage prone (Cha and Kleckner, 2002). In addition to late replicating areas, irreversible replication fork collapse in response to acute doses of hydroxyurea has been observed preferentially around a subset of early firing replication origins in yeast (Raveendranathan et al., 2006), which do not overlap with RSZs (Cha and Kleckner, 2002; Hashash et al., 2011). Although the molecular mechanisms governing replication initiation in yeast and mammalian cells are distinct, we wondered if fragility at early firing origins is also a feature of mammalian cells. Here, we identify highly unstable regions of the B cell genome designated as "early replicating fragile sites" (ERFSs). We propose that ERFSs are a new class of fragile sites in mammalian cells that contribute to recurrent rearrangements during lymphomagenesis.

RESULTS

Genome-wide Mapping of Replication-Induced DNA Damage

Single-strand DNA (ssDNA) mapping has been used to localize origins of replication in yeast (Feng et al., 2006). To identify potential sites of fork collapse, we first profiled the location and extent of ssDNA genome-wide using chromatin immunoprecipitation (ChIP) with an anti-replication protein A (RPA) antibody (Figure 1). RPA associates with ssDNA at stalled forks near early firing origins when fork movement is inhibited by HU (Tanaka and Nasmyth, 1998).

Freshly isolated mouse B cells are arrested in the G_0 phase of the cell cycle (Figure 1A). Upon stimulation with LPS/IL4, cells synchronously enter into the cell cycle so that by 22 hr, approximately 8% of cells have entered S phase, whereas at 28 hr over 30% are in S/G2 phases (Figure 1A). To profile early replication origins, we treated cells at 22 hr with 10 mM HU for 6 hr to fully arrest cells at G_1/S (Figures 1A and 1B). We then performed ChIP-seq of RPA in both untreated and HU-treated cells at 28 hr (Figures 1A and 1B). Two independent experiments showed reproducibility of genome-wide RPA association in HU-treated cells (Figure S1A available online). We generated profiles of RPA in untreated and treated samples, centered on individual RPA-bound sites (Figure S1B), and observed a marked increase in the intensity of RPA in HU-treated B cells relative to untreated cells where 5,939 out of 11,942 genomic regions (49.7%) displayed more than a 4-fold increase in RPA recruitment. In addition to the 53% overlap of RPA-associated regions between HU-untreated versus -treated cells, we also observed that 1,441 regions were present only in HU-treated samples (Figure S1B). These HU-dependent ssDNA regions may correspond to the firing of new replication origins to compensate for inefficient replication.

To confirm that RPA recruitment maps early replication zones, we used the Repli-Seq approach (Hansen et al., 2010) to identify replication origins in B cells during HU arrest. Approximately 12,000 early activating replication origins across the murine B cell genome were identified (Figure S1C). By comparing the distribution of BrdU incorporation relative to the individual RPA-occupied genomic regions, we observed association of BrdU incorporation with nearly 80% of RPA-bound regions (Figure S1C). Moreover, more than 86% of RPA/BrdU enriched genomic sites coincided with previously mapped early replicating regions in the mouse B cell line CH12 (Stamatoyannopoulos et al., 2012) ($p(permutation) < 1 \times 10^{-5}$, Figure S1D). Thus, HU-arrested B cells exhibited an enrichment of RPA at early replicating zones, consistent with an early S phase cell-cycle arrest (Figure 1A).

Early replicating regions are associated with accessible chromatin configuration (MacAlpine et al., 2004). In agreement with this, we found that more than 67% of RPA-bound regions in HU-arrested cells reside within intragenic sequences (Figures S1E and S1I), a frequency significantly higher than expected ($p(permutation) < 1 \times 10^{-5}$). Moreover, RPA preferentially associated with DNaseI hypersensitive sites (DHS) and euchromatic promoters marked by H3K4me3 (Figure S1F). Finally, we measured transcriptional activity in HU-treated B cells directly by genome-wide RNA sequencing. We observed high transcription activity within the RPA-occupied genomic regions as shown by the aggregated pattern of RNA-Seq centered on those regions (Figure S1G). Moreover, 6,100 RPA-bound RefSeq genes exhibited significantly higher average mRNA abundance than those that did not show RPA binding ($p < 1 \times 10^{-16}$, Figure S1H). Thus, HU-induced RPA recruitment in early S phase maps to actively transcribed genes that show the hallmarks of euchromatin.

Replisome stalling in response to HU triggers the activation of the ATR kinase (Ward and Chen, 2001), which protects forks from collapse (Cimprich and Cortez, 2008), and leads to phosphorylation of H2AX (γ-H2AX) (Ward and Chen, 2001), which colocalizes with RPA (Petermann et al., 2010). To examine the relative distribution of γ-H2AX and RPA genome-wide, we carried out ChIP-seq with an antibody that recognizes γ-H2AX (Figure S1A) and examined their profiles with respect to the center of RPA-bound sites. γ-H2AX-associated genomic regions were much broader than RPA, but these regions overlapped with 93% of RPA-bound sites marking ssDNA in HU-treated cells (Figure 1C), consistent with the finding that γ-H2AX marks stalled forks even prior to DSB formation (Petermann et al., 2010). γ-H2AX/RPA enriched loci may therefore correspond to a combination of stalled and broken replisomes.

Cells deficient in homologous recombination (HR) pathway components, such as XRCC2, often accumulate spontaneous chromosome breaks and exhibit hypersensitivity to HU (Sonoda et al., 1998). Consistent with increased spontaneous DNA damage at replication forks, untreated *XRCC2*$^{-/-}$ cells exhibited accumulation of γ-H2AX at similar genomic regions and at almost similar levels observed in HU-treated wild-type (WT)

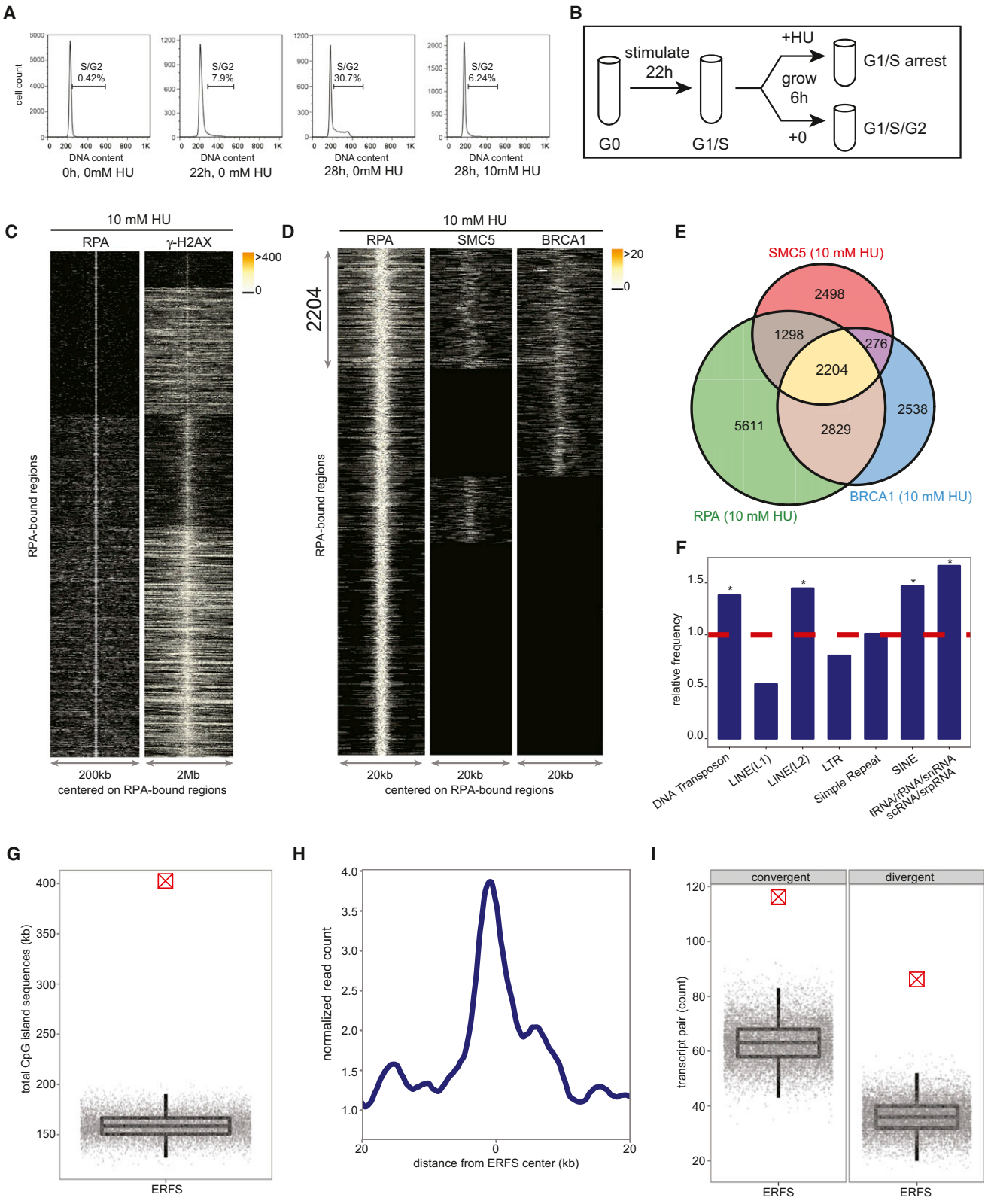

Figure 1. Mapping Replication-Induced DNA Damage in Murine B Lymphocytes

(A) FACS analysis showing DNA content of freshly isolated and ex vivo stimulated splenic murine B lymphocytes in the absence and presence of 10 mM HU.

(B) Experimental plan describing cell synchronization and isolation for samples used in ChIP-seq and RNA-Seq experiments.

(legend continued on next page)

B cells (Figures S2A–S2C). 90% of γ-H2AX-associated genomic regions in untreated *XRCC2*$^{-/-}$ cells correlate with the regions enriched for this protein in HU-treated WT B cells (Figure S2B), and nearly 80% of the regions with enriched γ-H2AX observed in HU-treated WT B cells overlapped with those seen in HU-treated *XRCC2*$^{-/-}$ cells (Figure S2C). These data indicate that XRCC2 deficiency leads to increased endogenous levels of replication stress mostly at the same loci where HU induces replication fork stalling and/or breakage in WT cells.

RPA, BRCA1, and SMC5 Colocalization Marks the Sites of Replication Stress in Early Replicating Zones

Like XRCC2, BRCA1 and members of the structural maintenance of chromosome (SMC) family have been implicated in promoting replication fork restart (Schlacher et al., 2012; Stephan et al., 2011). To determine whether HR proteins bind to a subset of stalled forks marked by RPA and γ-H2AX, we also defined the genome-wide profile of BRCA1 and SMC5. We confirmed BRCA1 and SMC5 ChIP-seq efficacy by observing their association at both Sμ and Sγ1 in *53BP1*$^{-/-}$ cells, where the breaks in IgH persist unrepaired and undergo extensive resection (Figure S3A) (Bothmer et al., 2010; Bunting et al., 2010, 2012; Yamane et al., 2011, 2013).

We then determined the localization of BRCA1 and SMC5 in HU-arrested B cells. Two independent experiments showed reproducibility of genome-wide BRCA1 and SMC5 association (Figures S3B and S3C). To identify the RPA genomic sites co-occupied by the HR proteins BRCA1 and SMC5, we plotted the distribution of their binding with respect to the center of individual RPA-bound regions. Overall, 2,204 regions spanning 10 kbp on average showed RPA/BRCA1/SMC5 triple colocalization (Figures 1D and 1E). We found that RPA was recruited to more than 88% of genomic sites exhibiting BRCA1 and SMC5 association (Figure 1E). Furthermore, genome-wide analysis of RPA/BRCA1/SMC5 profiles in untreated cells revealed more than a 21% increase in the number of genomic regions occupied by these three proteins after HU treatment (Figure S4A). Nevertheless, 48% of RPA/BRCA1/SMC5 triple colocalizations were common between the unperturbed and HU-arrested B cells (Figure S4A). Therefore, we hypothesized that chromatin with concomitant RPA, BRCA1, and SMC5 binding might correspond to regions undergoing replication fork collapse both in response to replication stress and during normal DNA replication. Given that our analysis focused on early replicating sites, which contrasts with late replicating CFSs, we designated these regions as ERFSs.

We then characterized ERFSs to determine whether they share common underlying primary sequence characteristics. Indeed, these loci were enriched at known repetitive elements, including LINE L2, SINE, DNA transposons, and tRNA elements (p(permutation) $< 1 \times 10^{-3}$, Figure 1F), which are known replication fork barriers (Mirkin and Mirkin, 2007). Furthermore, ERFSs showed significantly higher G and C nucleotide content compared to the whole mouse genome, in contrast to CFSs that are enriched in A+T sequences (p(Wilcoxon) $< 1 \times 10^{-16}$, Figure S4B). Twenty-six percent of the ERFSs regions overlapped with CpG islands, which are highly enriched at translocation breakpoints in B cell lymphoma (Tsai et al., 2008). Conversely, CpG islands covered approximately 400,000 nucleotides within these regions (p(permutation) $< 1 \times 10^{-5}$, Figure 1G). As anticipated, ERFSs clustered at early replication origins (Figure S4C), and over 66% of the loci overlapped with intragenic or promoter sequences of RefSeq annotated protein coding genes (p(permutation) $< 1 \times 10^{-3}$, Figures S4D and S4E). Moreover, ERFSs are more transcriptionally active relative to flanking genomic regions shown by relative mRNA enrichment by RNA-Seq (Figure 1H). Indeed, more than 86% of the RefSeq annotated genes with ERFSs are among the highest transcribed genes (p(binomial) $< 1 \times 10^{-16}$, Figure S4F). Finally, ERFSs were significantly enriched in gene pairs that are transcribed in converging or diverging directions (see Experimental Procedures), such as the convergent transcription pair of *IKZF1* and *FIGNL1* shown in Figure 2A. Compared to expected values, ERFSs were at least two times more likely to localize in regions containing gene pairs exhibiting convergent and/or divergent gene pairs (p(permutation) $< 1 \times 10^{-5}$, Figure 1I).

(C) For each RPA-bound site in response to 10 mM HU (y axis), each column depicts the presence of RPA (left) and γ-H2AX (right) within a window centered on the RPA-bound sites. Color map corresponds to binding intensities where "black" represents no binding. K-mean clustering algorithm was used to group the protein-bound sites.

(D) RPA, SMC5, and BRCA1 co-occupy 2,204 genomic regions in response to 10 mM HU. The plot in each column, from left to right, represents the pattern of RPA, SMC5, and BRCA1 genomic occupancy in response to HU centered on RPA-bound sites. K-mean clustering algorithm is used to group the protein-bound sites.

(E) The Venn diagram shows the overlap of sites bound by RPA, SMC5, and BRCA1 in response to 10 mM HU. The total number of bound sites is indicated for each shared and unique area.

(F) Relative frequency of ERFSs in classes of repetitive sequences is shown. Dashed line indicates the expected frequency based on the permutation model (*, enriched repetitive element classes; $p < 1 \times 10^{-3}$).

(G) ERFSs are enriched in CpG islands. Total CpG island sequences in all the 2,204 ERFSs as indicated by the crossed red point is compared to the permutation model as indicated by the gray points. Each gray point corresponds to the total CpG island sequences covered in an iteration of the permutation model. The box plot depicts the quantiles of total CpG sequences based on the permutation model ($p < 1 \times 10^{-5}$).

(H) ERFS genomic regions are transcriptionally active. The line plot represents the average RNA tag count (loess smoothed) in a genomic window around the center of the ERFSs.

(I) ERFSs are enriched in transcriptionally active convergent and divergent gene pairs. Count of divergent/convergent gene pairs coinciding with ERFSs as indicated by the crossed red point is compared to the permutation model as indicated by the gray points. Each gray point corresponds to the total number of divergent/convergent gene pairs observed in an iteration of the permutation model. The box plot depicts the quantiles of the total convergent/divergent transcript pair count based on the permutation model ($p < 1 \times 10^{-5}$). For definition of convergent/divergent gene pairs see Experimental Procedures. See also Figures S1, S3, S4.

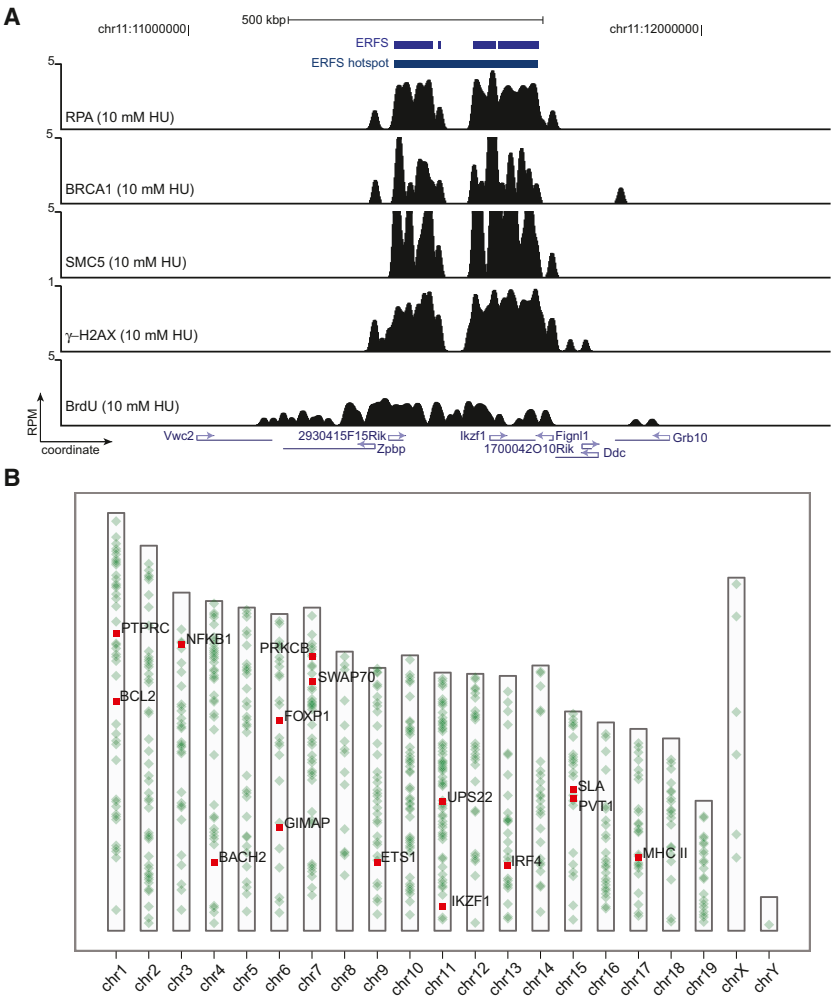

C

	ERFS Name	Chromosome	Length (Kb)	Gene Cluster	Transcribed	Convergent and/or Divergent Transcripts	Rearranged in B Cell Cancer	AID Target
1	MHCII	17	333	Yes	Yes	Yes	Yes	Yes
2	GIMAP	6	128	Yes	Yes	Yes	No	Yes
3	SWAP70	7	314.6	Yes	Yes	Yes	No	No
4	BACH2	4	419.4	No	Yes	Yes	Yes	No
5	IKZF1	11	281.4	Yes	Yes	Yes	Yes	Yes
6	FOXP1	6	431.8	No	Yes	No	Yes	No
7	PTPRC	1	1121.6	Yes	Yes	Yes	No	No
8	SLA	15	498.8	Yes	Yes	Yes	No	No
9	PVT1	15	669.8	No	Yes	Yes	Yes	Yes
10	ETS1	9	520	Yes	Yes	Yes	Yes	Yes
11	IRF4	13	283	Yes	Yes	Yes	Yes	Yes
12	BCL2	1	656.8	Yes	Yes	Yes	Yes	No
13	USP22	11	60.2	No	Yes	Yes	No	No
14	NFκB1	3	117	No	Yes	No	No	Yes
15	PRKCB	7	170.6	No	Yes	No	No	No

Figure 2. ERFS "Hot Spots" Associate with Highly Transcribed Gene Clusters

(A) Gene tracks represent, from the top, ERFS and ERFS hot spot demarcations; bindings of RPA, BRCA1, SMC5, γH2AX occupancy; and BrdU incorporation near the *IKZF1* locus. The y axis represents the total number of mapped reads per million of mapped reads (RPM) in 200 nucleotide windows (sliding-window smoothed).

(B) Genome-wide map of 619 ERFS hot spots. Each hot spot is represented by a green dot on the ideograms. The top fifteen hot spots are color-coded in red.

(C) Table of the top 15 ERFS hot spots. ERFS hot spots are ordered based on a ranked statistics of RPA/SMC5/BRCA1-binding strength (see Experimental Procedures). The first column depicts a representative gene within the hot spot. A hot spot containing at least three genes is designated as a "gene-cluster." A hot spot with a gene transcript value greater than 1 RPKM (reads per kilobase exon model per million mapped reads) is designated as transcribed. ERFS rearrangements in B cell cancers are listed in Table S2. ERFS is designated as "AID-target" according to (Chiarle et al., 2011; Klein et al., 2011). For complete definition of columns see Experimental Procedures. See also Tables S1 and S2.

Replication is organized into discrete zones (30–450 kbp in size) containing multiple replication origins that exhibit similar replication timing (Costa and Blow, 2007). Similarly, approximately 80% of the ERFSs are within 300 kbp of one another (Figures 2A and S4G). We therefore integrated these neighboring clustered ERFSs and removed those with footprints less than 10 kbp to define 619 triple colocalized hot spot regions (Figure 2B; Table S1). Interestingly, whereas these hot spots were distributed throughout the genome, the density of hot spots on autosomes was higher than on the sex chromosomes, which have a lower gene density (Figure 2B). An examination of the top 15 hot spots based on a ranked statistics of RPA/BRCA1/SMC5-binding strength showed that 9 out of the 15 regions contained gene clusters with at least three genes, and 12 out of 15 exhibited divergent/convergent gene pairs (Figures 2A and 2C; Table S1). Of note, 8 out of 15 hot spots are also rearranged in B cell lymphomas (Figure 2C; Table S2), suggesting a possible link among ERFSs, genome rearrangements, and cancer (see below).

Early S Phase Arrest by HU Induces DNA Damage at ERFSs, but Not at CFSs

DNA damage at CFSs is visualized by conventional cytogenetic analysis of metaphase chromosomes (Durkin and Glover, 2007). To investigate whether the ERFSs defined by RPA/ BRCA1/SMC5 binding are prone to actual breakage, we again treated cells with 10 mM HU, released them into fresh medium overnight, and examined metaphase spreads. Chromatid breaks, chromosome breaks, and rearrangements could be discerned in 20%–60% of WT cells after HU treatment (Figure S2D). To determine whether ERFSs are more sensitive to breakage under replication stress than regions lacking RPA/BRCA1/SMC5 binding (i.e., cold spots), we hybridized metaphases with bacterial artificial

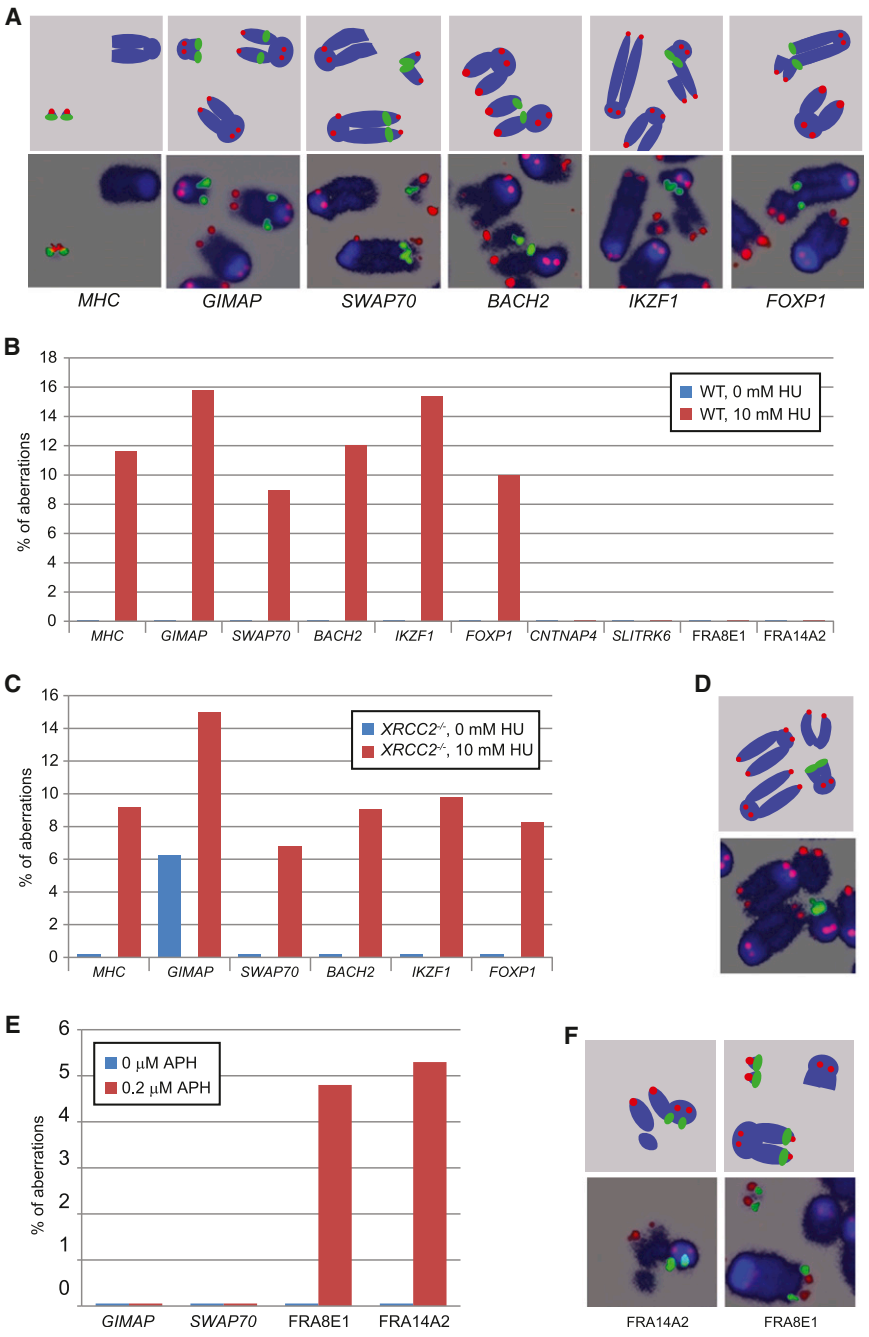

Figure 3. ERFS Break in Response to HU

(A) Upper: diagram of FISH probes. Lower: representative DNA aberrations identified by FISH. Blue is DAPI-stained DNA, green represents the BAC probe (*MHCII*, *GIMAP*, *SWAP70*, *BACH2*, *IKZF1*, or *FOXP1*) and red marks telomeric DNA.

(B) HU-induced aberrations were found at ERFSs but not at "cold sites" (*CNTNAP4*, *SLITRK6*) or CFSs (FRA8E1, FRA14A2). Quantitation of abnormalities from FISH analysis of untreated cells (blue bars) or cells treated with 10 mM HU (red bars). The percent aberrations specifically at the BAC probes relative to the total damage is plotted.

(C) Abnormalities detected by FISH in untreated (blue bars) and 10 mM HU-treated (red bars) *XRCC2*$^{-/-}$ cells.

(D) Upper: diagram of FISH probes. Lower: representative metaphase showing a spontaneous break at the *GIMAP* locus in an *XRCC2*$^{-/-}$ cell.

(E) Quantitation of abnormalities detected by FISH in untreated (blue bars) and 0.2 μM aphidicolin-treated (red bars) WT cells.

(F) Upper: diagram of FISH probes. Lower: representative metaphases showing aphidicolin-induced breaks at the FRA14A2 and FRA8E1 loci in WT cells. See also Figure S2 and Table S3.

chromosome (BAC) probes corresponding to six ERFS hot spots (*MHCII*, *GIMAP*, *SWAP70*, *BACH2*, *IKZF1*, and *FOXP1*) (Figures 3A and 3B), two cold spots (*CNTNAP4* and *SLITRK6*) and two CFSs (FRA8E1 and FRA14A2). For each of the six ERFS hot spots, a total of at least 40 chromosome aberrations were counted (Table S3). Notably, all six ERFS hot spots displayed chromosome aberrations in metaphases from HU-treated samples (Figure 3B). In contrast, neither of the cold regions or CFSs was broken under the same conditions (Figure 3B). Overall, 8%–15% of the total damage localized to individual ERFS hot spots, representing a significant fraction of the total damage (Figure 3B). DNA lesions were observed on either the centromeric or telomeric sides of ERFS-specific hybridized BAC (Figure S2E), suggesting that an ERFS represents a large fragile genomic region.

Aberrations at ERFS hot spots were also detected in *XRCC2*$^{-/-}$ cells treated with HU (Figure 3C). *XRCC2*$^{-/-}$ cells are more sensitive to HU than WT cells are, as evidenced by the higher level of total damage in these cells (Figure S2D). Breaks at *MHCII*, *GIMAP*, *SWAP70*, *BACH2*, *IKZF1*, and *FOXP1* were found in 5%–10% of HU-treated *XRCC2*$^{-/-}$ cells compared with 1%–6% of WT cells damaged in these regions (Table S3). Nevertheless, the frequency of ERFS-specific instability relative to the total damage was similar in *XRCC2*$^{-/-}$ and WT cells (Figures 3B and 3C). Interestingly, breaks in the vicinity of the *GIMAP* hot spot were detectable spontaneously in *XRCC2*$^{-/-}$ cells (Figures 3C and 3D; Table S3), which is consistent with increased γ-H2AX observed in unchallenged *XRCC2* mutant cells (Figure S2A).

None of the eight CFSs defined in mouse (Helmrich et al., 2006) were among our 619 ERFS hot spots (Table S1). Consistent with this, DNA aberrations at two of the most expressed CFSs in mouse lymphocytes, FRA14A2 and FRA8E1 (Helmrich et al., 2006) were undetectable in HU-treated WT samples

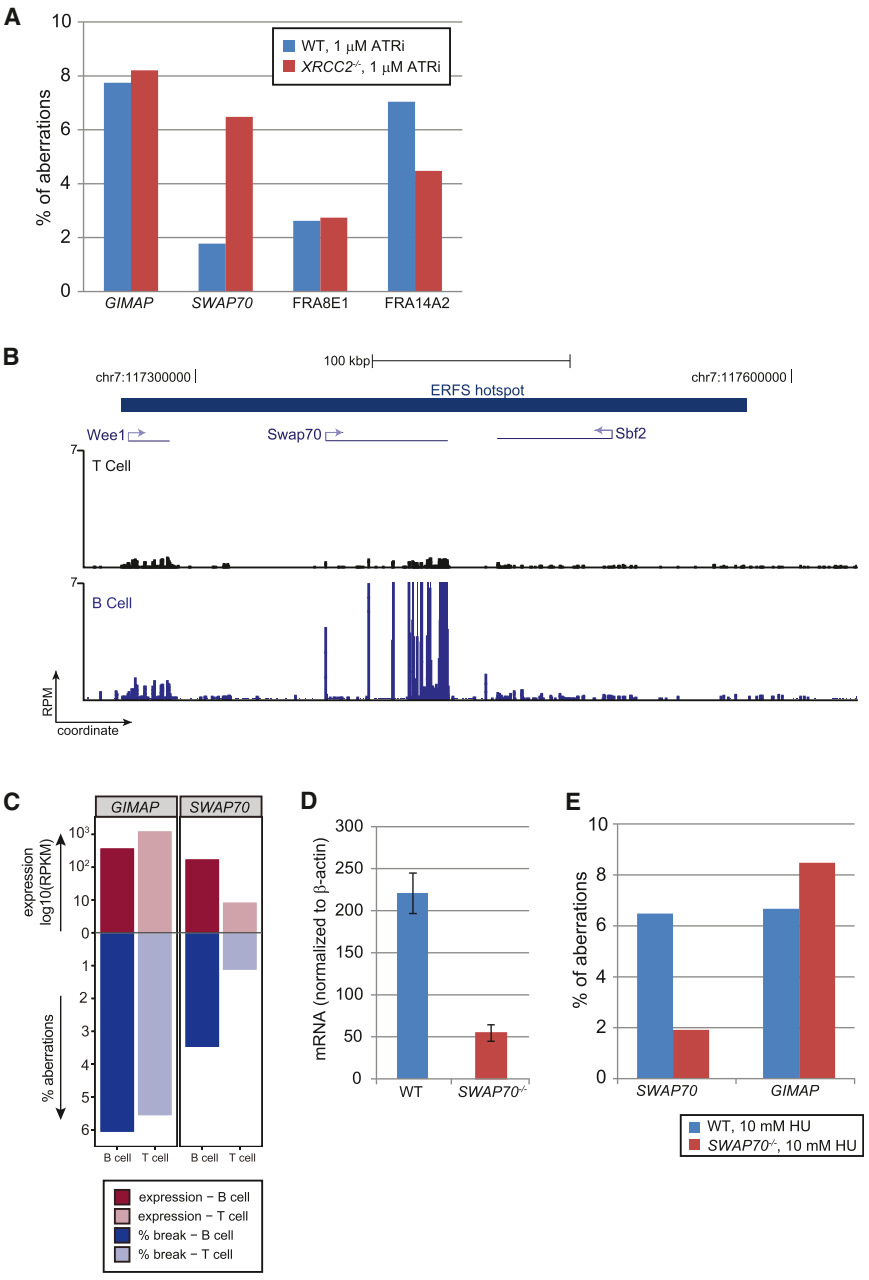

Figure 4. ERFS Break in Response to ATR Inhibition and High Transcription

(A) Quantitation of aberrations observed by FISH in response to overnight exposure to 1 μM ATRi in WT (blue bars) and *XRCC2*$^{-/-}$ cells (red bars).

(B) Gene tracks represent, from the top, ERFS demarcation and transcription measured by RNA-Seq in T and B cells at the region flanking *SWAP70* locus.

(C) Relative transcriptional activities of *GIMAP* and *SWAP70* loci in B and T cells and their relation to the ERFS fragility. *GIMAP* and SWAP70 hot spots are shown in separate facets. The x axis shows the cell lineage. The y axis upward depicts the log10(RPKM) in B and T cells by dark and light reds, respectively; the y axis downward depicts the quantitation of aberrations observed by FISH in response to overnight exposure to 1 μM ATRi in B and T cells in dark and light blue, respectively.

(D) Relative SWAP70 mRNA abundance (measured across exon 4) normalized to β-actin in WT and *SWAP70*$^{-/-}$ B cells (mean ± SD).

(E) Quantitation of aberrations in WT and *SWAP70*$^{-/-}$ cells at the *GIMAP* and *SWAP70* regions in response to 10 mM HU. See also Figure S5 and Table S3.

ATR Inhibition Promotes ERFS and CFS Expression

The ATR kinase protects the genome from chromosomal aberrations at late replicating CFSs, (Durkin and Glover, 2007) and is essential for stabilizing stalled forks and facilitates fork restart in early S phase (Cimprich and Cortez, 2008). To confirm that ATR inactivation induces CFSs and determine whether it similarly leads to damage at ERFSs, we treated asynchronous B cells on day 2 with 1 μM of a recently described ATR inhibitor (ATRi) (Toledo et al., 2011). We found that approximately 2.5% and 7.0% of the total chromosomal aberrations localized to the two CFSs, FRA8E1 and FRA14A2, respectively (Figure 4A). ATR deficiency also led to chromosomal aberrations at ERFSs at a similar frequency (Figure 4A; Table S3). Moreover, ERFSs and CFSs were both damaged in *XRCC2*$^{-/-}$ cells treated with ATRi (Figure 4A). Thus, the rupture of unreplicated regions at CFSs and fork collapse at ERFSs are similarly sensitive to ATR inhibition.

(Figure 3B). Absence of CFS expression could be explained by the fact that high concentrations of HU stall replication forks in early S phase (Figure 1A), whereas CFSs replicate late (Durkin and Glover, 2007). Conversely, we found that overnight treatment with low doses of aphidicolin (0.2 μM for 20 hr) induced damage at the CFSs FRA14A2 and FRA8E1, whereas the ERFSs *GIMAP* and *SWAP70* were largely insensitive (Figures 3E and 3F). These data are consistent with the idea that ERFS arise from fork collapse during early replication, whereas breakage at CFSs arises from a failure to replicate (Debatisse et al., 2012), and the two forms of replication stress induce distinct types of recurrent DNA lesions.

Transcriptional Activity Can Increase ERFS Fragility

As described above, ERFSs are enriched in regions with high transcriptional activity (Figures 1H, 2C, and S4F; Table S1). To determine the contribution of transcriptional activity to individual ERFSs, we focused on loci with tissue-specific transcription patterns. SWAP70 is a B-cell-specific developmental regulator, whereas genes within the *GIMAP* cluster are expressed both in

B and in T cells (Figures 4B and S5A). Treatment with ATRi led to a similar frequency of damage at *GIMAP* in B and T cells, consistent with insignificant changes in gene expression between the two cell types (Figure 4C). In contrast, damage near *SWAP70* was 3-fold lower in T than in B cells (Figure 4C; Table S3), which correlated with the decreased transcription of *SWAP70* in T cells (Figure 4B). Nevertheless, the replication timing near *SWAP70* was similar in both cell types (Figure S5B). To further delineate the role of transcription on ERFS breakage, we used *SWAP70*$^{-/-}$ mice in which 2.7 kbp, including the first exon and part of the 5′ untranslated region, is removed (Borggrefe et al., 2001), allowing us to compare the fragility of ERFSs in the same genomic region in knockout B cells. We determined that *SWAP70* mRNA in *SWAP70*$^{-/-}$ B cells was reduced by approximately 4-fold relative to levels in WT (Figure 4D). Moreover, DNA damage near *SWAP70* was approximately 2.5-fold lower in *SWAP70*$^{-/-}$ relative to levels in WT B cells (Figure 4E). In contrast, DNA damage near *GIMAP* remained at a similar level both in WT and *SWAP70*$^{-/-}$ cells (Figure 4E). Although our data indicate that high level of transcription contributes to the breakage of some ERFSs, other molecular features, including repetitive elements (Figure 1F), covalently bound protein complexes, and RNA:DNA hybrids, might also be sources of ERFS fragility.

Oncogenic Stress Can Trigger ERFS and CFS Fragility

Oncogene deregulation is thought to compromise genome integrity preferentially at CFSs (Bartek et al., 2007; Halazonetis et al., 2008), and CFS deletion has been associated with various cancers (Bignell et al., 2010). To determine whether oncogenic stress similarly induces DNA damage at ERFSs, we overexpressed *c-myc* in B cells because it has been implicated in regulating replication initiation and origin firing (Dominguez-Sola et al., 2007). *XRCC2*$^{-/-}$ cells were utilized to increase the amount of replicative stress and DNA damage as a result of decreased HR (Figure S2D). *c-myc* overexpression led to induction of p53 (Figure 5A), which correlated with an approximately 1.6-fold increase in overall DNA damage in *XRCC2*$^{-/-}$ cells overexpressing *c-myc* compared to empty vector (EV)-infected cells (Table S3). Moreover, 7.3% of the total breaks generated in *c-myc* overexpressing cells were found near *SWAP70*, compared to 2.4% of total breaks at this ERFS in EV-infected B cells (Figure 5B). Similarly, out of 43 breaks observed in *c-myc*-infected cells, 3 (7%) were found at the *GIMAP* cluster, and 3 (6.7%) were found near BACH2. *c-myc* overexpression also induced breaks at FRA8E1, showing a 2-fold relative increase in breaks relative to EV-infected cells (Figure 5B). Thus, DNA damage induced by *c-myc* overexpression can occur at ERFSs and CFSs.

ERFS Fragility Is AID Independent

Mutations and DSBs at various oncogenes, including *c-myc*, are due to AID off-target activity (Robbiani et al., 2008). Recently, a number of genome-wide studies in primary B cells mapped AID-induced DNA translocation events, and identified several novel hot spots for AID-dependent translocations at non-Ig genes (Chiarle et al., 2011; Kato et al., 2012; Klein et al., 2011). Among these translocation hot spots, *MHCII*, *GIMAP*, *IKZF1*, *PVT1*, *ETS1*, *IRF4*, and *NFkB1* were located within the top 15 ERFS hot spots in this study, whereas the *IgH* locus (the physiologic target of AID) was not ranked high on the list (Figure 2C; Table S1). To determine whether AID contributes to ERFS fragility, we stimulated WT and AID knockout B cells with LPS/IL4 for 2 days, and then treated them with ATRi overnight. These conditions induce robust AID-dependent DNA damage simultaneously with replication stress. We probed metaphases with BACs spanning the *IgH* locus, the *GIMAP* cluster, and *IKZF1*-all AID translocation hot spots—as well as *BACH2*, *SWAP70*, *FOXP1*, and *BCL2* (Figure S2E)—ERFSs that are frequently rearranged in B cell lymphoma (Figure 2C; Tables S1 and S2). In WT, the IgH locus was damaged in 3.8% of cells, but the frequency of *IgH*-specific instability did not increase with ATRi (Figure S2F), despite the fact that ATRi greatly increased overall damage (Table S3). Upon ATRi treatment, the frequency of breaks at the ERFSs *GIMAP*, *IKZF1*, *BACH2*, *SWAP70*, and *FOXP1*, and *BCL2* were elevated to the levels similar to those observed at the *IgH* in activated B cells (Figure S2F). Breaks at some ERFSs were even spontaneously detected (*FOXP1* and *GIMAP*, Figure S2F).

To determine whether AID expression contributes to aberrations observed at ERFSs, we next analyzed their breakage frequency in *AID*$^{-/-}$ cells. Unlike WT cells, *IgH* breaks were absent in *AID*$^{-/-}$ cells. In contrast, all ERFSs exhibited similar levels of breakage both in WT and *AID*$^{-/-}$ cells (Figure 5C; Table S3). Therefore, whereas *IgH* breaks in B cells are entirely AID dependent, the breakage of ERFSs is AID independent. Altogether, these data suggest that some recurrent rearrangements in B cell lymphoma are due to AID-independent replicative stress at ERFSs.

Genome Instability at ERFSs Is Observed in Mouse Models and Human Cancer

Among the top 15 ERFS hot spot that break in response to AID-independent replication stress, we have identified three partners that recurrently translocate to *IgH* in lymphomas: *BACH2*, *FOXP*1, and *BCL2* (Table S2). We hypothesized that if AID-dependent DSBs in G1 persisted into early S phase, translocations between AID-dependent breaks and ERFS might be detectable. To test this, we examined cells transgenically overexpressing AID and simultaneously deficient for 53BP1 (IgκAID/*53BP1*$^{-/-}$), thus allowing the persistence of G1 *IgH* breaks into S phase where they could be joined to ERFSs. Indeed, 26% and 7% of IgκAID/*53BP1*$^{-/-}$ B cells carried *IgH* locus and *BACH2* breaks, respectively (Figure 5D). These breaks are fusogenic because *IgH*- and *BACH2*-associated translocations to unidentified partner chromosomes were found in 7.3% and 1.2% of the metaphases, respectively (Figure 5D). Importantly, we also detected one *IgH*/*BACH2* translocation among 750 cells (Figure 5E), reminiscent of the IgH/BACH2 translocations observed in human B cell lymphoma (Kobayashi et al., 2011). Thus, AID-dependent breaks generated in G1 (Petersen et al., 2001) can join to ERFS breaks triggered in early S phase.

A hallmark of cancer genomes is widespread copy-number changes, insertions, and deletions. To determine whether deletions and/or amplifications at ERFSs are a general feature of the B cell lymphoma genome, we compared our ERFSs with

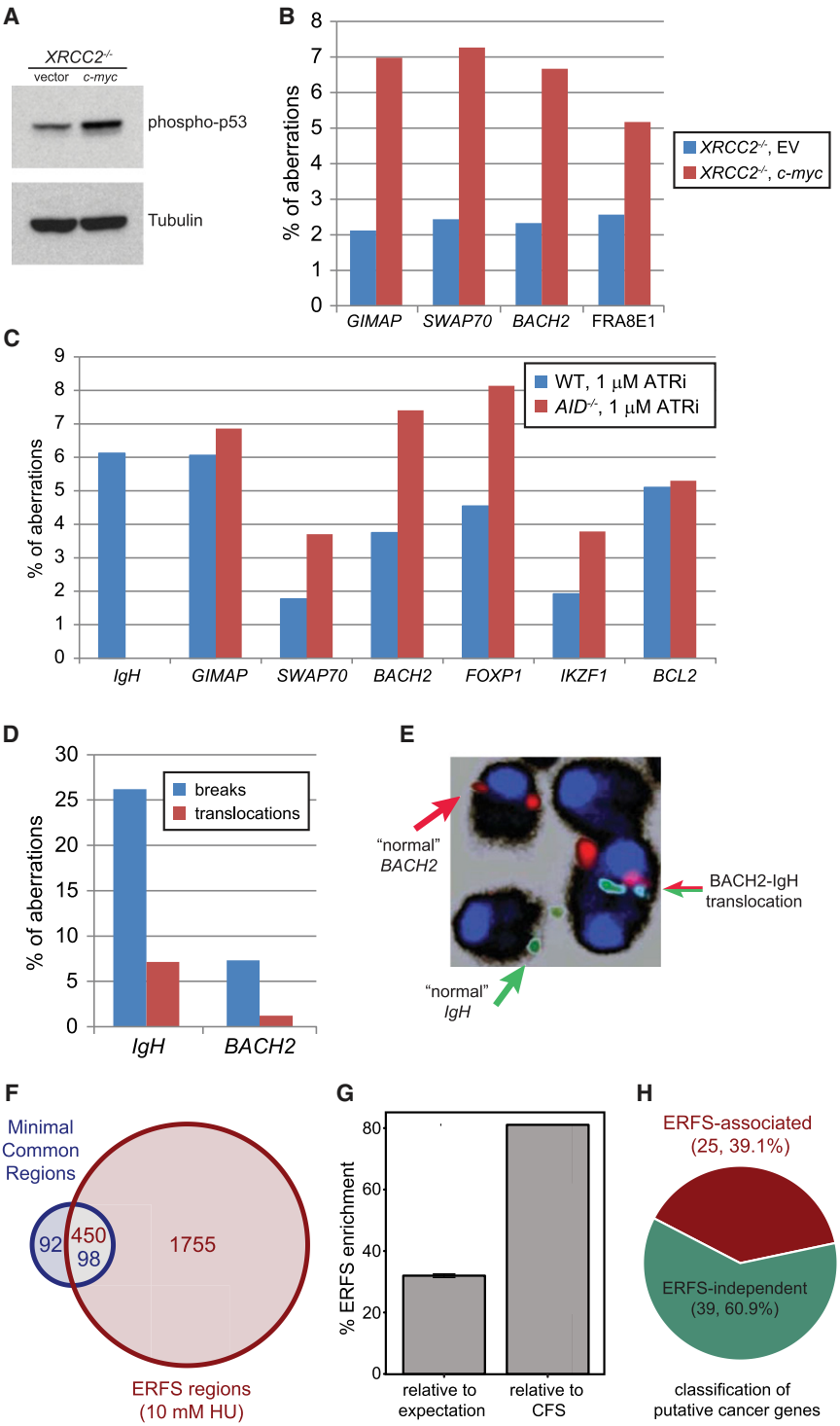

Figure 5. ERFS Fragility Is Observed in Response to Oncogenic Stress and in Human Cancer

(A) Western blot for phosphorylated p53 in *c-myc* and EV-infected *XRCC2*$^{-/-}$ B cells.

(B) Aberrations in *c-myc*-infected and EV-infected *XRCC2*$^{-/-}$ B cells.

(C) Aberrations in WT (blue bars) and *AID*$^{-/-}$ B cells (red bars) treated with 1 μM ATRi.

(D) Spontaneous chromosome breaks (blue bars) and translocations (red bars) at the *IgH* and *BACH2* locus in IgκAID/*53BP1*$^{-/-}$ B cells.

(E) Normal chromosomes and a translocation of *BACH2* ERFS (red) to the *IgH* locus (green) is shown.

(F and G) ERFSs significantly overlap with MCRs detected in DLBCL. The Venn diagram shows the overlap of ERFSs with MCR found in DLBCL. The total number of regions is indicated for each shared and unique area and color-coded based on the region's title.

(G) Significance of correlation between the ERFSs and MCRs is evaluated relative to the permutation model and CFSs. The percent increase in the overlap between the ERFSs and MCRs relative to the permutation model's expectation (mean ± SEM, $p < 1 \times 10^{-4}$) and CFSs are shown in the left and right bar graphs, respectively.

(H) ERFSs are enriched for known cancer genes. The pie chart shows the fraction of putative cancer genes (Bignell et al., 2010) associated with ERFSs ($p < 6 \times 10^{-20}$). See also Figure S6 and Tables S3 and S4.

high resolution copy-number changes detected in biopsies of patients with diffuse large B cell lymphoma (DLBCL), the most common type of non-Hodgkins lymphoma (Lenz et al., 2008). A total of 190 "minimal common regions" (MCRs) were found among 203 biopsies, carrying a gain or a loss of a chromosomal region ranging in size from 5 kbp to 21Mbp (Lenz et al., 2008). Mouse ERFS coordinates were overlaid onto the human genome using two methods, yielding 2,205 syntenic regions (Figures S6B–S6D). Notably, 51.6% of the MCRs observed in primary DLBCL overlapped with syntenic ERFS regions (p(permutation) $< 1 \times 10^{-4}$, Figure 5F). Moreover, 20.4% of ERFSs overlapped with MCRs, 32% higher than expectation (p(permutation) $< 1 \times 10^{-6}$, Figure 5G). Surprisingly, ERFS were deleted or amplified in DLBCL at least 81% more frequently as compared to CFSs, despite their cancer-specific propensity for breakage (Figure 5G). Moreover, our analysis indicated that the DLBCL copy-number alterations exhibited 2-fold higher correlation with B cell ERFSs compared to deletions and/or amplifications in T lineage acute lymphoblastic leukemia (Figure S6A) (Zhang et al., 2012a). Finally, by examining homozygous deletions in cancer genomes (Bignell et al., 2010), we found that 25 out of 64 genes known to contribute to oncogenesis coincide with ERFSs (p(hypergeometric) $< 6 \times 10^{-20}$, Figure 5H; Table S4). Based on these findings,

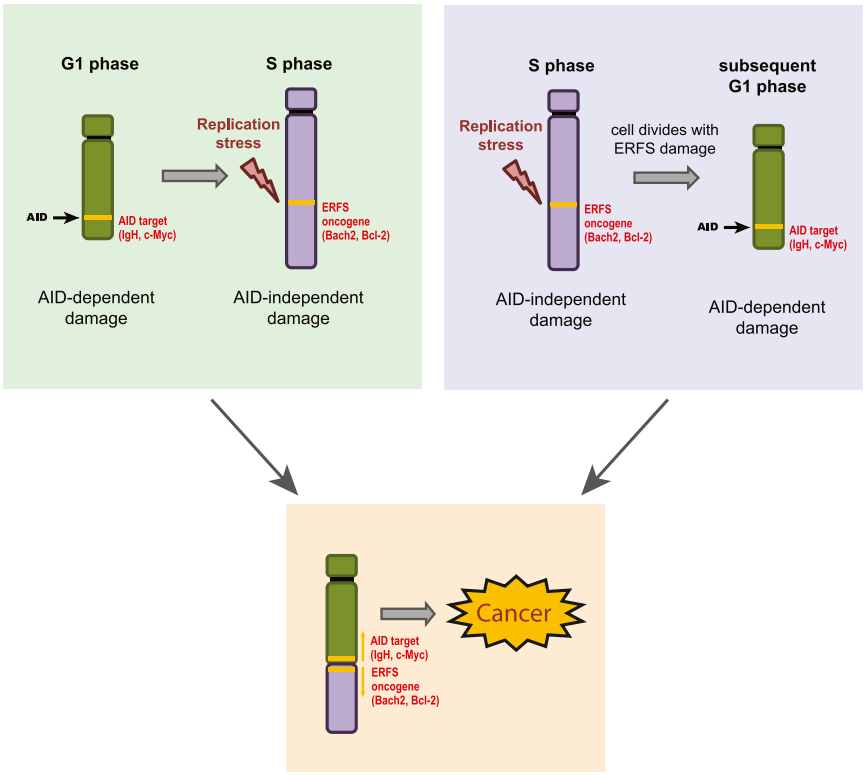

Figure 6. Model for Recurrent Rearrangements in B Cell Lymphomas

AID is active in G1 (Petersen et al., 2001) and targets IgH and various oncogenes (e.g., *c-myc*). Replication fork collapse at ERFSs in S phase occurs at preferential sites including various cancer-associated genes (e.g., *BCL2*, *BACH2*). An AID-generated break might be passed from G1 to early S, where it meets an ERFS, which may eventually result in a translocation (left). Alternatively, an ERFS (bearing unresolved a replication intermediate of under-replicated DNA) might break in mitosis and then become permissive to translocate to an AID-induced DSB in the next G1 phase of the cell cycle (right).

we conclude that ERFSs are a significant feature of the mutational landscape of diffuse large B cell lymphomas and potentially other cancers.

DISCUSSION

Replicative Stress at ERFSs Contributes to Genome Instability in B Cells

Although AID has been implicated in B cell translocations (Gostissa et al., 2011), very little is known about the mechanisms of chromosomal breakage at several *IgH*-partner loci, including *BCL2*, *BACH2*, and *FOXP1*. Besides programmed DNA damage, replication-based mechanisms are a major contributor to chromosomal instability in cancer (Liu et al., 2012). Activated B cells are among the most rapidly dividing mammalian cells (Zhang et al., 1988), which potentially exposes them to high endogenous levels of replicative stress. Here, we have used a genome-wide approach to identify a subset of early replicating regions in the B cell genome that are particularly vulnerable to fork collapse and contribute to rearrangements in B cell malignancies. In our model, ERFS breaks can occur after the generation of unrepaired AID-induced breaks in G1, and the two breaks could recombine during S or G2. Alternatively, ERFS damage might persist through mitosis resulting in DNA breaks in the subsequent G1 phase when AID is predominantly active. In either case, we suggest that AID-mediated DSBs in G1 (Petersen et al., 2001), together with replication-stress-induced damage at recurrent loci, can coordinately drive B cell lymphoma initiation and progression (Figure 6).

ERFS versus CFS

CFSs are considered to be the most replication-stress-sensitive sites in the genome (Durkin and Glover, 2007). Although no single mechanism accounts for CFS instability, it is hypothesized that a number of different characteristics may contribute to their fragility including co-occurrence with very large genes, late replication, low density of replication origins, high A-T content, and sequences prone to form secondary structures, histone hypoacetylation, and a condensed chromatin structure (Helmrich et al., 2011; Jiang et al., 2009; Letessier et al., 2011; Ozeri-Galai et al., 2011). In stark contrast to CFSs, our identified ERFSs replicate early; have an open chromatin configuration; and are origin-, gene-, and G-C-rich.

Despite these diametrically opposite properties, both CFS and ERFS fragility are increased by ATR inhibition (Figure 4A), oncogenic stress (Figure 5B), and deficiencies in HR (Figure 3C) (Bartek et al., 2007; Durkin and Glover, 2007; Halazonetis et al., 2008). These conditions decrease the rate of fork progression but concomitantly increase the density of replication initiating events (Bester et al., 2011; Daboussi et al., 2008; Dominguez-Sola et al., 2007; Shechter et al., 2004), which might contribute to the damage at both CFSs and ERFSs, respectively. The decrease in fork speed hinders the completion of replication at CFSs, either because of the scarcity of origins near CFSs (Letessier et al., 2011), the heterochromatic nature of the regions that would limit accessibility of DNA replication and/or DSB repair machineries (Jiang et al., 2009), or because of the interference between transcription and replication at very large genes (Helmrich et al., 2011). Although additional origins are not activated near CFSs upon replication stress (Letessier et al., 2011), an increase in origin activity at early replicons might paradoxically contribute to genome instability at ERFSs. For example, increasing the replication initiation events near highly transcribed gene clusters with divergent and/or convergent gene pairs could increase conflicts between DNA replication and transcription machineries. The higher density of activated origins at ERFSs would also be expected to prematurely deplete

nucleotide pools (Bester et al., 2011), thereby increasing the probability of subsequent fork stalling and collapse. These two outcomes of replication stress are likely to be linked because increased replication initiation and depletion of nucleotide supplies slows replication (Bester et al., 2011; Jones et al., 2012), whereas slow fork progression causes activation of dormant origins (Ge et al., 2007), and both incomplete replication and increased origin firing are monitored by ATR activity (Shechter et al., 2004). In conclusion, increased initiating events at ERFSs and a paucity of replication initiation at CFSs could both challenge replication fidelity.

ERFSs and Cancer

Oncogenic stress is a major driving force in the early stages of cancer development (Halazonetis et al., 2008); nevertheless, the factors that trigger replicative stress in vivo remain unclear. In the case of B cell lymphomas, oncogenic stress can be initiated by the activity of AID, which by targeting non-*Ig* genes such as *c-myc* (Robbiani et al., 2008), leads to *c-myc*/*IgH* translocations and consequent aberrant *c-myc* expression. This form of AID-induced oncogenic stress or high levels of proliferative activity in activated B cells could generate DNA damage at ERFSs (Figure 6).

Altogether, 103 AID hot spots (Chiarle et al., 2011; Klein et al., 2011)—including the *GIMAP* cluster, *MHCII* locus, and *IKZF1*—were also identified as ERFS hot spots in this study (Table S1). It is possible that the overlap observed between a subset of off-target AID sites and ERFSs is due to common underlying features of these loci. For example, AID is recruited to ssDNA regions (Chaudhuri and Alt, 2004), which are also generated during replicative stress; AID-dependent DSBs and ERFSs are also both enriched in repeat elements (Staszewski et al., 2011). In addition, chromosomal regions with the highest transcriptional activity have the highest AID-dependent translocation density (Chiarle et al., 2011; Klein et al., 2011), and early origins and translocations frequently reside near transcription start sites and RNA polymerase-II-binding sites (Chiarle et al., 2011; Klein et al., 2011). Thus, these euchromatic regions could serve both as AID targets in G1 and also be susceptible to fork collapse during early S phase.

A number of different hypotheses have been put forward about the mechanisms that promote recurrent translocations in mature B cell lymphomas. These include recurrent genomic damage by AID, random DNA damage followed by selection, and a nonrandom 3D organization of the genome (Chiarle et al., 2011; Hakim et al., 2012; Klein et al., 2011; Zhang et al., 2012b). To date, replication-stress-induced DNA damage has been associated with late-replicating CFS. By using an alternative experimental approach for the discovery of fragile site expression during early replication, we have identified a novel source of recurrent AID-independent DNA breaks that may play a mechanistic role in some of the most common genome rearrangements during B cell lymphomagenesis. Because transcriptional activity and replication timing of a genomic region vary among different cell lineages (Hansen et al., 2010), different sets of ERFSs might also account for recurrent chromosomal rearrangements in cancers of distinct cellular origins.

EXPERIMENTAL PROCEDURES

Mice

XRCC2$^{-/-}$(Frappart et al., 2009), 53BP1$^{-/-}$ (Ward et al., 2004), IgκAID (Robbiani et al., 2009), *AID*$^{-/-}$ (Muramatsu et al., 2000), and *SWAP70*$^{-/-}$ (Borggrefe et al., 2001) mice have been described. *SWAP70*$^{-/-}$ and WT control mice used in Figure 4D are C57BL/6 background; all other mice are 129/Sv x C57BL/6 background.

ChIP-Seq, Repli-Seq, RNA-Seq, DHS I Mapping, and FISH Analysis

ChIP-seq and RNA-Seq procedures were performed as in Yamane et al. (2011), Repli-Seq was performed as described in Hansen et al. (2010). DHSI mapping was performed as described (Sekimata et al., 2009), and fluorescence in situ hybridization (FISH) analysis is described in Callén et al. (2007). For detailed methods, see Extended Experimental Procedures.

BACs

Individual BACs to ERFSs were identified using NCBI clone finder and purchased from BACPAC. For complete list of BAC probes used in FISH experiments see Extended Experimental Procedures.

Retroviral Infection

Cells were infected with pMX-c-Myc-IRES-GFP or empty vector and GFP-positive cells were sorted as described (Robbiani et al., 2008).

Statistical and Computational Analyses

Detailed description is available in Extended Experimental Procedures.

ACCESSION NUMBERS

The ChIP-seq and RNA-seq data are deposited in GEO under accession number GSE43504.

SUPPLEMENTAL INFORMATION

Supplemental Information includes Extended Experimental Procedures, six figures, and four tables and can be found with this article online at http://dx.doi.org/10.1016/j.cell.2013.01.006.

ACKNOWLEDGMENTS

We thank Rolf Jessberger and Alessandra Pernis for *SWAP70*$^{-/-}$ mice, Mila Jankovic for pMX-c-Myc-IRES-GFP, Jean Gautier, Mirit Aladjem, and Toren Finkel for discussions and Lars Grontved for help with DHS mapping. This work was supported by the Intramural Research Program of the NIH, the National Cancer Institute, and the Center for Cancer Research, and by a Department of Defense grant to A.N. (BC102335). This study utilized the high-performance computational capabilities of the Biowulf Linux cluster at the NIH.

Received: November 9, 2012
Revised: December 10, 2012
Accepted: January 2, 2013
Published: January 24, 2013

REFERENCES

Bartek, J., Bartkova, J., and Lukas, J. (2007). DNA damage signalling guards against activated oncogenes and tumour progression. Oncogene *26*, 7773–7779.

Bester, A.C., Roniger, M., Oren, Y.S., Im, M.M., Sarni, D., Chaoat, M., Bensimon, A., Zamir, G., Shewach, D.S., and Kerem, B. (2011). Nucleotide deficiency promotes genomic instability in early stages of cancer development. Cell *145*, 435–446.

Bignell, G.R., Greenman, C.D., Davies, H., Butler, A.P., Edkins, S., Andrews, J.M., Buck, G., Chen, L., Beare, D., Latimer, C., et al. (2010). Signatures of mutation and selection in the cancer genome. Nature *463*, 893–898.

Borggrefe, T., Keshavarzi, S., Gross, B., Wabl, M., and Jessberger, R. (2001). Impaired IgE response in SWAP-70-deficient mice. Eur. J. Immunol. *31*, 2467–2475.

Bothmer, A., Robbiani, D.F., Feldhahn, N., Gazumyan, A., Nussenzweig, A., and Nussenzweig, M.C. (2010). 53BP1 regulates DNA resection and the choice between classical and alternative end joining during class switch recombination. J. Exp. Med. *207*, 855–865.

Bunting, S.F., Callén, E., Kozak, M.L., Kim, J.M., Wong, N., López-Contreras, A.J., Ludwig, T., Baer, R., Faryabi, R.B., Malhowski, A., et al. (2012). Mol. Cell *46*, 125–135.

Bunting, S.F., Callén, E., Wong, N., Chen, H.T., Polato, F., Gunn, A., Bothmer, A., Feldhahn, N., Fernandez-Capetillo, O., Cao, L., et al. (2010). 53BP1 inhibits homologous recombination in Brca1-deficient cells by blocking resection of DNA breaks. Cell *141*, 243–254.

Callén, E., Jankovic, M., Difilippantonio, S., Daniel, J.A., Chen, H.T., Celeste, A., Pellegrini, M., McBride, K., Wangsa, D., Bredemeyer, A.L., et al. (2007). ATM prevents the persistence and propagation of chromosome breaks in lymphocytes. Cell *130*, 63–75.

Cha, R.S., and Kleckner, N. (2002). ATR homolog Mec1 promotes fork progression, thus averting breaks in replication slow zones. Science *297*, 602–606.

Chaudhuri, J., and Alt, F.W. (2004). Class-switch recombination: interplay of transcription, DNA deamination and DNA repair. Nat. Rev. Immunol. *4*, 541–552.

Chen, H.T., Bhandoola, A., Difilippantonio, M.J., Zhu, J., Brown, M.J., Tai, X., Rogakou, E.P., Brotz, T.M., Bonner, W.M., Ried, T., and Nussenzweig, A. (2000). Response to RAG-mediated VDJ cleavage by NBS1 and gamma-H2AX. Science *290*, 1962–1965.

Chiarle, R., Zhang, Y., Frock, R.L., Lewis, S.M., Molinie, B., Ho, Y.J., Myers, D.R., Choi, V.W., Compagno, M., Malkin, D.J., et al. (2011). Genome-wide translocation sequencing reveals mechanisms of chromosome breaks and rearrangements in B cells. Cell *147*, 107–119.

Cimprich, K.A., and Cortez, D. (2008). ATR: an essential regulator of genome integrity. Nat. Rev. Mol. Cell Biol. *9*, 616–627.

Costa, S., and Blow, J.J. (2007). The elusive determinants of replication origins. EMBO Rep. *8*, 332–334.

Daboussi, F., Courbet, S., Benhamou, S., Kannouche, P., Zdzienicka, M.Z., Debatisse, M., and Lopez, B.S. (2008). A homologous recombination defect affects replication-fork progression in mammalian cells. J. Cell Sci. *121*, 162–166.

Debatisse, M., Le Tallec, B., Letessier, A., Dutrillaux, B., and Brison, O. (2012). Common fragile sites: mechanisms of instability revisited. Trends Genet. *28*, 22–32.

Dominguez-Sola, D., Ying, C.Y., Grandori, C., Ruggiero, L., Chen, B., Li, M., Galloway, D.A., Gu, W., Gautier, J., and Dalla-Favera, R. (2007). Non-transcriptional control of DNA replication by c-Myc. Nature *448*, 445–451.

Durkin, S.G., and Glover, T.W. (2007). Chromosome fragile sites. Annu. Rev. Genet. *41*, 169–192.

Feng, W., Collingwood, D., Boeck, M.E., Fox, L.A., Alvino, G.M., Fangman, W.L., Raghuraman, M.K., and Brewer, B.J. (2006). Genomic mapping of single-stranded DNA in hydroxyurea-challenged yeasts identifies origins of replication. Nat. Cell Biol. *8*, 148–155.

Frappart, P.O., Lee, Y., Russell, H.R., Chalhoub, N., Wang, Y.D., Orii, K.E., Zhao, J., Kondo, N., Baker, S.J., and McKinnon, P.J. (2009). Recurrent genomic alterations characterize medulloblastoma arising from DNA double-strand break repair deficiency. Proc. Natl. Acad. Sci. USA *106*, 1880–1885.

Ge, X.Q., Jackson, D.A., and Blow, J.J. (2007). Dormant origins licensed by excess Mcm2-7 are required for human cells to survive replicative stress. Genes Dev. *21*, 3331–3341.

Gostissa, M., Alt, F.W., and Chiarle, R. (2011). Mechanisms that promote and suppress chromosomal translocations in lymphocytes. Annu. Rev. Immunol. *29*, 319–350.

Hakim, O., Resch, W., Yamane, A., Klein, I., Kieffer-Kwon, K.R., Jankovic, M., Oliveira, T., Bothmer, A., Voss, T.C., Ansarah-Sobrinho, C., et al. (2012). DNA damage defines sites of recurrent chromosomal translocations in B lymphocytes. Nature *484*, 69–74.

Halazonetis, T.D., Gorgoulis, V.G., and Bartek, J. (2008). An oncogene-induced DNA damage model for cancer development. Science *319*, 1352–1355.

Hansen, R.S., Thomas, S., Sandstrom, R., Canfield, T.K., Thurman, R.E., Weaver, M., Dorschner, M.O., Gartler, S.M., and Stamatoyannopoulos, J.A. (2010). Sequencing newly replicated DNA reveals widespread plasticity in human replication timing. Proc. Natl. Acad. Sci. USA *107*, 139–144.

Hashash, N., Johnson, A.L., and Cha, R.S. (2011). Regulation of fragile sites expression in budding yeast by MEC1, RRM3 and hydroxyurea. J. Cell Sci. *124*, 181–185.

Helmrich, A., Stout-Weider, K., Hermann, K., Schrock, E., and Heiden, T. (2006). Common fragile sites are conserved features of human and mouse chromosomes and relate to large active genes. Genome Res. *16*, 1222–1230.

Helmrich, A., Ballarino, M., and Tora, L. (2011). Collisions between replication and transcription complexes cause common fragile site instability at the longest human genes. Mol. Cell *44*, 966–977.

Jiang, Y., Lucas, I., Young, D.J., Davis, E.M., Karrison, T., Rest, J.S., and Le Beau, M.M. (2009). Common fragile sites are characterized by histone hypoacetylation. Hum. Mol. Genet. *18*, 4501–4512.

Jones, R.M., Mortusewicz, O., Afzal, I., Lorvellec, M., García, P., Helleday, T., and Petermann, E. (2012). Increased replication initiation and conflicts with transcription underlie Cyclin E-induced replication stress. Oncogene. Published online September 3, 2012.

Kato, L., Begum, N.A., Burroughs, A.M., Doi, T., Kawai, J., Daub, C.O., Kawaguchi, T., Matsuda, F., Hayashizaki, Y., and Honjo, T. (2012). Nonimmunoglobulin target loci of activation-induced cytidine deaminase (AID) share unique features with immunoglobulin genes. Proc. Natl. Acad. Sci. USA *109*, 2479–2484.

Klein, I.A., Resch, W., Jankovic, M., Oliveira, T., Yamane, A., Nakahashi, H., Di Virgilio, M., Bothmer, A., Nussenzweig, A., Robbiani, D.F., et al. (2011). Translocation-capture sequencing reveals the extent and nature of chromosomal rearrangements in B lymphocytes. Cell *147*, 95–106.

Kobayashi, S., Taki, T., Chinen, Y., Tsutsumi, Y., Ohshiro, M., Kobayashi, T., Matsumoto, Y., Kuroda, J., Horiike, S., Nishida, K., and Taniwaki, M. (2011). Identification of IGHCδ-BACH2 fusion transcripts resulting from cryptic chromosomal rearrangements of 14q32 with 6q15 in aggressive B-cell lymphoma/leukemia. Genes Chromosomes Cancer *50*, 207–216.

Lenz, G., Wright, G.W., Emre, N.C., Kohlhammer, H., Dave, S.S., Davis, R.E., Carty, S., Lam, L.T., Shaffer, A.L., Xiao, W., et al. (2008). Molecular subtypes of diffuse large B-cell lymphoma arise by distinct genetic pathways. Proc. Natl. Acad. Sci. USA *105*, 13520–13525.

Letessier, A., Millot, G.A., Koundrioukoff, S., Lachagès, A.M., Vogt, N., Hansen, R.S., Malfoy, B., Brison, O., and Debatisse, M. (2011). Cell-type-specific replication initiation programs set fragility of the FRA3B fragile site. Nature *470*, 120–123.

Liu, M., Duke, J.L., Richter, D.J., Vinuesa, C.G., Goodnow, C.C., Kleinstein, S.H., and Schatz, D.G. (2008). Two levels of protection for the B cell genome during somatic hypermutation. Nature *451*, 841–845.

Liu, P., Carvalho, C.M., Hastings, P.J., and Lupski, J.R. (2012). Mechanisms for recurrent and complex human genomic rearrangements. Curr. Opin. Genet. Dev. *22*, 211–220.

MacAlpine, D.M., Rodríguez, H.K., and Bell, S.P. (2004). Coordination of replication and transcription along a Drosophila chromosome. Genes Dev. *18*, 3094–3105.

Mirkin, E.V., and Mirkin, S.M. (2007). Replication fork stalling at natural impediments. Microbiol. Mol. Biol. Rev. *71*, 13–35.

Muramatsu, M., Kinoshita, K., Fagarasan, S., Yamada, S., Shinkai, Y., and Honjo, T. (2000). Class switch recombination and hypermutation require activation-induced cytidine deaminase (AID), a potential RNA editing enzyme. Cell *102*, 553–563.

Ozeri-Galai, E., Lebofsky, R., Rahat, A., Bester, A.C., Bensimon, A., and Kerem, B. (2011). Failure of origin activation in response to fork stalling leads to chromosomal instability at fragile sites. Mol. Cell *43*, 122–131.

Petermann, E., Orta, M.L., Issaeva, N., Schultz, N., and Helleday, T. (2010). Hydroxyurea-stalled replication forks become progressively inactivated and require two different RAD51-mediated pathways for restart and repair. Mol. Cell *37*, 492–502.

Petersen, S., Casellas, R., Reina-San-Martin, B., Chen, H.T., Difilippantonio, M.J., Wilson, P.C., Hanitsch, L., Celeste, A., Muramatsu, M., Pilch, D.R., et al. (2001). AID is required to initiate Nbs1/gamma-H2AX focus formation and mutations at sites of class switching. Nature *414*, 660–665.

Raveendranathan, M., Chattopadhyay, S., Bolon, Y.T., Haworth, J., Clarke, D.J., and Bielinsky, A.K. (2006). Genome-wide replication profiles of S-phase checkpoint mutants reveal fragile sites in yeast. EMBO J. *25*, 3627–3639.

Robbiani, D.F., Bothmer, A., Callen, E., Reina-San-Martin, B., Dorsett, Y., Difilippantonio, S., Bolland, D.J., Chen, H.T., Corcoran, A.E., Nussenzweig, A., and Nussenzweig, M.C. (2008). AID is required for the chromosomal breaks in c-myc that lead to c-myc/IgH translocations. Cell *135*, 1028–1038.

Robbiani, D.F., Bunting, S., Feldhahn, N., Bothmer, A., Camps, J., Deroubaix, S., McBride, K.M., Klein, I.A., Stone, G., Eisenreich, T.R., et al. (2009). AID produces DNA double-strand breaks in non-Ig genes and mature B cell lymphomas with reciprocal chromosome translocations. Mol. Cell *36*, 631–641.

Schlacher, K., Wu, H., and Jasin, M. (2012). A distinct replication fork protection pathway connects Fanconi anemia tumor suppressors to RAD51-BRCA1/2. Cancer Cell *22*, 106–116.

Sekimata, M., Pérez-Melgosa, M., Miller, S.A., Weinmann, A.S., Sabo, P.J., Sandstrom, R., Dorschner, M.O., Stamatoyannopoulos, J.A., and Wilson, C.B. (2009). CCCTC-binding factor and the transcription factor T-bet orchestrate T helper 1 cell-specific structure and function at the interferon-gamma locus. Immunity *31*, 551–564.

Shechter, D., Costanzo, V., and Gautier, J. (2004). ATR and ATM regulate the timing of DNA replication origin firing. Nat. Cell Biol. *6*, 648–655.

Sonoda, E., Sasaki, M.S., Buerstedde, J.M., Bezzubova, O., Shinohara, A., Ogawa, H., Takata, M., Yamaguchi-Iwai, Y., and Takeda, S. (1998). Rad51-deficient vertebrate cells accumulate chromosomal breaks prior to cell death. EMBO J. *17*, 598–608.

Stamatoyannopoulos, J.A., Snyder, M., Hardison, R., Ren, B., Gingeras, T., Gilbert, D.M., Groudine, M., Bender, M., Kaul, R., Canfield, T., et al.; Mouse ENCODE Consortium. (2012). An encyclopedia of mouse DNA elements (Mouse ENCODE). Genome Biol. *13*, 418.

Staszewski, O., Baker, R.E., Ucher, A.J., Martier, R., Stavnezer, J., and Guikema, J.E. (2011). Activation-induced cytidine deaminase induces reproducible DNA breaks at many non-Ig Loci in activated B cells. Mol. Cell *41*, 232–242.

Stephan, A.K., Kliszczak, M., and Morrison, C.G. (2011). The Nse2/Mms21 SUMO ligase of the Smc5/6 complex in the maintenance of genome stability. FEBS Lett. *585*, 2907–2913.

Tanaka, T., and Nasmyth, K. (1998). Association of RPA with chromosomal replication origins requires an Mcm protein, and is regulated by Rad53, and cyclin- and Dbf4-dependent kinases. EMBO J. *17*, 5182–5191.

Toledo, L.I., Murga, M., Zur, R., Soria, R., Rodriguez, A., Martinez, S., Oyarzabal, J., Pastor, J., Bischoff, J.R., and Fernandez-Capetillo, O. (2011). A cell-based screen identifies ATR inhibitors with synthetic lethal properties for cancer-associated mutations. Nat. Struct. Mol. Biol. *18*, 721–727.

Tsai, A.G., Lu, H., Raghavan, S.C., Muschen, M., Hsieh, C.L., and Lieber, M.R. (2008). Human chromosomal translocations at CpG sites and a theoretical basis for their lineage and stage specificity. Cell *135*, 1130–1142.

Ward, I.M., and Chen, J. (2001). Histone H2AX is phosphorylated in an ATR-dependent manner in response to replicational stress. J. Biol. Chem. *276*, 47759–47762.

Ward, I.M., Reina-San-Martin, B., Olaru, A., Minn, K., Tamada, K., Lau, J.S., Cascalho, M., Chen, L., Nussenzweig, A., Livak, F., et al. (2004). 53BP1 is required for class switch recombination. J. Cell Biol. *165*, 459–464.

Yamane, A., Resch, W., Kuo, N., Kuchen, S., Li, Z., Sun, H.W., Robbiani, D.F., McBride, K., Nussenzweig, M.C., and Casellas, R. (2011). Deep-sequencing identification of the genomic targets of the cytidine deaminase AID and its cofactor RPA in B lymphocytes. Nat. Immunol. *12*, 62–69.

Yamane, A., Robbiani, D.F., Resch, W., Bothmer, A., Nakahashi, H., Oliveira, T., Rommel, P.C., Brown, E.J., Nussenzweig, A., Nussenzweig, M.C., et al. (2013). RPA accumulation during class switch recombination represents 5′-3′ DNA end resection during S-G2/M phase of the cell cycle. Cell Rep. Published January 02, 2013. http://dx.doi.org/10.1016/j.celrep.2012.12.006.

Zhang, J., MacLennan, I.C., Liu, Y.J., and Lane, P.J. (1988). Is rapid proliferation in B centroblasts linked to somatic mutation in memory B cell clones? Immunol. Lett. *18*, 297–299.

Zhang, J., Ding, L., Holmfeldt, L., Wu, G., Heatley, S.L., Payne-Turner, D., Easton, J., Chen, X., Wang, J., Rusch, M., et al. (2012a). The genetic basis of early T-cell precursor acute lymphoblastic leukaemia. Nature *481*, 157–163.

Zhang, Y., McCord, R.P., Ho, Y.J., Lajoie, B.R., Hildebrand, D.G., Simon, A.C., Becker, M.S., Alt, F.W., and Dekker, J. (2012b). Spatial organization of the mouse genome and its role in recurrent chromosomal translocations. Cell *148*, 908–921.

Palb2 synergizes with *Trp53* to suppress mammary tumor formation in a novel model of familial breast cancer

Christian Bowman-Colin[1], Bing Xia[2], Samuel Bunting[4], Christiaan Klijn[3,6], Rinske Drost[3], Peter Bouwman[3], Laura Fineman[1], Xixi Chen[1], Hong Cai[2], Jos Jonkers[3], Andre Nussenzweig[5], Chryssa Kanellopoulou[*1,7] and David M. Livingston[*1].

[*]corresponding authors

[1]Department of Cancer Biology, The Dana-Farber Cancer Institute, 450 Brookline Ave – SM870, Boston, MA 02215, USA.

[2]The Cancer Institute of New Jersey, 195 Little Albany Street, New Brunswick, NJ 08901, USA.

[3]Division of Molecular Pathology, The Netherlands Cancer Institute, Plesmanlaan 121, 1066 CX Amsterdam, The Netherlands.

[4]Rutgers University, Department of Molecular Biology and Biochemistry, 679 Hoes Lane, Piscataway, NJ 08854, USA.

[5]Laboratory of Genome Integrity, National Cancer Institute, National Institutes of Health, 37 Convent Drive, Bethesda, MD 20892, USA.

[6]Genentech, 1 DNA Way, South San Francisco, CA 94080, USA.

[7]Current address: Laboratory of Immunology, National Institute of Allergy and Infectious Diseases, National Institutes of Health, Bethesda, MD 20892, USA.

ABSTRACT

Germline mutations in *PALB2* lead to a familial predisposition to breast and pancreatic cancer or to Fanconi Anemia subtype N. PALB2 performs its tumor

suppressor role, at least in part, by supporting homologous recombination through interactions with BRCA1, BRCA2 and RAD51. To further understand the biology of PALB2-mediated tumor suppression, we targeted *Palb2* in the mouse. *Palb2*-deficient murine cells recapitulated DNA damage and checkpoint defects caused by PALB2 depletion in human cells. Similar to what happens after *Brca1* and *Brca2* ablation, germline *Palb2* deficiency in mice led to embryonic lethality, which could be delayed by ablation of checkpoint regulator genes such as *Cdkn1a* (p21) and *Cdkn2a* ($p16^{INK4A}$/$p19^{ARF}$). In contrast, somatic deletion of *Palb2* driven by *K14-Cre* led to tumor formation in the mammary glands, skin, and oral cavity with long latency. Mutation or loss of heterozygosity (LOH) of *Trp53* was frequently observed in these tumors. *Palb2* loss synergized with somatic *Trp53* loss to markedly accelerate tumor formation. Comparative genomic hybridization (CGH) analysis of *Palb2*/*Trp53* compound mutant breast tumors revealed distinct chromosomal aberrations that only partially overlapped with *Brca1*/*Trp53* and *Brca2*/*Trp53* compound mutant tumors, implying that the *Palb2* tumor suppression process is, in part, distinct from that executed by *Brca1* and *Brca2*. These observations underscore the usefulness of this new mouse model to investigate the molecular mechanisms underlying the breast tumor suppression functions of *Palb2*.

INTRODUCTION

PALB2 (Partner and Localizer of BRCA2) was recently identified as a major interacting protein of the breast cancer susceptibility gene product BRCA2[1]. This interaction is required for the repair of DNA double strand breaks by homologous recombination (HR), since PALB2 is necessary for the chromatin association of BRCA2 and its partner, RAD51[1]. RAD51 is the central recombinase in HR, involved in D-loop formation and strand displacement (PMID: 12778123). PALB2 also plays a BRCA2-independent role in the HR process by enhancing RAD51 function[2],(PMID: 20871615).

PALB2 was also found to interact with BRCA1 and, as such, supports the long known interaction between BRCA1 and BRCA2[3, 4]. Loss of PALB2 does not affect BRCA1 recruitment to irradiation-induced foci (IRIF), but abrogates localization of

BRCA2 and RAD51 at these structures. Genetic analyses have shown that, like BRCA2, a member of Fanconi anemia complementation group D1, PALB2 is also a Fanconi anemia protein (FANCN)[5, 6] and a breast tumor suppressor in its own right[7-10]. Unlike the case of BRCA1 and BRCA2-mutant tumors, only some *PALB2*-associated breast cancers have undergone loss of *PALB2* heterozygosity (LOH)[7, 8]. This implies that a reduction of *PALB2* gene copy number by half is sufficient to allow breast cancer development in some, but not all settings. Why this difference exists is an open question, and an experimental to address this question, among others, is in order.

Breast cancer in *PALB2*-mutated families appears to be of intermediate penetrance, unlike that in *BRCA1/2* families[8, 10]. Although *PALB2* mutations are rarer than *BRCA1/2* mutations, available clinical data indicate that heterozygous, germline *PALB2* mutations do not phenocopy precisely either *BRCA1* or *BRCA2* cancer predisposition syndromes[7, 8], consistent with the notion that PALB2 biological functions extend beyond solely bridging BRCA1-BRCA2 complex formation. Moreover, PALB2 also interacts with MRG15 (also known as MORF4L1)[11] a subunit of HAT/HDAC complexes and with KEAP1, a major regulator of the antioxidant transcription factor NRF2 (also known as NFE2L2)[12]. In addition, a highly conserved chromatin-associated domain (ChAM) has been described in a region of PALB2 for which there are no known binding partners[13]. The contribution of these PALB2 binding partners and of the ChAM domain to the BRCA1-PALB2-BRCA2 HR machinery and/or to hitherto unknown functions of PALB2, unrelated to homologous recombination is so far unclear.

In an effort to study how PALB2 contributes to breast cancer suppression, we generated the first model of high penetrance *Palb2* breast cancer in the mouse and assessed a number of its most salient properties. These insights are reported below.

RESULTS AND DISCUSSION

Targeting the mouse *Palb2* gene and the generation of *Palb2*-deficient ES cells

In order to generate a *Palb2* allele that could be conditionally inactivated upon Cre recombinase expression, we inserted *loxP* sites flanking exons 2 and 3 of the *Palb2* gene (Fig. S1B). These exons encode a putative nuclear localization signal (NLS) sequence and the PALB2 coiled-coil domain (Fig. 1A). The latter was previously shown to mediate the PALB2 interaction with BRCA1[3, 4]. Deletion of these exons resulted in out-of-frame reading of exon 4, leading to premature termination of the protein and exclusion of the BRCA2-interacting seven-bladed WD40-type β-propeller domain encoded by downstream exons. Due to the premature truncation of the *Palb2* open reading frame (ORF), the resulting transcript is also a candidate target for degradation by the nonsense-mediated decay (NMD) pathway.

Targeting of the *Palb2* locus and integration of both *loxP* sites was confirmed by Southern blot analysis (Fig. S1C). Heterozygous ES cells ($Palb2^{neo/+}$) were injected into blastocysts and the resulting chimeras from 2 individual clones were bred to either *Flp*-deleter mice (to eliminate the Frt-flanked Neo^r cassette) or *Cre*-deleter mice (to generate a conventional *Palb2* knockout allele). Germline transmission occurred from nearly all chimeras, and mice were PCR-genotyped for the Flp- or Cre-recombined alleles ($Palb2^{fl}$ or $Palb2^{-}$, respectively; Fig S1B).

$Palb2^{-/-}$ ES cells were derived from blastocysts of heterozygous $Palb2^{fl/-}$ crosses according to standard protocols. Three independent ES cell lines (1.1, 1.3 and 1.4) were generated from one such timed mating. Expression analysis of *Palb2* mRNA by quantitative real-time RT-PCR (qRT-PCR) confirmed that one of them was $Palb2^{fl/fl}$ and the other two were $Palb2^{-/-}$ (Fig. S1D), demonstrating that *Palb2* loss does not prevent ES cell derivation and subsequent survival. The three ES cell lines that were derived were morphologically comparable, proliferated at a similar rate to wild-type (WT) ES cells and could undergo differentiation into embryoid bodies (data not shown). The loss of full length *Palb2* expression in these lines was confirmed by qRT-PCR for *Palb2* mRNA (Fig. S1D) and by Western blotting, using an affinity-purified rabbit polyclonal anti-mouse PALB2 antibody (raised against the first 200 residues of the mouse PALB2 protein) (Fig. 1B).

ES cells that are deficient for *Brca1* or *Brca2* have been notoriously difficult to isolate and are severely compromised in their proliferation (PMID: 8698242, PMID: 9126738). Since PALB2 acts immediately upstream of BRCA2 and is required for BRCA2 localization at double strand breaks (DSBs), it is possible that the viability and robustness of the *Palb2*$^{-/-}$ cells was due to residual expression of a truncated *Palb2* species resulting from a downstream translation initiation that we could not detect with our antibody. In keeping with this possibility, *Palb2*$^{-/-}$ ES cells could not be derived from embryos carrying a conventional PALB2 gene-trap allele[14].

To test whether the conditional gene targeting approach that was employed had generated a functionally null allele, the response of *Palb2*$^{fl/fl}$ and *Palb2*$^{-/-}$ ES cells to DNA damaging agents that cause double strand breaks was analyzed. Normally, exposure of *PALB2*-proficient cells to ionizing radiation (IR) leads to the formation of γH2AX nuclear foci and subsequent recruitment to these structures of BRCA1, BRCA2 and RAD51 to these structures. As expected, γH2AX and BRCA1 foci formation was unaffected in *Palb2*$^{-/-}$ cells (Fig. 1C, Fig. S2A). However, the recruitment of RAD51 to IRIF was severely compromised, and no RAD51 colocalization with γH2AX foci could be detected after exposure of cells to IR (Fig. 1C). This defect was also evident at the biochemical level, since no increase in chromatin loading of RAD51 after IR was detected in *Palb2*$^{-/-}$ cells (Fig. 1D). Since biallelic PALB2 mutations in humans cause Fanconi anemia (FA), a hallmark of which is increased sensitivity to DNA cross-linking agents such as Mitomycin C (MMC), the sensitivity of *Palb2*$^{-/-}$ ES cells to MMC as well other DNA damaging agents was assayed. Both *Palb2*-deficient lines displayed increased sensitivity to MMC and IR (Fig. 1E, Fig. S2B-C). These findings reinforce the notion that these *Palb2*$^{-/-}$ cells are functional knock-outs for *Palb2*, as they appear compromised in all known *Palb2*-associated functions. Thus, upon Cre-mediated recombination *in vivo*, the aforementioned conditional *Palb2* allele should be converted to a *Palb2*-null allele.

Loss of *Palb2* in the germline results in early embryonic lethality

Germline deletion of *Brca1* or *Brca2* results in early embryonic lethality[15-17]. Although *Palb2*$^{-/-}$ ES cells displayed no significant growth defects in the absence of

exogenous DNA damage when compared with *Palb2*$^{fl/fl}$ controls, *Palb2* loss could be deleterious in differentiated progeny cells, and thereby negatively affect mouse development. Indeed, we were unable to obtain *Palb2*$^{-/-}$ mice from heterozygous crosses either at the time of weaning or at birth, consistent to previous reports[14, 18]. Dissection of embryos from timed pregnancies revealed that *Palb2*-null embryos could only be recovered up to E11.5, but only at sub-Mendelian ratios, and always presenting severe malformations. At earlier time points, morphological aberrations of *Palb2*$^{-/-}$ embryos were less obvious, although these mutant embryos were evidently smaller than WT or heterozygous littermates (Fig. 2A), some displaying exencephaly as well as malformations of the labyrinth and yolk sac-associated hematopoietic blood islets (Fig. 2C-F). The finding that *Palb2* deficiency results in embryonic lethality detectable at E8.5-E10.5 is largely consistent with earlier reports that homozygous *Palb2*-deficient mice, generated using a randomly-inserted gene-trap vector, also die during embryogenesis ~E8.5[14, 18].

Embryonic lethality due to loss of *Brca1* or *Brca2* can be delayed by concomitant loss of P53 and/or p21[19,20]. Likewise, p53 loss delayed the lethality of *Palb2* KO embryos[18], which also display increased levels of p21[18]. We therefore tested whether p21 deficiency would also have an effect on the embryonic lethality associated with *Palb2* nullizygosity. As expected, p21 deficiency did delay embryonic lethality of *Palb2* KO embryos by 2-3 days (Fig. 2B). A similar effect was observed when *Palb2*-deficient embryos were bred to a *p16*^{INK4A}-null allele (Fig. 2B); however, all *Palb2/p21* or *Palb2*/*p16*^{INK4A} double knockout embryos still displayed multiple malformations and impaired growth as compared with *Palb2* heterozygous or WT littermates (not shown), and were eventually resorbed.

Because the establishment of the placenta and onset of embryonic hematopoiesis are critical developmental steps that take place around the time of lethality of *Palb2* embryos, we set out to verify whether the lethality of *Palb2* KO embryos could be by-passed by a WT placenta. To this end, we used the *Palb2*$^{fl/fl}$ and *Palb2*$^{-/-}$ ES cells to perform tetraploid complementation assays. We found that embryos derived from the *Palb2*$^{-/-}$ ES cells were underdeveloped and malformed already at E9.5 when compared to their *Palb2*$^{fl/fl}$ counterparts (Fig. 2I-J). At E12.5, embryos derived from *Palb2*$^{fl/fl}$ ES

looked normal, whereas embryos from *Palb2*$^{-/-}$ ES cells were completely degenerated and resorbed (Fig. S3). Likewise, breeding of the *Palb2* conditional allele to *Meox2-Cre* KI mice (in which Cre is expressed from the endogenous *Meox2* locus only in the embryo proper[21]) only yielded mice in which *Palb2* deletion was incomplete (data not shown). Collectively, these findings indicate that *Palb2* is a developmentally essential gene, and its deficiency leads to multiple defects. These findings are also in accord with previous studies in which the lethality of *Brca1*$^{-/-}$ embryos was not rescued by tetraploid complementation assay[15].

Palb2 is a breast tumor suppressor in mice

In order to assess the effect of *Palb2* loss-of-function in mammary tumorigenesis, we crossed *Palb2*$^{fl/fl}$ mice with *K14-Cre* transgenic mice[22]. *K14-Cre* transgenic mice preferentially express Cre recombinase in the basal epithelium of the mammary ducts, as well as in other epithelial compartments such as skin and oral mucosa. *K14-Cre* has previously been used to model *Brca1* and *Brca2* loss-mediated mammary tumorigenesis in the mouse[23, 25].

In humans and mice, mammary tumor formation initiated by BRCA1 or BRCA2 loss requires concomitant loss of functional P53 (encoded by *Trp53* in mice)[23, 24]. Therefore, we set out to generate cohorts of *Palb2/Trp53* double conditional mice by crossing *Palb2*$^{fl/fl}$;*K14-Cre* transgenic mice with *Trp53*-floxed mice in order to assess the contribution of each gene alone and in combination to suppressing mammary tumor formation[23]. All mice that harbored the *K14-Cre* transgene or conditional alleles for *Palb2* and/or *Trp53* were phenotypically normal, fertile, and capable of nursing their litters.

During the period of tumor monitoring (up to 600 days after birth), *Trp53*$^{fl/fl}$;*K14-Cre* female mice developed spontaneous tumors with a frequency of ~80% and a mean tumor-free interval (T50) of 320 days. In contrast, *Palb2*$^{fl/fl}$;*Trp53*$^{fl/fl}$;*K14-Cre* double conditional mice displayed significantly decreased latency in tumor formation (T50 = 192 days, $P = 2.4\times10^{-5}$), indicating that *Palb2* loss significantly accelerates tumor formation

on a *Trp53* conditional null background (Fig. 3A). Most tumors in this double conditional KO group appeared between 130-200 days.

Somatic loss of one *Trp53* allele displayed, as expected, a haploinsufficient tumor suppressor phenotype, given that *Palb2*$^{fl/fl}$;*Trp53*$^{fl/+}$;*K14-Cre* mice developed tumors significantly faster than *Palb2*$^{fl/fl}$;*Trp53*$^{+/+}$;*K14-Cre* mice (T50 = 225 and 420 days, respectively, $P = 2.5\times10^{-12}$, Fig. S4C). *Palb2* loss of function also accelerated tumor formation on a *Trp53* heterozygous (fl/+) background, reiterating the synergistic interaction of these two genes (Fig 3B).

K14-Cre-mediated conditional loss of *Palb2* and *Trp53* predominantly led to tumor formation in breast, skin and oral mucosa (Fig. 3E), as previously reported for *Brca1* and *Brca2*[23, 25, 26]. While most of the tumors found in *Palb2*$^{+/+}$;*Trp53*$^{fl/fl}$;*K14-Cre* mice were breast carcinomas, *Palb2*/*Trp53* compound conditional KO mice displayed an expanded spectrum of tissues affected by tumors (Fig. 3E), suggesting that PALB2 tumor suppressor activities are not restricted to the mammary gland. Mice harboring conditional alleles for *Palb2* and *Trp53,* but no *K14-Cre* transgene, and *Palb2*$^{+/+}$;*Trp53*$^{+/+}$;*K14-Cre* mice did not display increased tumor susceptibility during the observation period, despite the intrinsic mutagenic activity of Cre in mammalian cells[27, 28]. Taken together, our results imply that the short latency and high penetrance of tumor formation observed in *Palb2*$^{fl/fl}$;*Trp53*$^{fl/fl}$;*K14-Cre* mice is primarily a result of synergy of the combined loss of *Palb2* and *Trp53*.

In order to assess the contribution of the loss of *Palb2* and/or *Trp53* alleles as driver mutations in the tumors that arose in *K14-Cre* mice, we determined the gene copy number for *Palb2* and *Trp53* by qPCR on tumor genomic DNA. All analyzed tumors from *Palb2*$^{fl/fl}$;*Trp53*$^{fl/fl}$;*K14-Cre* mice (12 out of 12) lost both floxed copies of *Palb2* and *Trp53* (Fig. 3D). Similarly, in all tumors from *Palb2*$^{fl/fl}$;*Trp53*$^{fl/+}$;*K14-Cre* mice (15 of 15) only residual signals could be detected for *Palb2* and *Trp53* allele copy number, suggesting that the conditional *Palb2* and *Trp53* alleles were fully recombined in most cells, whereas the WT copy of *Trp53* was lost through LOH. On the other hand, tumors that arose in *Palb2*$^{fl/+}$ mice displayed a heterogeneous pattern of loss of the conditional and WT *Palb2* or *Trp53* allele. Early reports describing lack of *PALB2* LOH in clinical tumor samples from heterozygous patients suggested that PALB2 could be a

haploinsufficient tumor suppressor in humans. Other reports showed that multiple *PALB2* tumors revealed *PALB2* LOH, implying that the *PALB2* tumor formation process is not rigidly uniform[7, 29, 30]. In our experimental setting, no haploinsufficiency was observed for *Palb2*, as indicated by the comparable latency in *Palb2*$^{fl/+}$;*Trp53*$^{fl/fl}$;*K14-Cre* and *Palb2*$^{+/+}$;*Trp53*$^{fl/fl}$;*K14-Cre* tumor development (P = 0.46, Fig. S4A). The same held true when similar cohorts of *Palb2*$^{+/+}$ and *Palb2*$^{fl/+}$ mice were compared on a *Trp53*$^{fl/+}$;*K14-Cre* background (P = 0.96, Fig S4B). Likewise, *Palb2* heterozygous mouse breast tumor lines displayed proper RAD51 localization at IRIF, consistent with preserved HR function. Tumor formation in this setting was not accelerated when compared with *Trp53*$^{-/-}$ tumor formation (Fig. 4C). As expected, *Palb2*-deficient breast tumor cell lines displayed the same defect in RAD51 accumulation observed in *Palb2*-deficient primary cells (Fig. 4C). This again points to a role for HR deficiency in the genesis of these tumors. Finally, all analyzed breast tumors from *K14-Cre* mice were negative for estrogen receptor (ER), progesterone receptor (PR) and ErbB2 (HER2), irrespective of the germline genotype (Fig 3F-H). This is consistent with what has been previously described for mouse breast tumors arising from *K14-Cre*-mediated conditional deletion of tumor suppressor genes[23, 25, 26].

Long latency tumors were also observed in *Palb2*$^{fl/fl}$;*K14-Cre* mice on a *Trp53* WT background (T50 = 420 days), but the tumor formation is still highly significant when compared with *Palb2*$^{+/+}$;*Trp53*$^{+/+}$;*K14-Cre* control mice (P = 5.4×10^{-10}) (Fig. 3C). The majority of these tumors were small lesions in the head/neck cavities, whereas a smaller subset of animals also developed mammary tumors. The finding that loss of *Palb2* alone is sufficient to induce tumor formation contrasts with most *Brca1* and *Brca2* mouse models in which short-medium latency breast tumor formation due to somatic loss of *Brca1/2* cannot be detected, unless *Trp53* is also co-deleted[23, 25, 31, 32]. One possible explanation for this finding is that somatic *Palb2* loss might be better tolerated than somatic *Brca1/2* loss on a *Trp53* WT background, which would be in keeping with the observation that *Palb2* deficiency leads to a less severe lethality phenotype in ES cells compared to *Brca1*/*Brca2* deficiency in the same setting. These *Palb2*-null and HR-deficient cells would survive and accumulate additional mutations that would eventually lead to tumor formation. The majority of the macroscopically dissectible tumors that

arose in *Palb2*$^{fl/fl}$;*Trp53*$^{+/+}$;*K14-Cre* mice had recombined both copies of *Palb2*. Two out of 7 mammary tumors gave rise to tumor cell lines. These tumors harbored inactivating *Trp53* mutations (not shown), again suggesting strongly that loss of p53 is ultimately required for *Palb2* loss-mediated tumor formation.

Genomic features of *Palb2*/*Trp53*-deficient mammary tumors

Genomic instability is a hallmark of human cancer, and it is believed to promote tumor initiation and progression. Experimental mouse tumor models have recapitulated this aspect of human tumorigenesis. In addition, aberrant tumor genomic profiles in such models have been shown to correlate with clinico-pathological features of the relevant tumor as well as with the results of certain signal transduction events. In order to gain insight into the genomic nature of the tumors that arose due to the loss of *Palb2*, we performed high-resolution comparative genomic hybridization (CGH) analysis of *Palb2/Trp53, Brca1/Trp53, Brca2/Trp53* and *Trp53* only-deficient mammary tumors.

Segmentation analysis of the CGH data was performed for each tumor in order to assess the number of genomic segments with deviating copy number changes as a readout of genomic instability[33]. The mammary tumors arising in *Palb2*$^{fl/fl}$;*Trp53*$^{fl/fl}$;*K14-Cre* mice (n=8) displayed higher numbers of amplified segments of the genome ($\log_2$ dose ≥ 0.5) than *Brca2*$^{fl/fl}$;*Trp53*$^{fl/fl}$;*K14-Cre* tumors (n=5; p = 0.046, Fig. S5). When compared to *Brca1*/*Trp53* tumors (n=5), which are known to display high levels of genomic instability, the CGH profiles of *Palb2*/*Trp53* tumors were equally fragmented (p = 0.94), indicating that *Palb2* loss also leads to formation of tumors that display a high degree of genomic instability. On the other hand, the number of homozygous deletions ($\log_2$ dose ≤ 0.5) detected in *Palb2*/*Trp53* tumors was significantly lower than that observed in *Brca1*/*Trp53* tumors (p = 0.035; Fig. S5), whereas *Palb2*/*Trp53* tumors were indistinguishable from *Brca2*/*Trp53* tumors in that regard (p = 0.45). Based on these analyses, *Palb2*/*Trp53* tumors seem to be phenotypically closer to *Brca1*/*Trp53* driven tumors in terms of genomic instability, but still distinct from tumors generated by either *Brca1*/*Trp53* or *Brca2*/*Trp53* loss. The implication for the trends observed is that PALB2 might possess biological roles that are, at least in part, not overlapping with its role in the

regulation of BRCA2 function. Notably, we were unable to identify chromosomal regions of imbalance that were unique to *Palb2*/*Trp53* tumors, but it is possible that a more comprehensive analysis with a larger collection of tumor samples might allow the identification of such regions.

53BP1 loss fails to rescue the HR defect caused by PALB2 deficiency

Loss of 53BP1 can rescue an HR defect observed in *BRCA1*-null cells and the lethality of *Brca1*$^{-/-}$ mice[34, 35] (REF 36, PMID: 22445484). Similarly, decreased expression of 53BP1 expression was linked to triple negative breast cancers as well as to human *BRCA1* tumors[36]. We then asked whether *Trp53bp1* is absent from *Palb2*/*Trp53* KO tumors, and whether its absence would rescue the HR defect associated with *Palb2* loss. Quantitative RT-PCR analysis of *Trp53bp1* mRNA in freshly isolated *Palb2* tumor samples showed that *Trp53bp1* mRNA levels were not significantly downregulated in *Palb2*-deficient breast tumors in comparison with *Palb2* WT tumor controls, although some tumors displayed reduced *Trp53bp1* mRNA levels (Fig. 4A).

To determine whether HR deficiency due to *Palb2* loss could be complemented by *Trp53bp1* loss in primary cells, we generated *Palb2*$^{fl/fl}$;*CD19-Cre* mice that were or were not deficient in *Trp53bp1*. Cultured primary splenocytes from these mice were then assayed for their HR competence upon treatment with PARP1 inhibitors (PARPi), which selectively induces DNA damage and chromosomal aberrations in HR-deficient cells[37]. Treatment with Olaparib (PARPi) induced accumulation of chromosomal and chromatid breaks, and radial structures in chromosomal spreads from cultured *Palb2*$^{fl/fl}$; *Trp53bp1*$^{+/-}$; *CD19-Cre* primary splenocytes. The number of chromosomal aberrations was comparable in *Palb2*$^{fl/fl}$; *Trp53bp1*$^{-/-}$; *CD19-Cre* splenocytes, implying that *Trp53bp1* deletion did not complement the HR defect caused by *Palb2* deficiency (Fig. S6). *Trp53bp1* deletion also failed to rescue the chromosomal aberrations found in spreads from PARPi-treated *Brca2*$^{fl/fl}$; *Trp53bp1*$^{-/-}$; *CD19-Cre* splenocytes. In the same experiment, complete rescue of the DNA repair deficiency in *Brca1*$^{fl/fl}$; *Trp53bp1*$^{-/-}$; *CD19-Cre* splenocytes was observed as previously described[35, 36]. These observations suggest that the contributions of PALB2 and BRCA2 to HR-based DSB repair are

distinct from those of BRCA1, and cannot be complemented by 53BP1 loss. In keeping with existing evidence, PALB2 and BRCA2 may well be *de facto* downstream HR effectors, which cannot be replaced or bypassed, except by artificially forcing the loading of RAD51 onto chromatin at/near DSB (REF 36, [38-40]) . These observations, along with earlier results (PMID: 20871615), also suggest that PARP1 inhibition is a potential therapeutic target in *PALB2*-deficient tumors, to the same extent that it is in *BRCA1*- and *BRCA2*-associated tumors[37].

CONCLUSIONS

In summary, we have shown that *Palb2* is a breast tumor suppressor gene in mice as it is in humans, and synergizes with *Trp53* to suppress tumor formation. However, tumorigenesis driven by *Palb2* loss in the mouse is not entirely suppressed on a *Trp53* WT germline background, unlike most *Brca1* and *Brca2* mouse models of breast tumorigenesis (PMID: 16998503). Despite some similarities to *Brca2*;*Trp53*;*K14-Cre* breast tumors, *Palb2* tumors still display certain divergent features that, together, support the notion that PALB2 possesses additional biological functions that might not be related to HR and/or its interaction with BRCA2, as judged by the divergent chromosomal aberration pattern observed in between *Palb2*- and *Brca2*-derived tumors and for the fact that *Palb2*$^{fl/fl}$*;K14-Cre* conditional mice which are *Trp53* WT still develop tumors with long latency, unlike *Brca2*$^{fl/fl}$;*K14-Cre* mice. Finally, haploinsufficiency for *Palb2* tumor suppression was not detected in this model, although one cannot rule out that it would be manifest in a different model system and/or with enlarged cohorts of experimental mice. For example, the tumors in this mouse model driven by *K14-Cre* were uniformly of the triple negative phenotype. This difference might well contribute to the absence of haploinsufficiency in our system, in the same fashion that distinct cell populations in the human mammary gland display preferential patterns of consecutive LOH events along the tumorigenesis pathway associated with BRCA1 loss[41]. We believe that this mouse model will be useful in further studies aimed at unraveling the molecular pathways in which PALB2 plays a role.

Figure legends

Figure 1. Conditional gene targeting of mouse *Palb2*. A) Schematic representation of *Palb2* domains and the exons from which they are encoded. The shaded area corresponds to the truncated open reading frame encoded upon recombination of the inserted *loxP* recombination sites. B) Western blot analysis for PALB2 in chromatin fraction extracts (S420) of three independent ES cell lines. The full length mouse PALB2 protein is ~120 kDa. An unspecific background band is indicated by an asterisk, and can be used as an internal loading control. **C)** Recruitment of RAD51 to DSBs marked by γH2AX IRIF 2h after exposure to 5 Gy of ionizing radiation in $Palb2^{fl/fl}$ and $Palb2^{-/-}$ ES cells. **D)** Western blot analysis of chromatin-bound (S420) RAD51 in $Palb2^{fl/fl}$ and $Palb2^{-/-}$ ES cells that received 10 Gy of IR and their respective unirradiated control. Histone H3 was used as a loading control. **E)** Dose-response curves of $Palb2^{fl/fl}$ and $Palb2^{-/-}$ ES cells after exposure to increasing concentrations of the radiomimetic neocarzinostatin.

Figure 2. Early lethality of $Palb2^{-/-}$ embryos. **A)** Bright-field images of $Palb2^{+/+}$ and $Palb2^{-/-}$ embryos at E10.5. Arrow indicates brain exencephaly. **B)** Graph indicating the p-values of Hardy-Weinberg disequilibrium for *Palb2* KO embryos retrieved from $Palb2^{+/-}$ matings at various embryonic ages. Both *Cdkn1a* (*p21*)- or *Cdkn2a* ($p16^{INK4A}$)-deficient backgrounds delay the lethality of *Palb2*-deficient embryos and the time point at which the counterselection of *Palb2* KO embryos become significant ($p < 0.05$). **C-H)** Hematoxylin-eosin staining of placenta (C, F) and yolk sac blood islets of WT (C-E) or $Palb2^{-/-}$ embryos (F-H). Pictures E and H display higher magnification of the areas delimited on D and G. **I-J)** Hematoxylin-eosin staining of *in utero* embryo sections from tetraploid complementation assay at E9.5, utilizing $Palb2^{fl/fl}$ ES cells (I) or $Palb2^{-/-}$ ES cells (J).

Figure 3. Tumor formation in $Palb2^{fl/fl}$;$Trp53^{fl/fl}$;*K14-Cre* mice. **A-C)** Kaplan-Meier curves displaying that *Palb2* loss accelerates tumor formation both under a *Trp53* conditional null background (A) as well under a *Trp53* conditional heterozygous background (B) and finally on a *Trp53* WT background. **D)** *Palb2* (top panels) and *Trp53* (lower panels) gene dosages of mammary tumors derived from *Palb2/Trp53* double

conditional mouse cohorts. The germline *Palb2* and *Trp53* genotypes of the mice are indicated in red below the graphs. **E)** Spectrum of tumors arising in mouse cohorts with different combinations of *Palb2* and *Trp53* alleles. The genotypes of the mice are shown below the graphs. **F-H)** Mammary tumors arising in *Palb2/Trp53* double conditional mice are triple-negative. Representative IHC stainings for ER (F), PR (G) and HER2 (H). The arrows on the top left corner of F) and G) indicates an *in situ* ductal carcinoma structures that displays the typical nuclear positivity for ER and PR, respectively.

Figure 4. The HR defect in *Palb2*-deficient cells and tumors. **A)** RT-qPCR for *Trp53bp1* mRNA in freshly isolated tumor samples that are either *Palb2*-proficient (+/+ and +/-) or *Palb2*-deficient (-/-). **B)** Distinct defects observed in chromosome spreads of acute chromosomal damage and genome instability following PARPi treatment are not rescued by *Trp53bp1* deletion in $Palb2^{fl/fl}$*;CD19-Cre* B-lymphocytes. **C)** Established *Palb2/Trp53*-deficient breast tumor cell lines have not reversed the defect of recruitment of RAD51 to IRIF, whereas *Palb2* heterozygosity does not impair the proper IRIF localization of RAD51 in breast tumor lines, compared with *Palb2* WT control breast tumor lines.

Figure S1. **A)** Schematic representation of the targeting strategy. The wild-type allele (WT), targeting construct and targeted allele are depicted. Dashed lines indicate regions of homology. Black triangles represent *loxP* sites, and arrows represents the primers used for RT-PCR. **B)** Southern blot of genomic DNA from targeted ES cell clones digested with indicated restriction enzyme (BamHI or BsaBI), and hybridized with 5' and 3' probe. Note that only some of the targeted clones (3' probe) that show cointegration of the second *loxP* site with the 5' probe were used. **C)** Real-time RT-PCR analysis of *Palb2* mRNA levels in three ES cell lines of the indicated genotypes derived from heterozygous $Palb2^{fl/-}$ crosses.

Figure S2. Response of $Palb2^{-/-}$ cells to DNA damage. **A)** Recruitment of BRCA1 to DSBs marked by γH2AX foci 2h after exposure to 5 Gy of ionizing radiation both in $Palb2^{fl/fl}$ and $Palb2^{-/-}$ cells. **B-C)** Survival curves of $Palb2^{fl/fl}$ and $Palb2^{-/-}$ ES cell lines to DNA damaging agents such as mitomycin C (B) and IR (C).

Figure S3. *Palb2* WT placentas do not rescue the lethality of *Palb2*$^{-/-}$ embryos. Hematoxylin-eosin section staining of embryos from tetraploid complementation assay. E12.5 derived from WT tetraploid embryo aggregation with either *Palb2*$^{fl/fl}$ ES cells (left) or *Palb2*$^{-/-}$ ES cells (right). By this stage (E12.5), all *Palb2*$^{-/-}$ embryos have been reabsorbed (arrows).

Figure S4. Effects of *Palb2* and *Trp53* heterozygosity in *K14-Cre* mice. Kaplan-Meier curves of tumor-free survival indicating that *Palb2* is not haploinsufficient for tumor formation either on a *Trp53* conditional null (A) or conditional heterozygous background (B). On the other hand, *Trp53* displays a strong haploinsufficient tumor phenotype on a *Palb2*$^{fl/fl}$ background (C).

Figure S5. CGH analysis of *Palb2* tumors. **A)** Control (spleen) and tumor DNA was hybridized to whole genome arrays to determine regions of loss or gains in mouse breast tumor samples. Representative rainbow graphs for each tumor genotype showing $\log_2$ DNA copy number ratio (tumor/spleen) across the entire genome. **(B-C)** Dot plots of the number and dose ratio of high-level amplification ($\log_2 > 0.5$, B) or homozygous deletion events ($\log_2 < -0.5$, C). Each dot represents an amplification/deletion event, with its corresponding relative dose. Asterisks indicate differences that were statistically significant ($p < 0.05$).

Figure S6. Rescue of the PARPi-induced acute chromosomal damage in *Brca1/2*-deficient B-lymphocytes by *Trp53bp1* deletion. *Trp53bp1* deletion is able to rescue defects observed in chromosome spreads from PARPi-treated *Brca1*-deficient B-lymphocytes (*Brca1*$^{fl/fl}$*;CD19-Cre*) (**A),** but cannot rescue the damage in *Brca2*-deficient B-lymphocytes **(B)**.

REFERENCES

1. Xia, B. et al. Control of BRCA2 cellular and clinical functions by a nuclear partner, PALB2. Mol Cell 22, 719-29 (2006).
2. Dray, E. et al. Enhancement of RAD51 recombinase activity by the tumor suppressor PALB2. Nat Struct Mol Biol 17, 1255-9 (2010).

3. Sy, S. M., Huen, M. S. & Chen, J. PALB2 is an integral component of the BRCA complex required for homologous recombination repair. Proc Natl Acad Sci U S A 106, 7155-60 (2009).
4. Zhang, F. et al. PALB2 links BRCA1 and BRCA2 in the DNA-damage response. Curr Biol 19, 524-9 (2009).
5. Reid, S. et al. Biallelic mutations in PALB2 cause Fanconi anemia subtype FA-N and predispose to childhood cancer. Nature Genetics 39, 162-4 (2007).
6. Xia, B. et al. Fanconi anemia is associated with a defect in the BRCA2 partner PALB2. Nat Genet 39, 159-61 (2007).
7. Tischkowitz, M. et al. Analysis of PALB2/FANCN-associated breast cancer families. Proc Natl Acad Sci U S A 104, 6788-93 (2007).
8. Erkko, H. et al. A recurrent mutation in PALB2 in Finnish cancer families. Nature 446, 316-9 (2007).
9. Jones, S. et al. Exomic sequencing identifies PALB2 as a pancreatic cancer susceptibility gene. Science 324, 217 (2009).
10. Rahman, N. et al. PALB2, which encodes a BRCA2-interacting protein, is a breast cancer susceptibility gene. Nature Genetics 39, 165-7 (2007).
11. Sy, S. M., Huen, M. S. & Chen, J. MRG15 is a novel PALB2-interacting factor involved in homologous recombination. J Biol Chem 284, 21127-31 (2009).
12. Ma, J. et al. PALB2 interacts with KEAP1 to promote NRF2 nuclear accumulation and function. Mol Cell Biol 32, 1506-17 (2012).
13. Bleuyard, J. Y., Buisson, R., Masson, J. Y. & Esashi, F. ChAM, a novel motif that mediates PALB2 intrinsic chromatin binding and facilitates DNA repair. EMBO Rep 13, 135-41 (2012).
14. Rantakari, P. et al. Inactivation of Palb2 gene leads to mesoderm differentiation defect and early embryonic lethality in mice. Hum Mol Genet 19, 3021-9 (2010).
15. Hakem, R. et al. The tumor suppressor gene Brca1 is required for embryonic cellular proliferation in the mouse. Cell 85, 1009-23 (1996).
16. Suzuki, A. et al. Brca2 is required for embryonic cellular proliferation in the mouse. Genes Dev 11, 1242-52 (1997).
17. Liu, C. Y., Flesken-Nikitin, A., Li, S., Zeng, Y. & Lee, W. H. Inactivation of the mouse Brca1 gene leads to failure in the morphogenesis of the egg cylinder in early postimplantation development. Genes Dev 10, 1835-43 (1996).
18. Bouwman, P. et al. Loss of p53 partially rescues embryonic development of Palb2 knockout mice but does not foster haploinsufficiency of Palb2 in tumour suppression. J Pathol 224, 10-21 (2011).
19. Ludwig, T., Chapman, D. L., Papaioannou, V. E. & Efstratiadis, A. Targeted mutations of breast cancer susceptibility gene homologs in mice: lethal phenotypes of Brca1, Brca2, Brca1/Brca2, Brca1/p53, and Brca2/p53 nullizygous embryos. Genes Dev 11, 1226-41 (1997).
20. Hakem, R., de la Pompa, J. L., Elia, A., Potter, J. & Mak, T. W. Partial rescue of Brca1 (5-6) early embryonic lethality by p53 or p21 null mutation. Nat Genet 16, 298-302 (1997).
21. Tallquist, M. D. & Soriano, P. Epiblast-restricted Cre expression in MORE mice: a tool to distinguish embryonic vs. extra-embryonic gene function. Genesis 26, 113-5 (2000).

22. Dassule, H. R., Lewis, P., Bei, M., Maas, R. & McMahon, A. P. Sonic hedgehog regulates growth and morphogenesis of the tooth. Development 127, 4775-85 (2000).
23. Jonkers, J. et al. Synergistic tumor suppressor activity of BRCA2 and p53 in a conditional mouse model for breast cancer. Nat Genet 29, 418-25 (2001).
24. Holstege, H. et al. High incidence of protein-truncating TP53 mutations in BRCA1-related breast cancer. Cancer Res 69, 3625-33 (2009).
25. Liu, X. et al. Somatic loss of BRCA1 and p53 in mice induces mammary tumors with features of human BRCA1-mutated basal-like breast cancer. Proc Natl Acad Sci U S A 104, 12111-6 (2007).
26. Molyneux, G. et al. BRCA1 basal-like breast cancers originate from luminal epithelial progenitors and not from basal stem cells. Cell Stem Cell 7, 403-17 (2010).
27. Loonstra, A. et al. Growth inhibition and DNA damage induced by Cre recombinase in mammalian cells. Proc Natl Acad Sci U S A 98, 9209-14 (2001).
28. Silver, D. P. & Livingston, D. M. Self-excising retroviral vectors encoding the Cre recombinase overcome Cre-mediated cellular toxicity. Mol Cell 8, 233-43 (2001).
29. Garcia, M. J. et al. Analysis of FANCB and FANCN/PALB2 fanconi anemia genes in BRCA1/2-negative Spanish breast cancer families. Breast cancer research and treatment 113, 545-51 (2009).
30. Casadei, S. et al. Contribution of inherited mutations in the BRCA2-interacting protein PALB2 to familial breast cancer. Cancer research 71, 2222-9 (2011).
31. Xu, X. et al. Conditional mutation of Brca1 in mammary epithelial cells results in blunted ductal morphogenesis and tumour formation. Nat Genet 22, 37-43 (1999).
32. Ludwig, T., Fisher, P., Ganesan, S. & Efstratiadis, A. Tumorigenesis in mice carrying a truncating Brca1 mutation. Genes Dev 15, 1188-93 (2001).
33. de Ronde, J. J. et al. KC-SMARTR: An R package for detection of statistically significant aberrations in multi-experiment aCGH data. BMC Res Notes 3, 298 (2010).
34. Cao, L. et al. A selective requirement for 53BP1 in the biological response to genomic instability induced by Brca1 deficiency. Mol Cell 35, 534-41 (2009).
35. Bunting, S. F. et al. 53BP1 inhibits homologous recombination in Brca1-deficient cells by blocking resection of DNA breaks. Cell 141, 243-54 (2010).
36. Bouwman, P. et al. 53BP1 loss rescues BRCA1 deficiency and is associated with triple-negative and BRCA-mutated breast cancers. Nat Struct Mol Biol 17, 688-95 (2010).
37. Farmer, H. et al. Targeting the DNA repair defect in BRCA mutant cells as a therapeutic strategy. Nature 434, 917-21 (2005).
38. Brown, E. T. & Holt, J. T. Rad51 overexpression rescues radiation resistance in BRCA2-defective cancer cells. Mol Carcinog 48, 105-9 (2009).
39. Martin, R. W. et al. RAD51 up-regulation bypasses BRCA1 function and is a common feature of BRCA1-deficient breast tumors. Cancer Res 67, 9658-65 (2007).

40. Schild, D. & Wiese, C. Overexpression of RAD51 suppresses recombination defects: a possible mechanism to reverse genomic instability. Nucleic Acids Res 38, 1061-70 (2010).
41. Martins FC et al. Evolutionary pathways in BRCA1-associated breast tumors. Cancer Discov 6, 503-11 (2012).

Figure 1

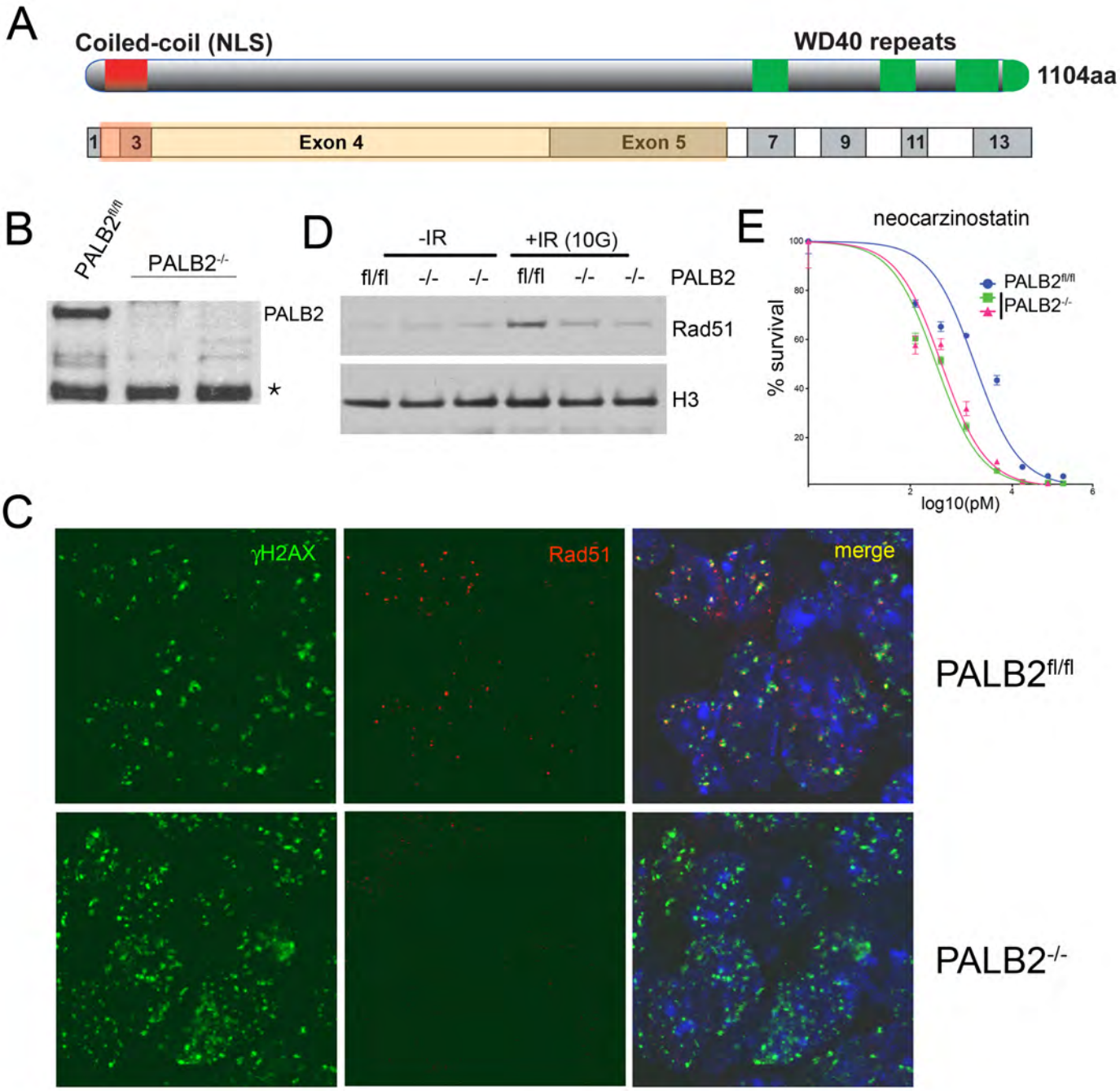
A
Coiled-coil (NLS)
WD40 repeats
1104aa
1
3
Exon 4
Exon 5
7
9
11
13
B
PALB2fl/fl
PALB2-/-
PALB2
*
D
-IR
+IR (10G)
fl/fl
-/-
-/-
fl/fl
-/-
-/-
PALB2
Rad51
H3
E
neocarzinostatin
% survival
log10(pM)
PALB2fl/fl
PALB2-/-
C
γH2AX
Rad51
merge
PALB2fl/fl
PALB2-/-

Figure 2

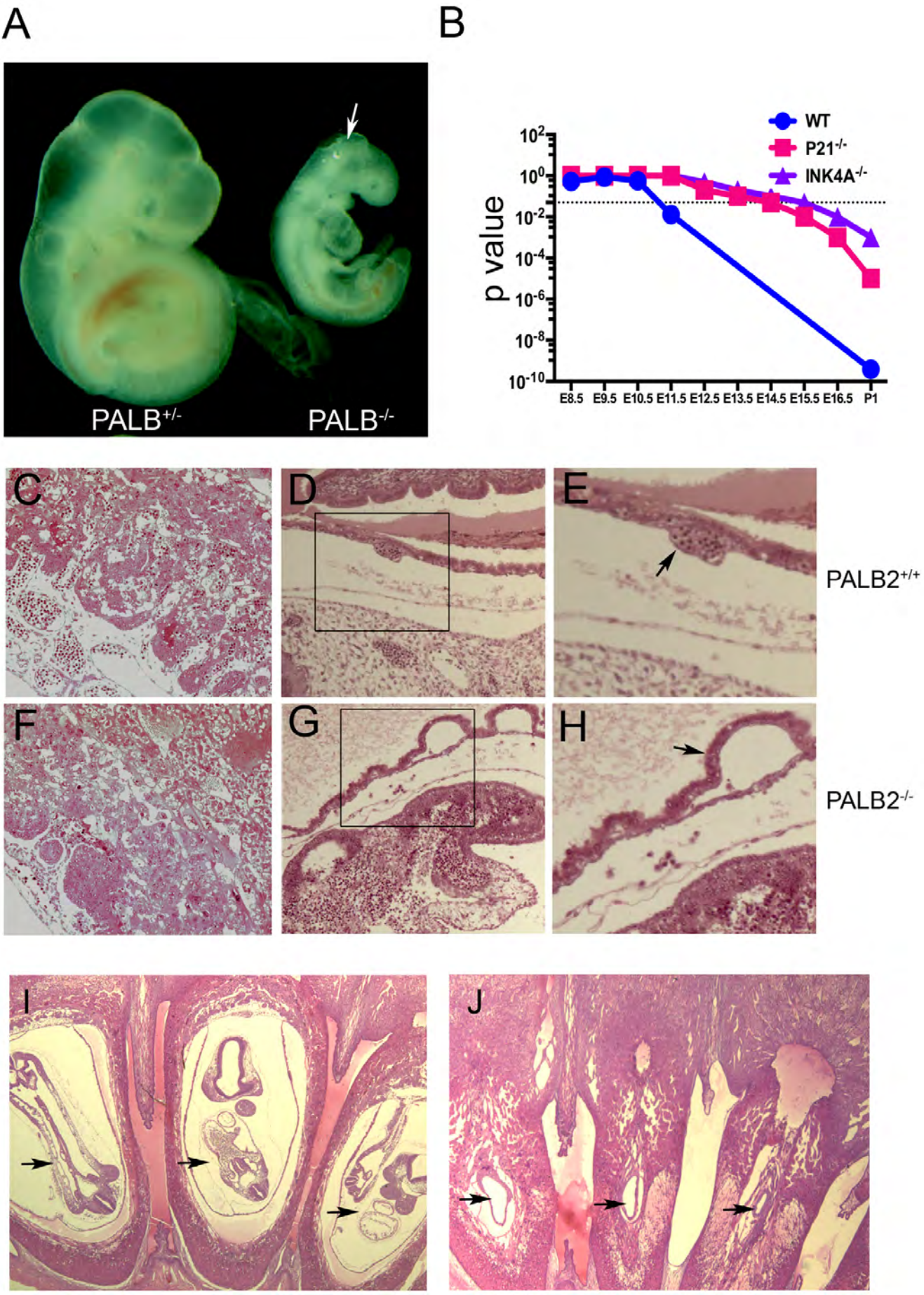
A
B
PALB+/-
PALB-/-
WT
P21-/-
INK4A-/-
p value
E8.5 E9.5 E10.5 E11.5 E12.5 E13.5 E14.5 E15.5 E16.5 P1
C
D
E
F
G
H
PALB2+/+
PALB2-/-
I
J

Figure 3

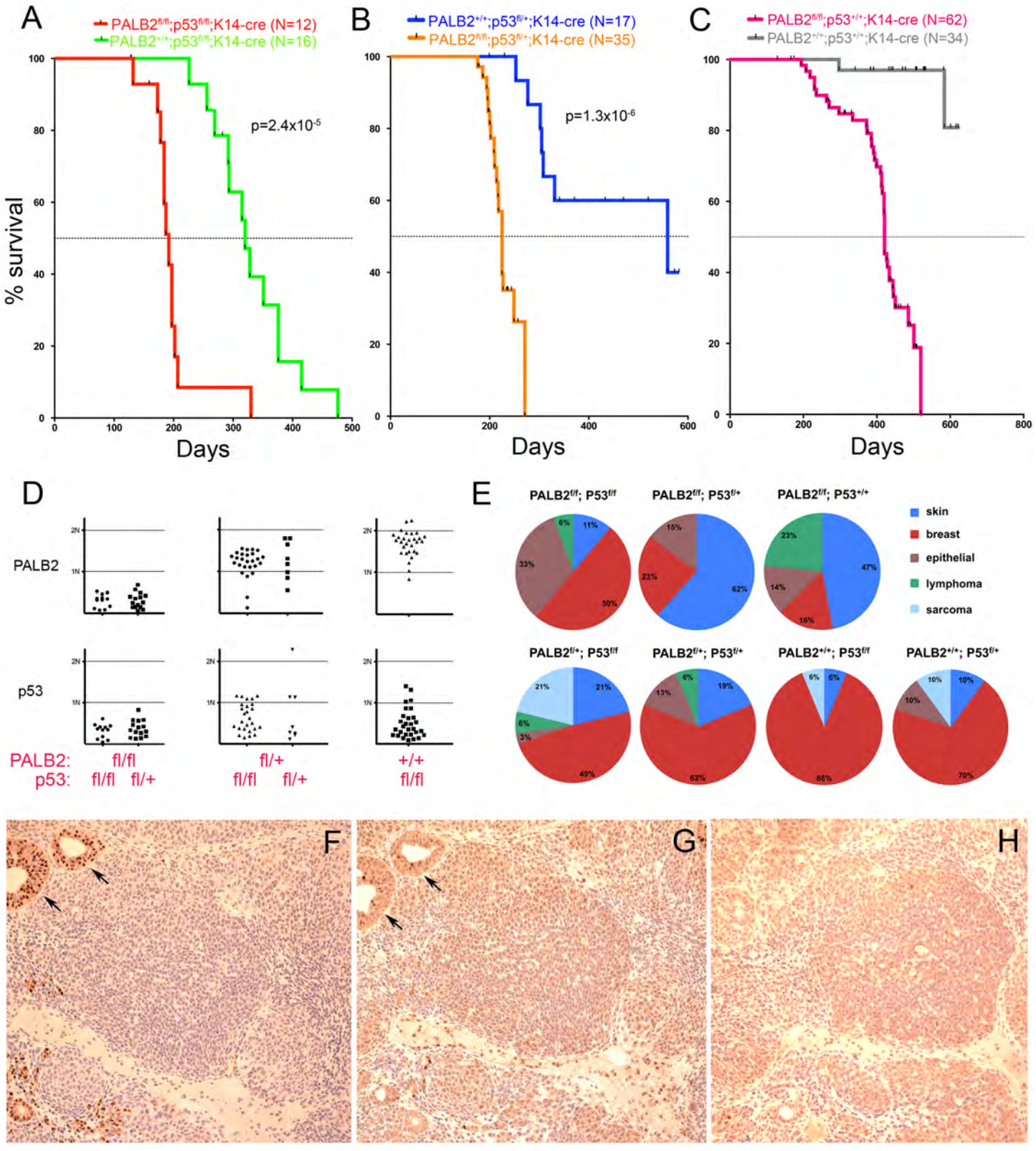
A
PALB2fl/fl;p53fl/fl;K14-cre (N=12)
PALB2+/+;p53fl/fl;K14-cre (N=16)
p=2.4x10-5
% survival
Days
B
PALB2+/+;p53fl/+;K14-cre (N=17)
PALB2fl/fl;p53fl/+;K14-cre (N=35)
p=1.3x10-6
Days
C
PALB2fl/fl;p53+/+;K14-cre (N=62)
PALB2+/+;p53+/+;K14-cre (N=34)
Days
D
PALB2
p53
PALB2: fl/fl fl/+ +/+
p53: fl/fl fl/+ fl/fl fl/+ fl/fl
E
PALB2f/f; P53f/f
PALB2f/f; P53f/+
PALB2f/f; P53+/+
PALB2f/+; P53f/f
PALB2f/+; P53f/+
PALB2+/+; P53f/f
PALB2+/+; P53f/+
skin
breast
epithelial
lymphoma
sarcoma
F
G
H

Figure 4

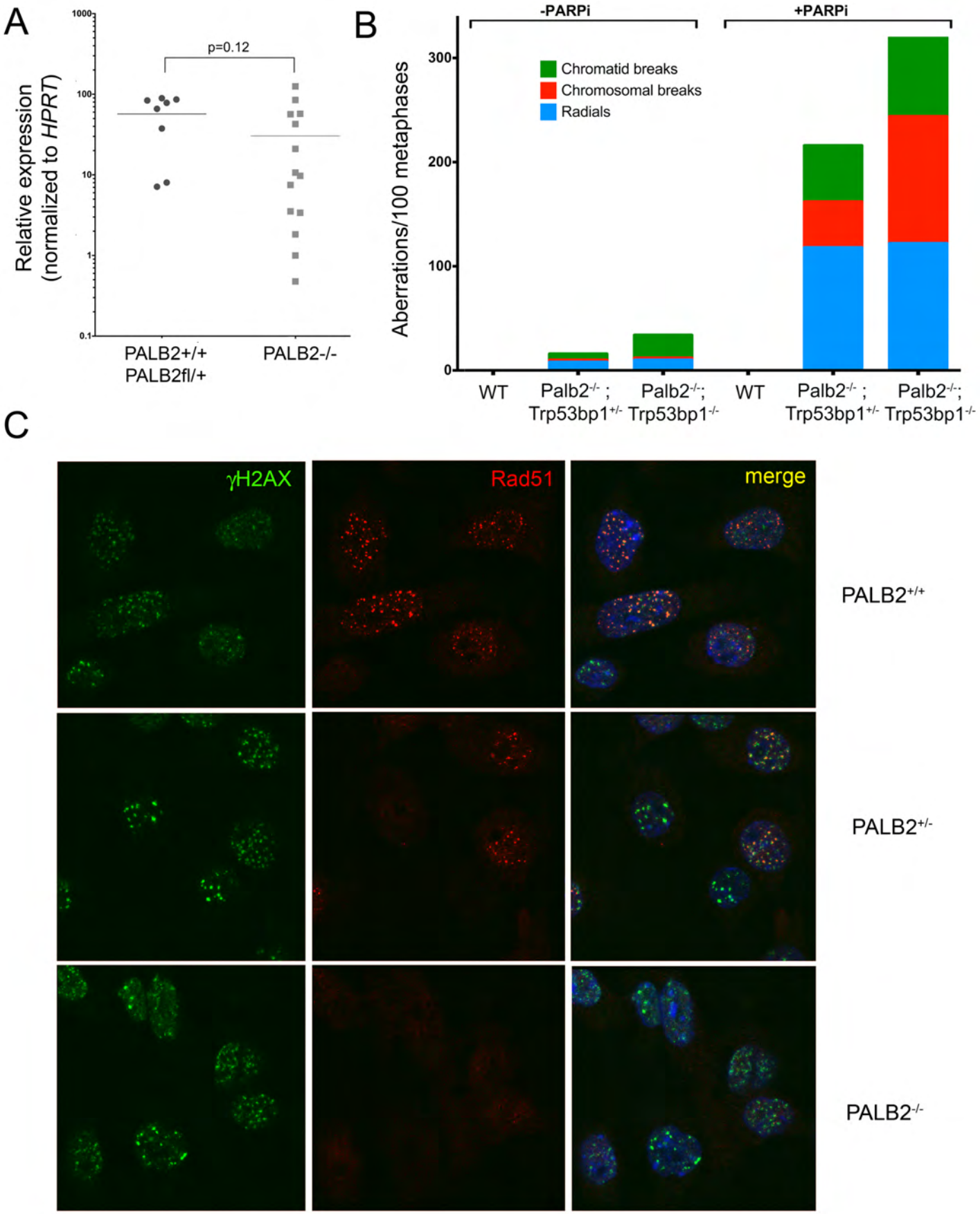
A
Relative expression (normalized to HPRT)
1000
100
10
1
0.1
p=0.12
PALB2+/+ PALB2fl/+
PALB2-/-
B
-PARPi
+PARPi
Aberrations/100 metaphases
300
200
100
0
Chromatid breaks
Chromosomal breaks
Radials
WT
Palb2-/- ; Trp53bp1+/-
Palb2-/-; Trp53bp1-/-
WT
Palb2-/- ; Trp53bp1+/-
Palb2-/-; Trp53bp1-/-
C
γH2AX
Rad51
merge
PALB2+/+
PALB2+/-
PALB2-/-

Figure S1

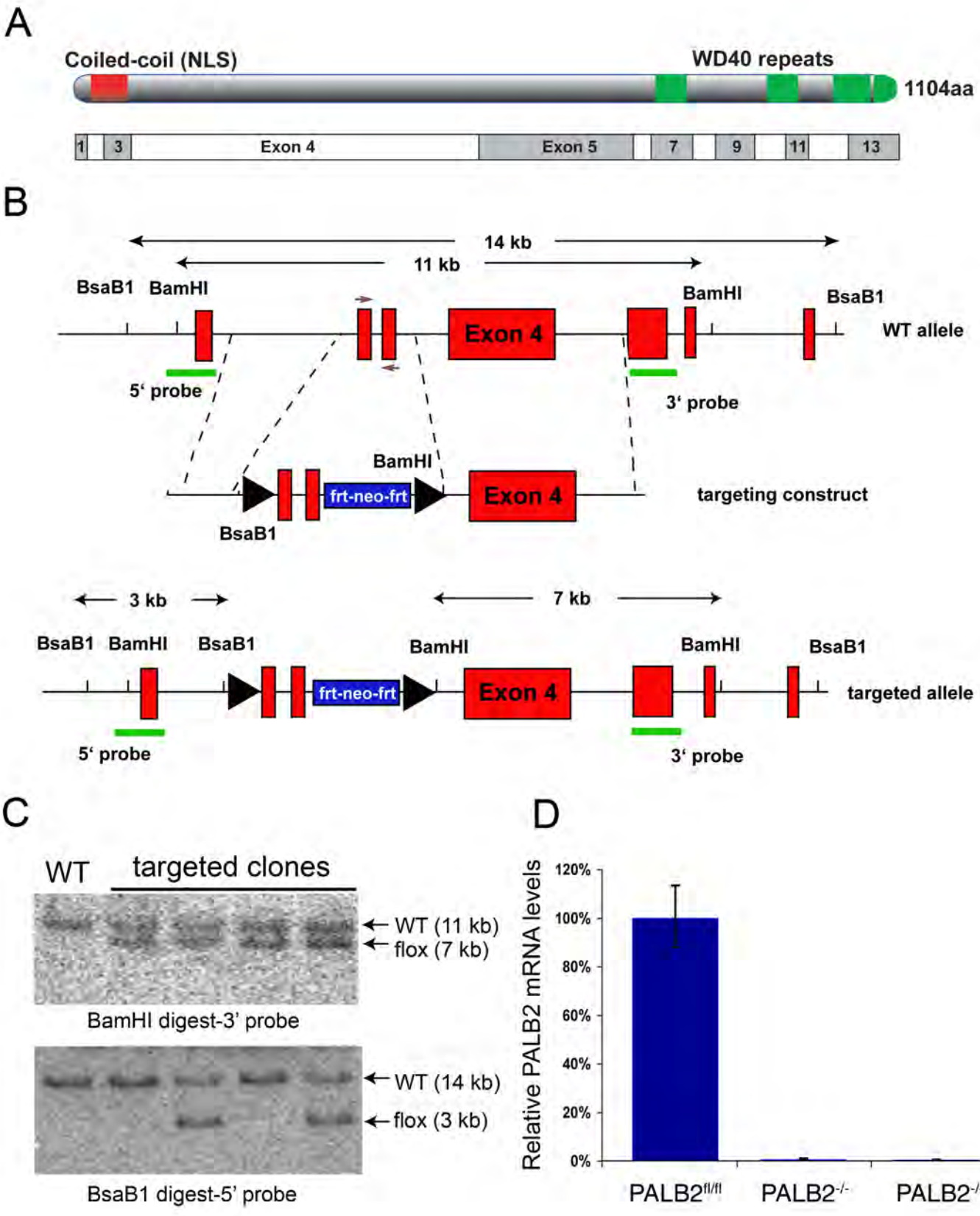
A
Coiled-coil (NLS)
WD40 repeats
1104aa
1
3
Exon 4
Exon 5
7
9
11
13
B
14 kb
11 kb
BsaB1
BamHI
BamHI
BsaB1
Exon 4
WT allele
5‘ probe
3‘ probe
BamHI
frt-neo-frt
Exon 4
targeting construct
BsaB1
3 kb
7 kb
BsaB1
BamHI
BsaB1
BamHI
BamHI
BsaB1
frt-neo-frt
Exon 4
targeted allele
5‘ probe
3‘ probe
C
WT
targeted clones
WT (11 kb)
flox (7 kb)
BamHI digest-3’ probe
WT (14 kb)
flox (3 kb)
BsaB1 digest-5’ probe
D
Relative PALB2 mRNA levels
120%
100%
80%
60%
40%
20%
0%
PALB2fl/fl
PALB2-/-
PALB2-/-

Figure S2

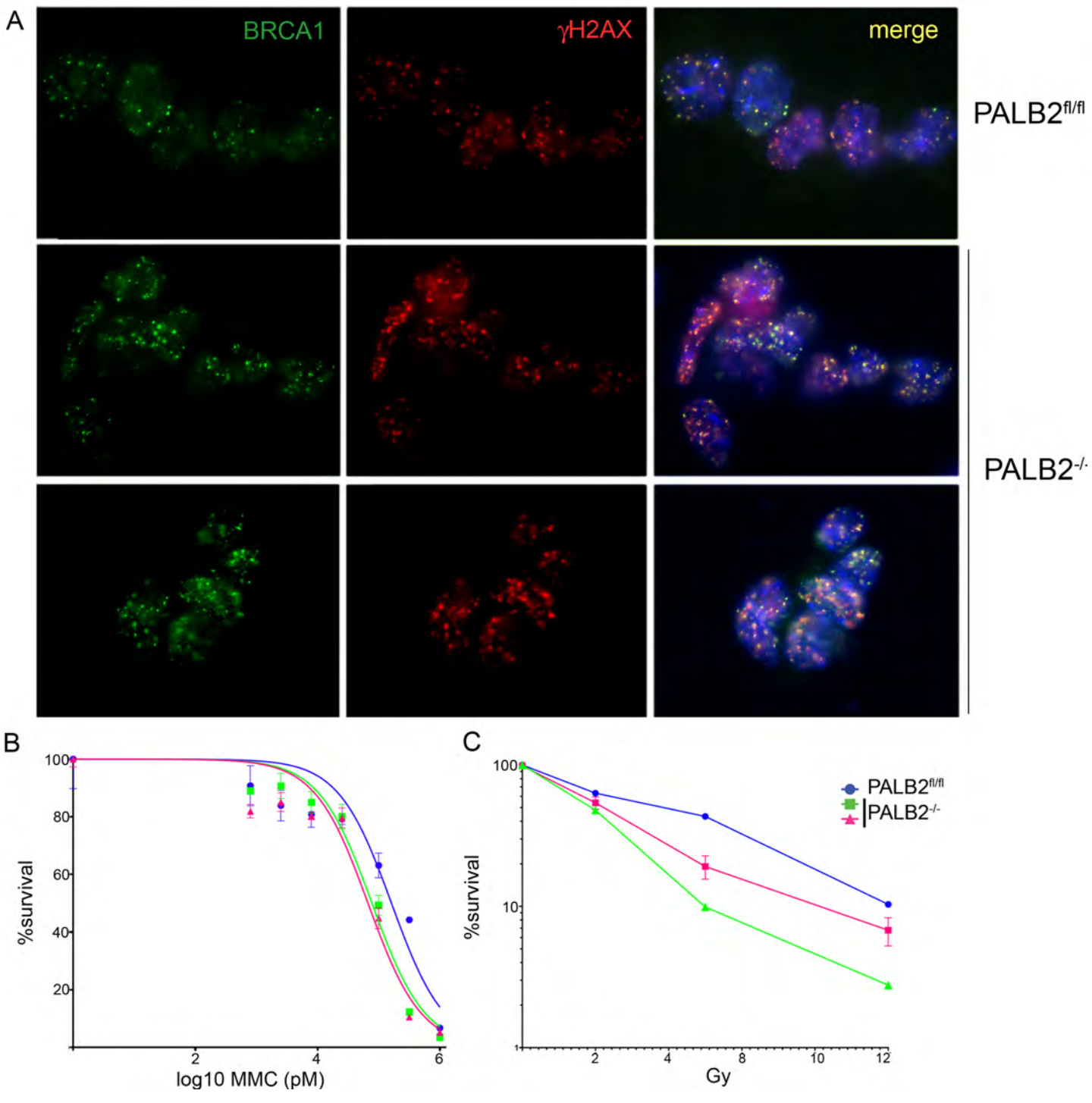
A
BRCA1
γH2AX
merge
PALB2fl/fl
PALB2-/-
B
%survival
log10 MMC (pM)
C
%survival
Gy
PALB2fl/fl
PALB2-/-

Figure S3

PALB2$^{fl/fl}$ *dpc* 12.5

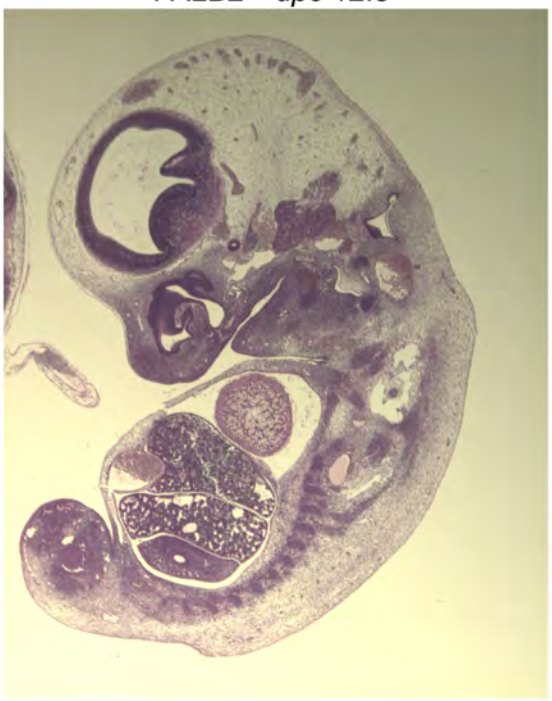

PALB2$^{-/-}$ *dpc* 12.5

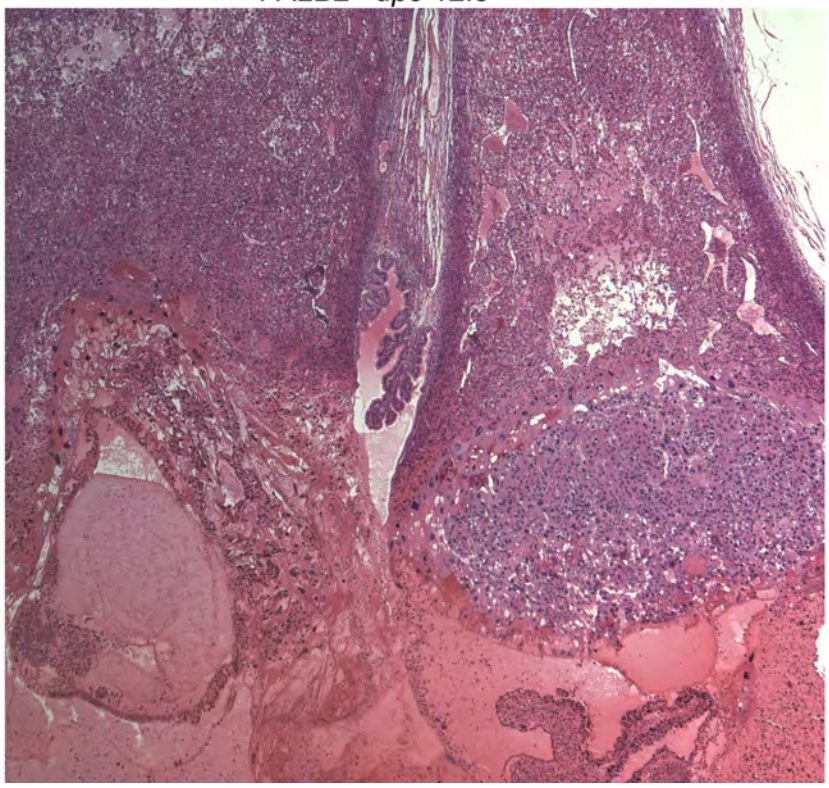

Figure S4

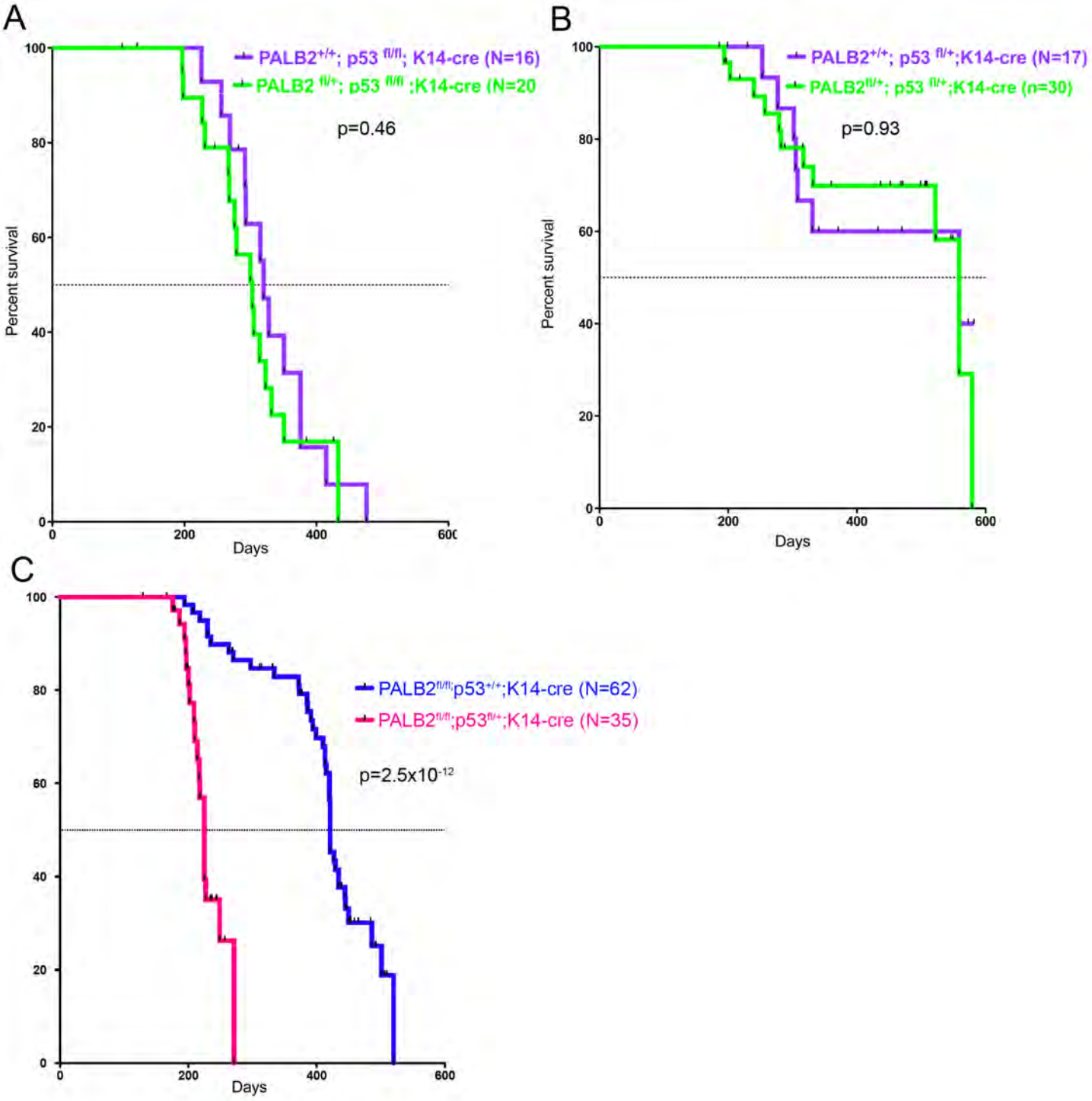
A
PALB2+/+; p53 fl/fl; K14-cre (N=16)
PALB2 fl/+; p53 fl/fl ;K14-cre (N=20
p=0.46
Percent survival
Days
B
PALB2+/+; p53 fl/+;K14-cre (N=17)
PALB2fl/+; p53 fl/+;K14-cre (n=30)
p=0.93
Percent survival
Days
C
PALB2fl/fl;p53+/+;K14-cre (N=62)
PALB2fl/fl;p53fl/+;K14-cre (N=35)
p=2.5x10-12
Days

Figure S5

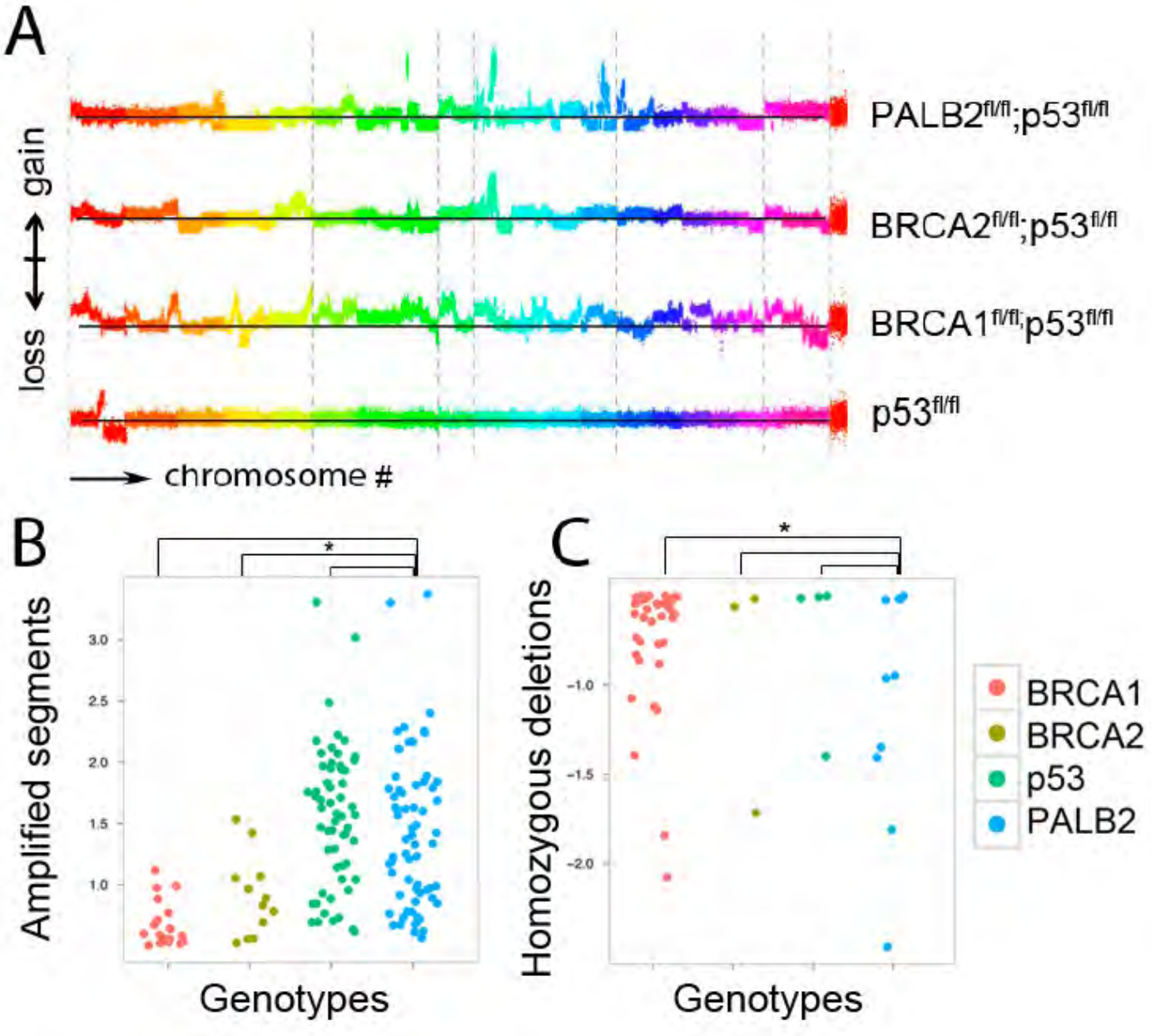
A
gain
loss
chromosome #
PALB2fl/fl;p53fl/fl
BRCA2fl/fl;p53fl/fl
BRCA1fl/fl;p53fl/fl
p53fl/fl
B
Amplified segments
3.0
2.5
2.0
1.5
1.0
*
Genotypes
C
Homozygous deletions
-1.0
-1.5
-2.0
*
Genotypes
BRCA1
BRCA2
p53
PALB2

Figure S6

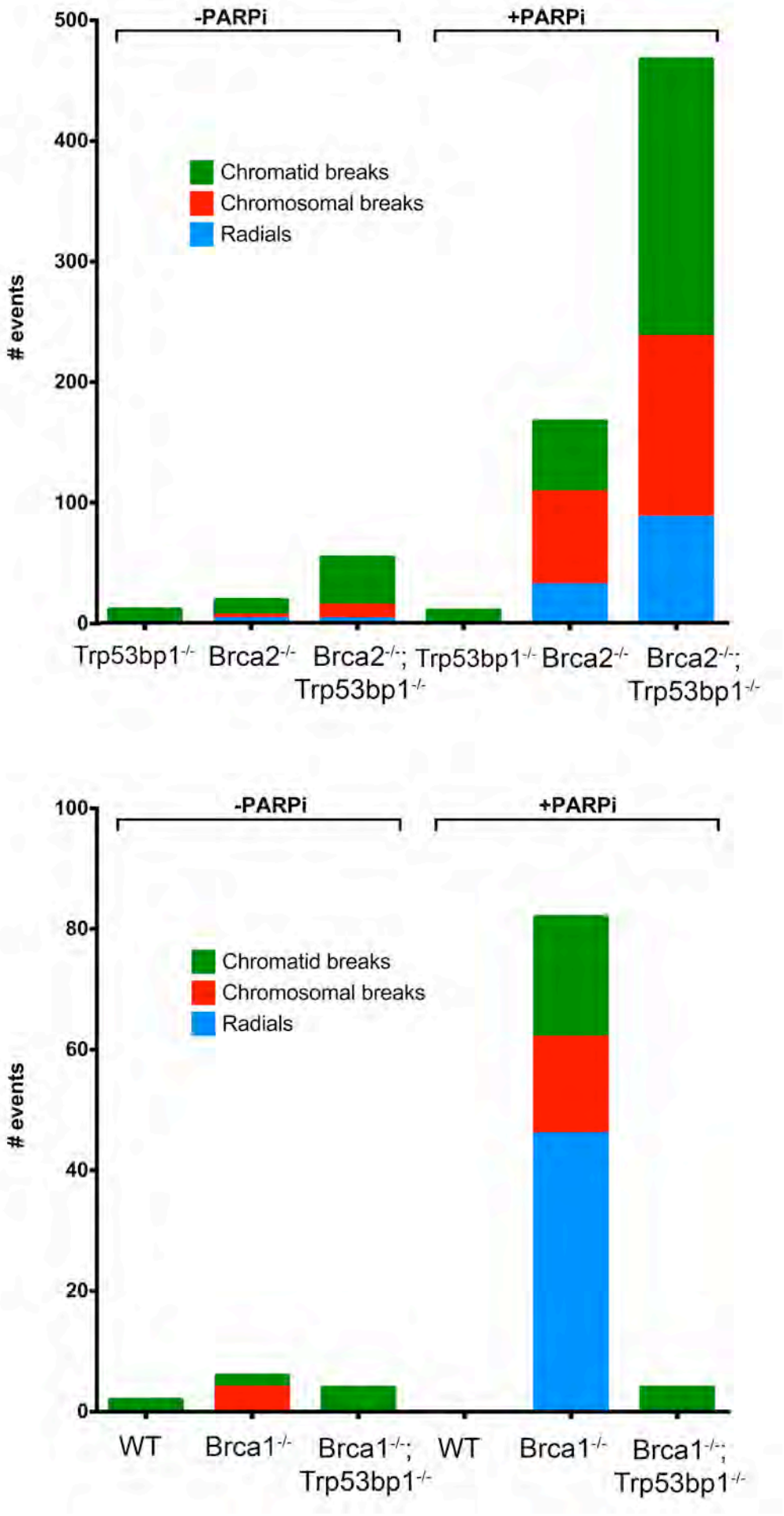
-PARPi
+PARPi
500
400
300
200
100
0
events
Chromatid breaks
Chromosomal breaks
Radials
Trp53bp1-/-
Brca2-/-
Brca2-/-; Trp53bp1-/-
Trp53bp1-/-
Brca2-/-
Brca2-/-; Trp53bp1-/-
100
80
60
40
20
0
events
Chromatid breaks
Chromosomal breaks
Radials
WT
Brca1-/-
Brca1-/-; Trp53bp1-/-
WT
Brca1-/-
Brca1-/-; Trp53bp1-/-